Lightning-Driven Electric and Magnetic Fields Measured in the Stratosphere: Implications for Sprites

Jeremy Norman Thomas

A dissertation submitted in partial fulfillment
of the requirements for the degree of

Doctor of Philosophy

University of Washington

2005

Program Authorized to Offer Degree: Earth and Space Sciences

INFORMATION TO USERS

The quality of this reproduction is dependent upon the quality of the copy submitted. Broken or indistinct print, colored or poor quality illustrations and photographs, print bleed-through, substandard margins, and improper alignment can adversely affect reproduction.

In the unlikely event that the author did not send a complete manuscript and there are missing pages, these will be noted. Also, if unauthorized copyright material had to be removed, a note will indicate the deletion.

ProQuest Information and Learning Company
300 North Zeeb Road
P.O. Box 1346
Ann Arbor, MI 48106-1346

University of Washington
Graduate School

This is to certify that I have examined this copy of a doctoral dissertation by

Jeremy Norman Thomas

and have found that it is complete and satisfactory in all respects,
and that any and all revisions required by the final
examining committee have been made.

Chair of Supervisory Committee:

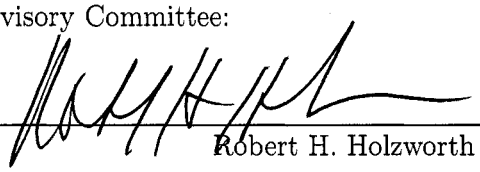

Robert H. Holzworth

Reading Committee:

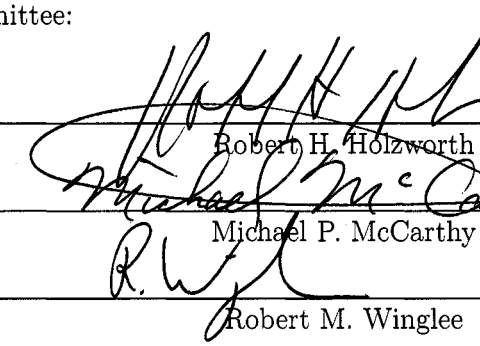

Robert H. Holzworth

Michael P. McCarthy

Robert M. Winglee

Date: August 10, 2005

In presenting this dissertation in partial fulfillment of the requirements for the doctoral degree at the University of Washington, I agree that the Library shall make its copies freely available for inspection. I further agree that extensive copying of this dissertation is allowable only for scholarly purposes, consistent with "fair use" as prescribed in the U.S. Copyright Law. Requests for copying or reproduction of this dissertation may be referred to Proquest Information and Learning, 300 North Zeeb Road, Ann Arbor, MI 48106-1346, to whom the author has granted "the right to reproduce and sell (a) copies of the manuscript in microform and/or (b) printed copies of the manuscript made from microform."

Signature Jeremy A. Thurman

Date August 10, 2005

University of Washington

Abstract

Lightning-Driven Electric and Magnetic Fields Measured in the Stratosphere: Implications for Sprites

Jeremy Norman Thomas

Chair of Supervisory Committee:
Professor Robert H. Holzworth
Earth and Space Sciences

A well accepted model for sprite production involves quasi-electrostatic fields (QSF) driven by large positive cloud-to-ground (+CG) strokes that can cause electrical breakdown in the middle atmosphere. A new high voltage, high impedance, double Langmuir probe instrument is designed specifically for measuring these large lightning-driven electric field changes at altitudes above 30 km. This High Voltage (HV) Electric Field Detector measured 200 nearby (< 75 km) lightning-driven electric field changes, up to 140 V/m in magnitude, during the Brazil Sprite Balloon Campaign 2002-03.

A numerical QSF model is developed and compared to the in situ measurements. It is found that the amplitudes and relaxation times of the electric fields driven by these nearby lightning events generally agree with the numerical QSF model, which suggests that the QSF approach is valid for modeling lightning-driven fields. Using the best fit parameters of this comparison, it is predicted that the electric fields at sprite altitudes (60-90 km) never surpass conventional breakdown in the mesosphere for each of these 200 nearby lightning events.

Lightning-driven ELF to VLF (25 Hz - 8 kHz) electric field changes were measured for each of the 2467 cloud-to-ground lightning (CGs) detected by the Brazilian Integrated Lightning Network (BIN) at distances of 75-600 km, and magnetic field changes (300 Hz - 8 kHz) above the background noise were measured for about 35% (858) of these CGs. ELF pulses that occur 4-12 ms after the retarded time of the lightning sferic, which have been previously attributed to sprites, were found for 1.4% of 934 CGs examined with a strong bias towards +CGs (4.9% or 9/184) compared to -CGs (0.5% or 4/750). These results disagree with results from the Sprites99 Balloon Campaign [Bering et al., 2004b], in which the lightning-driven electric and magnetic field changes were rare, while the CG delayed ELF pulses were frequent. The Brazil Campaign results thus suggest that mesospheric currents are likely the result of the QSF driven by large charge moment strokes, which are usually +CG strokes, initiating breakdown in the middle atmosphere.

TABLE OF CONTENTS

LIST OF FIGURES

LIST OF TABLES

ACKNOWLEDGMENTS

I thank everyone in the Space Physics Group of the Department of Earth and Space Sciences. I give special thanks to my advisor, Professor Robert Holzworth, whose expertise in making in situ measurements in the atmosphere made this dissertation possible, and for supporting me throughout my years working with him. I am grateful to Professor Michael McCarthy who taught me the art of building and testing sensors, and for carefully reading and critiquing my articles. I owe thanks to Professor Robert Winglee who showed me the fundamentals of numerical modeling which eventually led to the QSF model. I appreciate the help of Research Engineer John Chin who passed on to me some of his tremendous knowledge of analog circuit design, because of him the HV Electric Field Sensor was possible. I am grateful to Professor Timothy Chinowski whose telemetry system worked wonderfully and allowed for a great data set. I owe it to Professor Victor Pasko at Penn. State U. for helping with the development of the QSF model and for many fruitful discussions about how sprites might initiate. I am thankful to Mitsuteru Sato (RIKEN, Japan) and Tohoku U., Japan for estimating charge moments from their ELF magnetic field data. I owe it to Dave Rust and Don MacGorman (NOAA, National Severe Storms Laboratory), for allowing Natália Solórzano and I to test our electric field sensor as part of the TELEX campaign in Oklahoma. I give special thanks to graduate students Michael Kokorowski, Erin Lay, Carol Paty, and Ruth O'Connor who were always there to point out where I dropped the minus sign and to provide nice distractions from work. I am grateful to summer undergraduates Graylan Vincent and Nimisha Ghosh Roy whose help in the lab made the Brazil Balloon Campaign a reality. I thank research

associates Bill Peria and Erika Harnett whose help kept me on the right path. I am especially grateful to my father and mother who always encourage me to follow my passions in life and to never quit. And to my wife, Natália, who is always there for me, I could have not done this without you.

This work was supported by U. S. National Science Foundation under grants ATM-0091825 and ATM-0355190 to the University of Washington. Additional equipment support was provided through a Mindlin Foundation grant to the University of Washington Space Science Instrumentation Fund.

DEDICATION

To Natália, Carter, Connie, and Jonathan.

Chapter 1

INTRODUCTION

In this dissertation, lightning-driven electric and magnetic field measurements in the stratosphere, along with a numerical model, are used to study how discharges in the middle and upper atmosphere, known as sprites, are generated. Section 1.1 outlines the practical applications and fundamental geophysics that are addressed in this work. A brief introduction to thunderstorms and lightning, the tropospheric driving mechanisms for electric and magnetic fields in the middle and upper atmosphere, are presented in section 1.2. Sprites and other transient luminous events, including a brief outline of possible mechanisms for sprite production, are described in section 1.3. Section 1.4 is an overview of the electrical environment of the atmosphere. Previous balloon- and rocket-borne measurements of the electrical environment above thunderstorms are presented in section 1.5. A summary of the experimental campaign central to this dissertation, the Brazil Sprite Balloon Campaign 2002-03, is found in section 1.6. Section 1.7 outlines the structure of this dissertation.

1.1 Why Study How Thunderstorms Affect the Middle and Upper Atmosphere?

1.1.1 Practical Applications

Sprites, or other thunderstorm related transient luminous events (TLEs), might be a significant driving mechanism of the global electric circuit, or they may be viable producers of NOx in the middle atmosphere [Hiraki et al., 2002]. Also, the gap

between the inner and outer radiation belts of the Earth might be the result of lightning-driven electron precipitation [Voss et al., 1998; Clilverd et al., 2004]. These high altitude discharges also may adversely affect radio communication systems and aircrafts. Although discharges in the middle atmosphere have yet to be directly linked to air- or spacecraft failure, in 1987, the Atlas-Centaur 67 rocket triggered a lightning discharge that scrambled the on-board electronics causing the rocket to destruct. NASA now has criteria in place at Cape Canaveral that restricts launches when tropospheric lightning and/or high altitude electrical discharges are possible.

1.1.2 Fundamental Geophysics

The main focus of this work is to address the following fundamental questions about the electrical environment above thunderstorms using in situ measurements in the stratosphere:

1. Are the magnitudes and relaxation times of the nearby lightning-driven quasi-electrostatic fields (QSF) above thunderstorms sufficient for sprite production and growth?

2. Do the lightning-driven ELF/VLF (25 Hz-8 kHz) electromagnetic field perturbations measured in the stratosphere indicate that current is flowing in the mesosphere after CG strokes?

3. Do QSF and ELF/VLF models and other experiments agree with these measurements?

4. Do conductivity measurements suggest that thunderstorms affect the electrical relaxation times in the middle and upper atmosphere, thus affecting how TLEs initiate or grow?

1.2 *Thunderstorms and Lightning*

The focus of this work is to study how thunderstorms and lightning affect the middle and upper atmosphere including the stratosphere, mesosphere and lower ionosphere. This section will provide a brief introduction to the these tropospheric driving mechanisms for electric and magnetic fields in the middle and upper atmosphere.

1.2.1 Thunderstorms

Thunderstorms consist of a system of lightning-producing cumulonimbi, or thunderclouds, which can develop from small fair-weather clouds known as cumuli. When the relative humidity in warm, moist air parcels that rise and cool by adiabatic expansion surpasses saturation, condensation occurs on airborne particles thus forming the visible cloud. If the atmosphere is unstable, meaning that the lapse rate of atmospheric temperature is greater than the moist-adiabatic lapse rate (0.6^0C per 100 m), these parcels of warm, moist air remain warmer than the air around them and thus stay buoyant, forming cumuli and eventually thunderclouds. For parcels that rise above the -40^0 C isotherm, all water particles in that parcel will be frozen. But for parcels that rise to above the 0^0 C and below the -40^0 C isotherms, both supercooled water and ice particles can co-exist allowing for electrification to occur.

Thunderstorms form in lowest layer of the atmosphere, the troposphere, where the temperature decreases with height until reaching the tropopause. The tropopause varies with latitude and season with typical altitudes of 15-18 km for low latitudes and 8-10 km for high latitudes. The atmospheric layer above the troposphere, the stratosphere (the layer where measurements were made during the Brazil Balloon Campaign), is characterized by a temperature increase with height (due to absorption of ozone by UV radiation). Thus, parcels of warm, moist air lose their buoyancy and cease rising. Although for particularly strong thunderstorms with intense updrafts, cloud growth can overshoot into the lower stratosphere (up to 20 km) due to strong

upward momentum.

Thunderstorms occur throughout the year in the tropics and primarily during the spring and summer in midlatitude regions. Thunderstorms do also occur in the polar regions during the summer. Local, small convective storms form in the spring and summer in midlatitudes due to the abundance of warm, moist air in the atmosphere which drives the convection process. The instability that allows the convection process to continue can be caused by differential heating (e.g. between the sea and the land or mountains and valleys), orgraphic effects (e.g. mountains directing horizontal wind upwards to increase vertical convection), or short wave upper level disturbances (e.g. a small scale pressure trough). Large-scale storms can form due to frontal activity, such as cold or warm fronts, that produce widespread instability of the atmosphere. These larger storms occur throughout the year in mid-latitudes, but the majority of lightning producing storms occur in the spring and summer. A cluster of medium to large scale thunderstorms that form due to this widespread instability is known as a mesoscale convective system (MCS), and a singular large scale storm is a mesoscale convective complex (MCC). These MCS and MCC storms are huge charge reservoirs that are capable of producing very intense lightning discharges [Williams, 1998], with most sprite observations having occurred during these types of storms [Lyons, 1996]. For a more complete review of the meteorology of thunderstorms, see Williams [1995] and Rakov and Uman [2003].

The most idealized charge distribution of thunderclouds is an electric dipole with an upper positive region and lower negative region. A slightly more detailed model includes a positive region below the negative region or a tripole distribution [Rakov and Uman, 2003]. In situ cloud measurements have found that actual charge distribution can be much more complex, with numerous layers of charge [Stolzenburg et al., 1998].

How these cloud layers form is poorly understood compared to the meteorology of thunderstorms due to the complex processes involved at the particle level. The most

well accepted model for cloud electrification is the graupel-ice charging mechanism (for a review of cloud electrification including other charging mechanisms see Saunders [1995]). In brief, in the graupel-ice charging mechanism the heavier graupel particles fall colliding with the lighter ice crystals and supercooled water particles. Below a critical temperature (T_R, or reversal temperature), the graupel particles acquire negative charge with the ice crystal acquiring positive charge. And above T_R the graupel particles acquire positive charge while the ice crystals acquire negative charge. This reversal temperature has been measured experimentally [Jayaratne et al., 1983] to be between about -10 and -20^0 C [Rakov and Uman, 2003]. However, the polarity and amount of charge separated in this process also depends on the supercooled water content and droplet size, ice crystal size, relative velocity of the collisions, and contaminants in the water [Rakov and Uman, 2003].

The charging mechanism outlined above generates a large electrostatic field inside the thundercloud. Balloon-borne field mill soundings of the thunderclouds have measured electric fields up to a few hundred kV/m, but never surpassing the conventional breakdown threshold for air [Stolzenburg et al., 1998; Marshall et al., 1995]. This suggests that either microscale fields or relativistic breakdown [Marshall et al., 1995] are responsible for lightning initiation. The initiation of discharges will be discussed further in the context of sprites in section 1.2.

1.2.2 Lightning

According to the most recent data from the LIS and OTD satellites, about 44 flashes occur globally each second [Christian et al., 2003] with a 3:1 ratio of cloud flashes to ground flashes [see Rakov and Uman, 2003, Chpt. 2.7]. Globally, about 90% of cloud-to-ground strokes have negative polarity, or transfer negative charge from the cloud to the ground. However, during the waning stages of large storms and during some winter storms [Takahashi et al., 2003] a high percentage of positive cloud-to-ground (+CG) strokes can occur.

Typical negative cloud-to-ground (-CG) flashes initiate with preliminary breakdown due to the large electric fields inside the cloud. From this preliminary breakdown, a negatively charged plasma channel, or stepped leader, discretely moves downward at about 2×10^5 m/s, to form a conducting path between the cloud and the ground [Rakov and Uman, 2003, Chpt. 4.2]. As this descending leader nears the ground, an upward propagating leader from the ground is initiated by the large electric field produced by the downward leader. The downward and upward propagating leaders typically attach at a few 10s of meters above the ground and initiate a first return stroke. This first return stroke neutralizes the negative charge on the leader channel in about 70 μs with a peak current of about 20-40 kA, on average. After this first return stroke the flash may end, but usually a subsequent downward propagating leader will develop, known as a dart leader. This dart leader extends down the first stroke channel at about 10^7 m/s and attaches to an upward leader near the ground which allows for a second return stroke. This process can continue and produce numerous subsequent strokes. See Chpt. 3 for -CG lightning-driven electric and magnetic fields measured in the stratosphere.

Although +CG flashes have about the same peak current as -CG flashes on average (20-40 kA), many of the other characteristics of +CG flashes are unique [Rakov and Uman, 2003, Chpt. 5]. Positive CG flashes are usually composed of one return stroke followed by long continuing currents (10s to 100s of ms) and substantial in-cloud lightning activity. Moreover, +CG discharges are often composed of long horizontal channels, 10s of km in size, which allow for the possibility of large reservoirs of charge to be tapped. Finally, the positive leader for an initial +CG stroke can propagate either in steps, like initial -CG strokes, or continuously, like a -CG dart leader. Positive CG discharges are of special interest in the context of this study because of the correlation between +CG strokes and sprites, which is further discussed in section 1.2, and Chpts. 3 and 5.

Cloud discharges, the most common type of lightning on earth, initiate near the

lower and upper boundaries of the negative charge region where the electric fields are greatest [Rakov and Uman, 2003, Chpt. 9]. This initiation is followed by an active stage characterized by a negative leader which bridges the negative and positive charge regions in the cloud in 10s to 100s of ms. This negative leader during this active stage is much like a stepped leader in a CG flash, propagating at about 10^5 m/s with currents of 10s to 100s of A and related to the largest changes in the electric field record. The disconnection between the negative and positive regions marks the end of this active stage. The final stage which follows is characterized by small electric field changes and low currents; this stage likely allows for negative charge to repopulate the discharge initiation point from remote locations in the cloud. See Chpt. 3 for cloud discharge-driven electric and magnetic fields measured in the stratosphere.

1.2.3 Large Scale Thunderstorm Electric and Magnetic Fields

Electrostatic, induced and radiated fields are generated by lightning discharges in thunderclouds. The electrostatic field at the earth from a single charge located above the earth (assumed to be a perfect conductor) and its image charge below the earth can be found from Coulomb's law to be

$$E = \frac{2QZ}{4\pi\epsilon_0(Z^2 + R^2)^{3/2}} \tag{1.1}$$

where the charge Q is at a height Z at a distance R along the earth assuming that $R >> Z$. A CG stroke removes charges from (or inserts opposite charges into) the thundercloud which results in a charge moment of

$$M_q = \sum_i Q_i Z_i \tag{1.2}$$

where the total charge moment is the sum over all the charges removed (or opposite charges inserted) times their altitudes. The electric and magnetic fields at the earth

due the CG stroke can be shown to be (see Uman [1984, Chpt. 3])

$$E = \frac{2[M_q]}{4\pi\epsilon_0 R^3} + \frac{2}{4\pi\epsilon_0 c R^2}[\frac{dM_q}{dt}] + \frac{2}{4\pi\epsilon_0 c^2 R}[\frac{d^2 M_q}{dt^2}] \tag{1.3}$$

$$B = \frac{2\mu_0}{4\pi R^2}[\frac{dM_q}{dt}] + \frac{2\mu_0}{4\pi c R}[\frac{d^2 M_q}{dt^2}] \tag{1.4}$$

where c is the speed of light and quantities in brackets are evaluated at their retarded times $(t - R/c)$. For these equations to be valid, $R >> Z_i$, the current resulting for the change in M_q must be constant along the path of the current, and each R_i must be constant. Note that Uman [1984, Chpt. 3] defines M_q as $2 \times M_q$ that is defined above. The first term in (1.3) is the electrostatic field that results from the redistribution of thundercloud charge after a CG stroke and falls off as $1/R^3$. In Chpt. 3.2 electrostatic stratospheric measurements of nearby lightning events are presented, these electrostatic fields are likely responsible for sprites (see section 1.2 and Chpt. 5) and thus a main focus of this study. The second and third terms of (1.3) and the first and second terms of (1.4) are the induced and radiated fields that are due to the CG stroke current and the time derivative of this current, respectively. These induced and radiated fields fall off as $1/R^2$ and $1/R$ and are the dominant CG fields beyond about $R = 75$ km. In Chpt. 3.3 examples of induced and radiated fields measured in the stratosphere due to CG strokes are presented, and possible induced and radiated fields due to mesospheric currents are presented in Chpt. 3.4. Note that (1.3) and (1.4) do not include the non-zero, exponentially increasing with altitude, atmospheric conductivity which affects how these fields propagate. In Chpt. 5, the electrostatic field ((1.3), term 1) due to a +CG stroke is modeled including the atmospheric conductivity and the self-consistent effects of the CG stroke on the conductivity.

1.3 *Sprites and Other Transient Luminous Events*

Sprites are transient luminous events (TLEs), or optical discharges that last up to 10s of ms, that occur between 40 and 90 km in altitude above thunderstorms illuminating the stratosphere and mesosphere [Sentman et al., 1995; Boeck et al., 1991; Lyons, 1994]. These high altitude discharges were first imaged by accident by Franz et al. [1990], and have since been correlated with positive cloud-to-ground lightning (+CG) strokes [Lyons, 1996] with large charge moments [Cummer and Lyons, 2004, 2005] usually occurring during MCS or MCC storms (see section 1.2.1). Figure 1.1 shows sprites imaged from an aircraft during the Sprites94 Campaign over the U. S. High Plains [Sentman et al., 1995]. Models suggest that these large +CG strokes generate a large quasi-static electric field (an electrostatic field that decays in time due to the non-zero atmospheric conductivity, see Chpt. 5) above the thundercloud, which leads to breakdown seen as sprites [Roussel-Dupre and Gurevich, 1996; Pasko et al., 1997a; Lehtinen et al., 1997; Rowland, 1998] (see section 1.2.1). Sprites are initiated in the mesosphere at altitudes between about 65-80 km [Stanley et al., 1999; Wescott et al., 2001a]. After this initial breakdown, sprite streamers can propagate down to about 40 km and up to about 80 km [Stanley et al., 1999; Pasko et al., 1998a], and a diffuse glow, known as the sprite halo, forms at about 80-90 km [Wescott et al., 2001a; Pasko et al., 1998a]. Sprites have been observed to occur from a few ms to more than 30 ms after the parent +CG lightning discharge [Boccippio et al., 1995; São Sabbas et al., 2003]. Moreover, sprites can be displaced horizontally by more than 50 km from the location of the parent +CG stroke [Wescott et al., 2001a; São Sabbas et al., 2003]. Sprites correlated with -CG strokes have been reported as well [Barrington-Leigh et al., 1999], but these are extremely rare compared to the numerous reports of +CG stroke correlated sprites.

Blue jets are optical discharges that propagate from the top of a thundercloud upward into the stratosphere and mesosphere [Wescott et al., 1995, 2001b] and some-

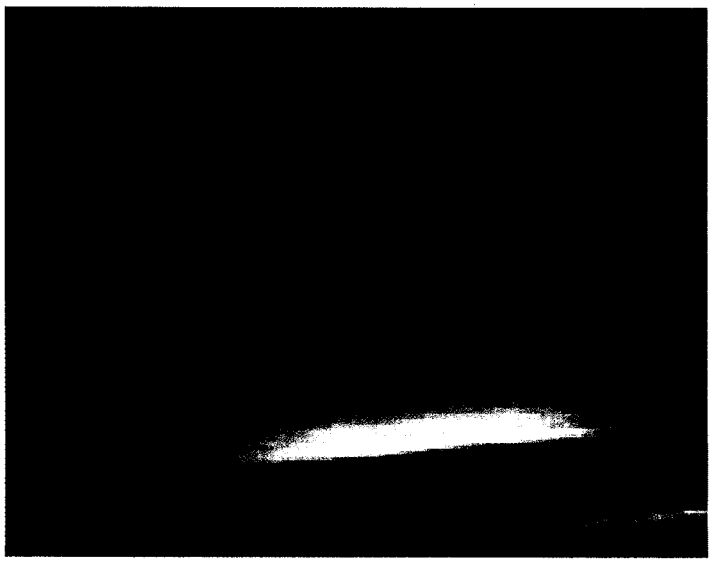

Figure 1.1: Sprites imaged over the U. S. High Plains from an aircraft during the Sprites94 campaign, July, 2004 (reproduced from Sentman et al. [1995]).

times connecting with the ionosphere at about 90 km in altitude [Pasko et al., 2002; Su et al., 2003] as shown in Figure 1.2. Unlike sprites which are correlated with +CG strokes, jets are not correlated with individual strokes. Thus, models suggest that jets are due to large electrostatic fields, resulting from the cloud charge distribution, surpassing breakdown inside and above thunderclouds [Pasko et al., 2002].

Elves are an expanding disks of optical emissions that occur in the lower ionosphere (90-100km) after large peak current (> 60kA) CGs of both negative and positive polarity [Fuknunishi et al., 1996; Inan et al., 1997; Barrington-Leigh and Inan, 1999; Barrington-Leigh et al., 2001], as shown in Figure 1.3. Unlike sprites and jets which are likely caused by quasi-electrostatic fields, models suggest that elves are the result of the lightning return stroke generated electromagnetic pulses (EMP) [Fernsler and Rowland, 1996; Rowland, 1998]. Figure 1.4 is a cartoon portraying the "big picture" of TLEs including sprites, jets, and elves [Lyons et al., 2003; Pasko, 2003].

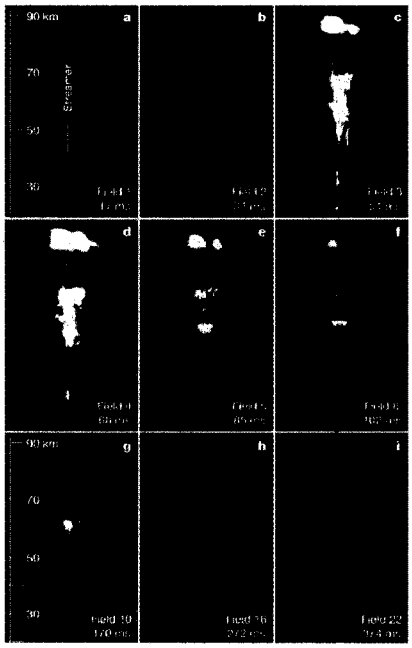

Figure 1.2: A gigantic jet reaching from the top of the thundercloud to the ionosphere over the South China Sea imaged from Taiwan (reproduced from Su et al. [2003]).

Figure 1.3: An elve imaged over Europe in Nov. 1999 by M. J. Taylor and L. C. Gardner of Utah St. U. (reproduced from http://leonid.arc.nasa.gov/leonidnews.html).

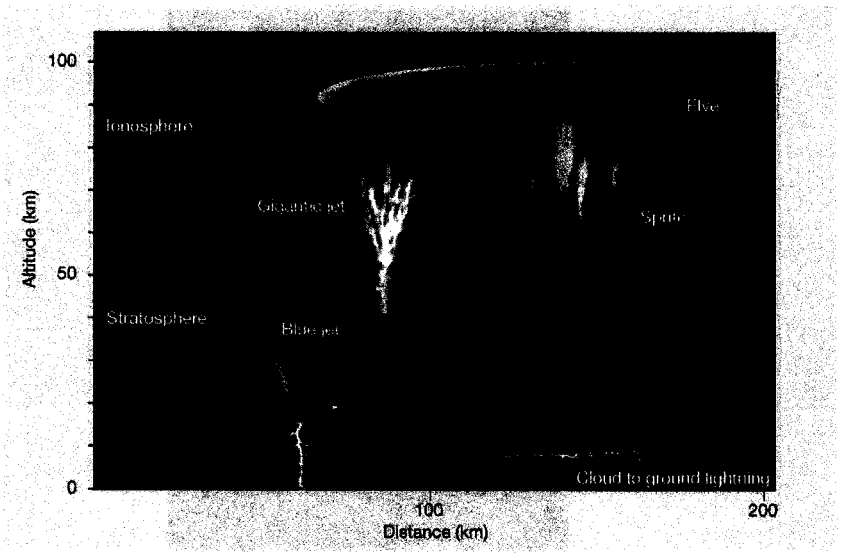

Figure 1.4: A cartoon of the "big picture" of TLEs showing sprites, jets, and elves (reproduced from Lyons et al. [2003]; Pasko [2003]).

1.3.1 Sprite Models

C. T. R. Wilson [1925] first hypothesized that a large quasi-electrostatic field above thunderclouds would generate discharges between cloud tops and the ionosphere. Most sprite models are built upon this concept of a large quasi-electrostatic field causing electrical breakdown in the mesosphere and stratosphere. The removal of large amounts of positive charge during a +CG stroke with a long continuing current (as discussed in section 1.1.2) results in a large quasi-static electric field to form above the cloud pointing downward. The magnitude of this electric field is determined by the charge moment M_q (product of the total charge removed and the height from which it is removed, see equation (1.2)) of the lightning discharge, the continuing current discharge time τ_d, the atmospheric conductivity σ, and the cloud charge distribution ρ_c. If the field above the cloud surpasses the conventional breakdown threshold E_k, the sprite can be initiated. By surpassing the positive streamer threshold E_{cr}^{+}, the

sprite discharge can propagate downwards in a region where the field is below the conventional threshold. This is known as the quasi-electrostatic field (QSF) model for sprite production. In Chpt. 5 a numerical QSF model is developed and compared to in situ measurements from the Brazil Balloon Campaign. Using the best fit parameters of this comparison, the electric field change everywhere in the stratosphere and mesosphere can be predicted and compared to various electrical breakdown thresholds needed for the initiation and/or growth of sprites.

Another model incorporates this QSF approach with the presence of relativistic electrons ($\sim$ 1 MeV) that result from cosmic ray secondaries [Roussel-Dupre and Gurevich, 1996; Lehtinen et al., 1997]. The quasi-static field accelerates these relativistic electrons upward. If the field is sufficiently large, then electrons gain more energy from the electric field then is lost by colliding with neutrals. These electron are able to continue to accelerate in the electric field and produce more free electrons through collisions. Hence, the free electron population grows exponentially, known as electron runaway. The stopping force for electrons with neutrals has the form shown in Figure 1.5 which has a minimum around 1.2 MeV. Thus, electrons with this energy can cause runaway with a minimum electric field value of 2×10^5 V/m at STP, known as the runaway threshold E_t.

1.4 The Global Atmospheric Electric Circuit

A fair weather vertical electric field of about 100 V/m, pointing downwards, exists near the Earth's surface due to a negatively charged surface and positively charged atmosphere. The highly conductive Earth's surface and ionosphere (alt.$\sim$ 90 km) form a spherically concentric capacitor that leaks due to the non-zero conductivity of the atmosphere in between them. Since these fair weather charges remain quasi-stable over time, there must exist a driving mechanism which supports this charge distribution and the resulting fair weather electric field. Without a driving mechanism, the

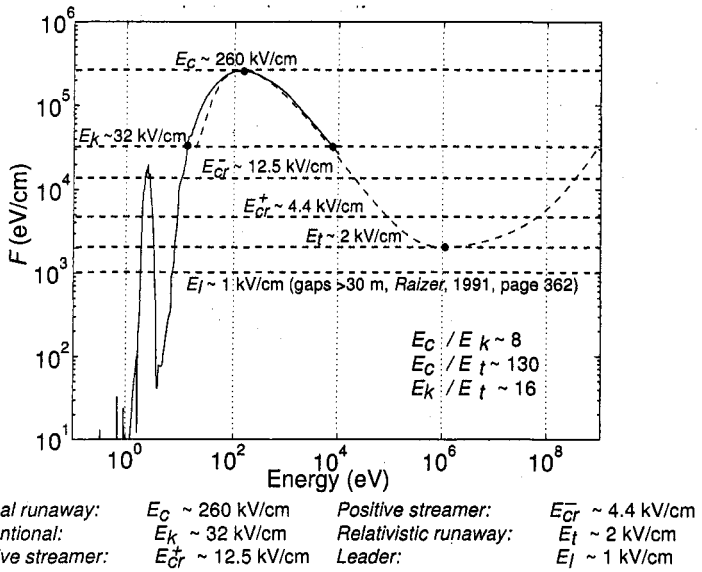

Figure 1.5: The stopping force for electrons with neutrals vs. electron energy (reproduced from Pasko [2004]). Note the minimum at about 1.2 MeV which allows for electrons in a field greater than 2×10^5 V/m to initiate runaway (an exponential growth of the electron population).

Earth-ionosphere capacitor would discharge in less than 1 hour. Wilson [1920] first suggested that thunderstorms support this global electric circuit by driving positive charge upwards to the ionosphere and negative charge downwards to the Earth's surface. The simple dipole model of a thunderstorm, with a positive over negative charge structure, would drive charge in the direction to keep the Earth-ionosphere capacitor charged as illustrated in Figure 1.6 . However, it is unclear whether thunderstorms provide enough driving to maintain this global circuit.

Some properties of the global electric circuit are the following [Roble and Tzur, 1986]: fair weather global current of $750 - 2000$ A, fair weather current density of $1.0 - 2.5 \times 10^{-12}$ A/m^2, currents above thunderstorms of $0.1 - 6.0$ A, 1500-2000 active thunderstorms at one time, ionospheric potential of $150 - 600$ kV, total resistance of

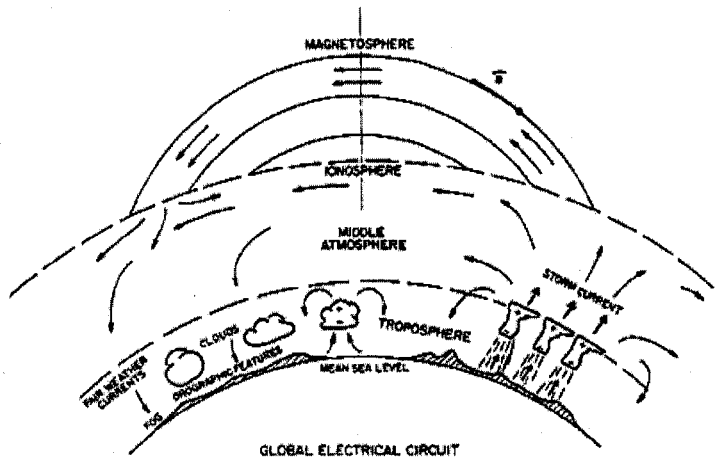

Figure 1.6: An illustration of the Wilson thunderstorm hypothesis of global electric circuit (reproduced from Roble and Tzur [1986]).

200Ω, fair weather electric field just above the Earth's surface of $70-400$ V/m downward, total charge on the Earth of about 500,000 C, and conductivity that increases quasi-exponentially with altitude from about $10^{-14}(\Omega\text{m})^{-1}$ just above the surface to $> 10^{-9}(\Omega\text{m})^{-1}$ near the ionospheric D region lower boundary (60 km alt. during the day, 90 km alt. during the night). See Chpt. 4 for conductivity measurements in the stratosphere during the Brazil Campaign and Chpt. 5 for how the conductivity is employed in the QSF model.

A back of the envelope calculation would suggest that if all 1500-2000 thunderstorms generated about 1 A of current this would be enough to drive the global current of 750-2000 A. But it is unclear how much current each storm actually drives since there have only been an handful of in situ measurements (see section 1.5). Also the role discharges above thunderstorms, such as sprites and jets (see section 1.3), play in the global circuit is unknown.

1.5 Historical Review of Electric Field Measurements Above Thunderstorms

The first electric field measurements above thunderstorms were obtained by Gish and Wait [1950] in 1948 using an aircraft flying at 12 km above 21 thunderstorms in the midwest of the United States. During the 1950s, Stergis et al. [1957] launched 25 balloons to 21-27 km over active thunderstorms in central Florida. These early experiments measured dc electric fields that pointed upwards over thunderstorms and varied with lightning activity. In addition to measuring electric fields, these experiments measured the atmospheric conductivity, which allowed for the calculation of the conduction current ($J = \sigma E$) above storms. Gish and Wait [1950] and Stergis et al. [1957] measured $J \approx 0.5$ A and $J \approx 1.3$ A above thunderstorms, which was the first experimental support for the Wilson [1920] hypothesis of thunderstorms as the drivers for the global electric circuit.

Subsequent balloon [Benbrook et al., 1974; Bering et al., 1980; Holzworth et al., 1985] and aircraft [Blakeslee et al., 1989] based measurements of electric fields and conductivity were made during the 1970s and 1980s. These balloon-borne experiments measured fields up to a few 10s of V/m at altitudes of about 25-37 km [Benbrook et al., 1974; Bering et al., 1980; Holzworth et al., 1985]. These aircraft experiments measured fields up to 5 kV/m at 20 km in altitude [Blakeslee et al., 1989]. Rocket-borne electric field and conductivity measurements have also been conducted above thunderstorms since the early 1980s [Hale et al., 1981; Maynard et al., 1981; Kelley et al., 1985] with lightning-driven field changes of 10s of mV/m measured in the mesosphere and ionosphere.

These previous experiments were not capable of measuring large electric fields (100s of V/m) at altitudes above 30 km, nor did they have adequate time resolution, to address how sprites might be generated. The first campaign to measure electric fields aloft near sprite-producing storms was conducted over the U. S. High Plains in 1999.

This Sprites99 Campaign [Bering et al., 2002, 2004a,b; Bhusal et al., 2004] included stratospheric balloon payloads that were capable of measuring electric fields up to 100 V/m along with magnetic fields and x-rays. A balloon-borne platform was used, rather than a rocket-borne platform, to maximize the probability of measuring the electric and magnetic fields correlated with sprites and sprite-parent lightning, since a rocket is only capable of making measurements for a few minutes. Unfortunately, the balloons during this campaign flew more than 300 km horizontal distance from thunderstorms activity. Thus, the near field quasi-static electric field change above the thundercloud was not measured, although electric field changes up to a few hundred mV/m were measured correlated with sprites [Bering et al., 2002]. See Chpts. 3 and 6 for further discussion of the Sprites99 Campaign results in relation to the Brazil Campaign results.

1.6 Overview of Sprite Balloon Campaign in Southeastern Brazil

The data included in this thesis were acquired during the Sprite Balloon Campaign 2002-2003 in southeastern Brazil. The objective of this campaign was to obtain in situ measurements, in the stratosphere, of the electromagnetic signature above sprite producing thunderstorms. Southeastern Brazil was chosen as the location for this campaign due to the frequent thunderstorm activity, the limited restrictions concerning stratospheric ballooning, and the collaboration with the Brazilian National Institute for Space Research (INPE) which funded the costs of the launching team. The campaign included two balloon flights (December 6-7, 2002 and March 6-7, 2003) each launched from Cachoeira Paulista, Brazil ($22^0 44'$ S, $44^0 56'$ W). During the two flights, the electric and magnetic field changes driven by thousands of lightning events were measured by the payloads, including some of the largest vector electric fields ever measured over intense thunderstorms above 30 km in the stratosphere (see Chpt. 3). Unfortunately, sprites could not be observed during these flights because the optical

imager mounted on an airplane was hindered by heavy cloud coverage (Flight 1), or the observation airplane was unable to take off due to severe local weather (Flight 2). Although, during this campaign, sprites were imaged for the first time from Brazil [Pinto et al., 2004], as shown in Figure 1.7, but not simultaneous to the balloon flights.

It is found that the amplitudes and relaxation times of the electric fields measured in the stratosphere during the Brazil Campaign driven by 200 nearby (< 75 km) lightning events (see Chpt. 3) generally agree with a numerical QSF model developed in this dissertation (see Chpt. 5), which suggests that the QSF approach is valid for modeling lightning-driven fields. Using the best fit parameters of this comparison, the electric field change everywhere in the stratosphere and mesosphere is predicted and compared to various electrical breakdown thresholds needed for the initiation and/or growth of sprites (see Chpt. 5). It is predicted that the electric fields at sprite altitudes (60-90 km) never surpass conventional breakdown in the mesosphere for each of these 200 nearby lightning events (see Chpt. 6). Moreover, lightning-driven ELF to VLF (25 Hz - 8 kHz) electric field changes were measured for each of the 2467 cloud-to-ground lightning (CGs) detected by the Brazilian Integrated Lightning Network (BIN) at distances of 75-600 km, and magnetic field changes (300 Hz - 8 kHz) above the background noise were measured for about 35% (858) of these CGs (see Chpt. 3). For 1.4% of 934 events studied, ELF pulses that occur 4-12 ms after the retarded time of the lightning sferic were detected, which may be indicative of mesospheric currents.

1.7 Dissertation Outline

Chpt. 2 is a detailed description of the instrumentation used to measure the electrical environment above thunderstorms during the Brazil Campaign, along with the complementary ground-based measurements. The lightning-driven electric and magnetic fields measured in the stratosphere are presented in Chpt. 3, and the atmospheric

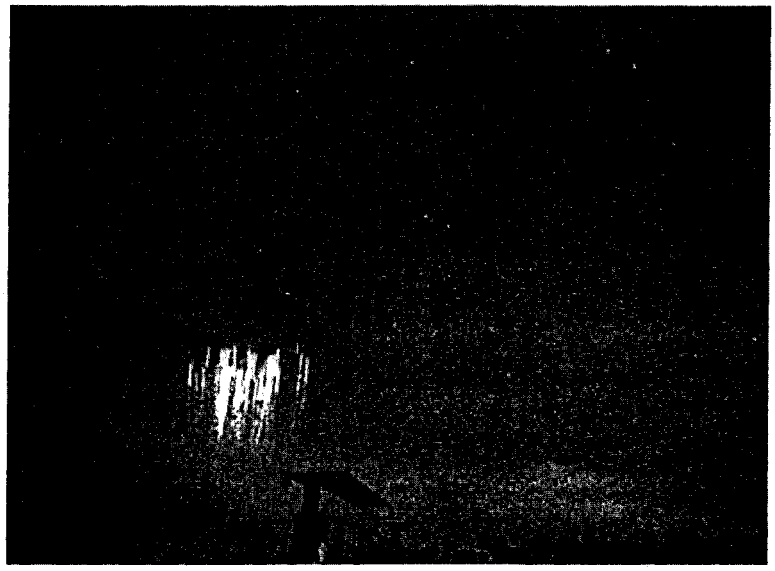

Figure 1.7: The first sprite imaged from the ground in Brazil on Nov. 25, 2002 from Cachoeira Paulista ($22^0 44'$ S, $44^0 56'$ W) (courtesy of M. J. Taylor and D. Pautet, Utah St. U.).

conductivity measured during Flight 1 is presented in Chpt. 4. In Chpt. 5, a QSF model is developed and compared to the in situ measurements. Chpt. 5 also includes predictions of the electric field at sprite altitudes using the best fit parameters to this comparison. The implications these electric and magnetic field measurements have on sprite formation are discussed in Chpt. 6. Chpt. 7 introduces ideas for future research, including another balloon campaign in Brazil.

Chapter 2

INSTRUMENTATION FOR THE BRAZIL SPRITE BALLOON CAMPAIGN

2.1 Overview of Instruments

The balloon-borne instrumentation package for the Sprite Campaign included sensors to measure electric fields, magnetic fields, x-rays, and optical power. The Low-Voltage (LV) and High-Voltage (HV) electric field instruments measured vector fields from dc to 10 kHz with a range of a few mV/m to 195 V/m. The LV vertical sensor was also used to measure the ambient conductivity of the atmosphere. Vector search coils measured ac magnetic fields from 300 Hz to 10 kHz. The dc to 100 Hz aspect magnetometer provided the orientation of the electric and magnetic fields measured relative to the geomagnetic field. Uplooking and downlooking NaI scintillators with attached photomultiplier tubes were capable of detecting x-rays within the 20 keV to 650 keV energy range. Two optical power sensors measured uplooking and downlooking light from lightning and/or possible TLEs. Figure 2.1 is a photo of the sprite balloon payload without the ground planes in place around the gondola. The large spheres and smaller cylinders are the LV and HV electric field probes, respectively. Just below the upper sphere are the vector magnetic field search coils. The x-ray sensors are housed within the central gondola along with the payload electronics responsible for controlling the sensors and telemetry. The transmitting antenna hung below the lower sphere during the flights, but is attached to the lower boom in Figure 2.1.

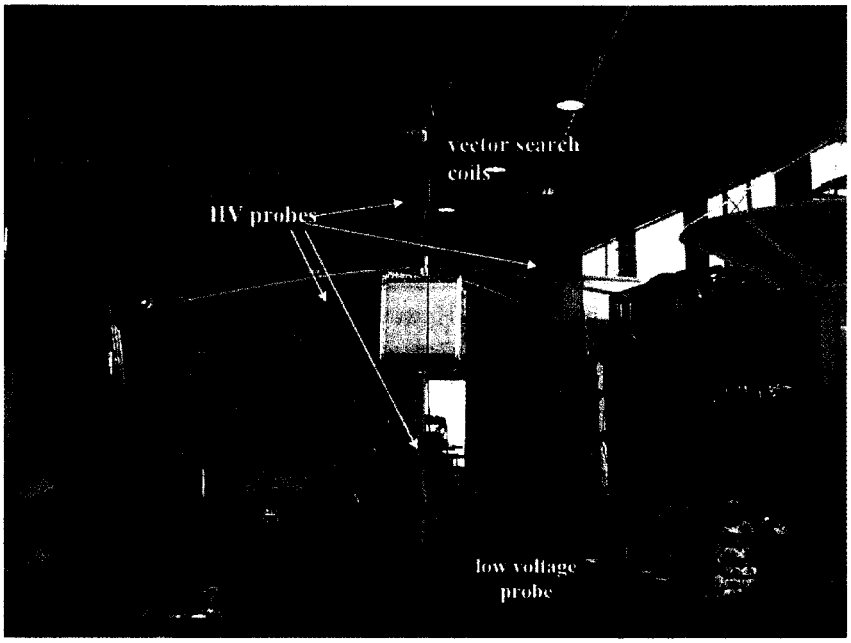

Figure 2.1: A photo of the sprite balloon payload.

2.2 The High-Voltage and Low-Voltage Electric Field Instruments

2.2.1 Basics of the Double Langmuir Probe Technique

The High-Voltage (HV) and Low-Voltage (LV) electric field instruments use the double Langmuir probe technique, first used (at much lower voltages) for atmospheric studies by Kellogg and Weed [1968] and Mozer and Serlin [1969], to measure electric fields in the stratosphere. This technique has been used by various researchers to study electric fields associated with auroral activity, thunderstorms, and fair weather [e.g. Benbrook et al. [1974]; Holzworth and Mozer [1979]; Bering et al. [1980]; Pinto et al. [1988]; Hu [1994]; Holzworth and Bering [1998]; Saba et al. [2000]]. Although, all of these double Langmuir probes, limited by the operational voltage of the preamplifiers used, measured electric fields less than about 10 V/m.

Field mill technology, rather than the double Langmuir probe technique, has been used to measure atmospheric electric fields below about 20 km in altitude. Field mill measurements of up to 5 kV/m have been made over thunderstorms from U-2 airplanes at 15-20 km altitude [Blakeslee et al., 1989]. Balloon-borne field mills have also been flown through thunderclouds measuring fields up to 200 kV/m below 10km in altitude [Marshall et al., 1995]. However, since the local relaxation time is only a few seconds at altitudes above 25-30 km, the field mill method is not an effective way to measure electric fields in this region of the stratosphere. This is because field mills measure the current that flows between two conductors connected with low impedance electronics as the conductors are rotated by a motor in and out of the electric field (see MacGorman and Rust [1998, Chpt. 6] for a discussion of field mills). The fields mills are calibrated such that a given electric field value drives a given current. Thus the rotation period of the field mill (which typically rotates at few Hz) must be much less than the ambient atmospheric relaxation time (see Figure 5.2), or the current will flow from the conductors into the atmosphere instead of through the low impedance electronics to the other conductor. This new HV detector, utilizing new high voltage, high input impedance operational amplifiers, is capable of measuring potential differences up to 240 V (or electric fields over 1 kV/m for 20 cm probe separation), at altitudes above the field mill regime, to study lightning discharges and/or sprites. Note that Bering et al. [2002] did report using a balloon-borne detector above 30 km in altitude with a full scale range of $\pm$100 V/m, but no results have been published thus far.

The HV and LV electric field instruments employ this double Langmuir probe technique to allow for the measurement of large scale electric fields in the atmosphere with field frequencies limited by the slew rate of the operational amplifiers used. This technique consists of two conductors (spheres, plates, or cylinders) each with a sufficiently large surface area to collect enough charge to drive the electronics. These conductors are separated by a distance d which enables the probes to be adequately

far from the central payload (> 1 m) to reduce field anomalies caused by the payload structure. By measuring the potential difference between the two conductors ($V_{21} \equiv V_2 - V_1$) and dividing by the distance between the probes d, the electric field component ($E_{21} = V_{21}/d$) in the direction from probe 2 to probe 1 is determined. By orienting pairs of probes in three orthogonal directions, the vector electric field $\vec{E}$ is found.

2.2.2 Hardware for the HV and LV Detectors

The HV probes, or charge collectors, developed for the Sprite Campaign 2002-2003 are 20 cm long by 4 cm diameter cylindrical conductors placed on four booms to give voltage difference measurements of up to ±240 V along two independent directions, one vertical and one horizontal. Cylindrical conductors are used since they are cheaper and easier to fabricate than spheres. However, this shape does result in a different antenna factor for the HV cylindrical probes relative to the LV spherical probes as as discussed in section 2.2.5. The cylinders are placed on fiberglass booms extending vertically and horizontally from the balloon gondola, and they are connected to high voltage, high input impedance preamplifiers (see section 2.2.3) housed inside the gondola by Teflon coaxial cable (RG-188). The coaxial shield is driven by the unity gain op amp output to eliminate a voltage drop between the inner and outer conductors of the cable thus preventing a large load capacitance from forming and at the same time reducing leakage current. The total voltage difference between probes, divided by the separation distance between the probes (1.56 m on the vertical axis and 2.0 m on the horizontal axis) is the vector electric field component, E_z or E_x. Four vertical metal plates are placed around the gondola to form a symmetric ground configuration for the probes (see Figure 2.2 for a sketch of the sprite payload configuration). The vertical probes can measure fields up to about 154 V/m with a resolution of about 0.08 V/m, and the horizontal probes can measure fields up to about 120 V/m with a resolution of about 0.06 V/m. This gives a maximum two component field magnitude of about 195 V/m. Note that the instrument could measure higher electric fields

by reducing the probe separation. However, this is limited by the requirement that the probes must be far enough from the central payload to sufficiently reduce field distortions caused by the gondola structure.

The LV detector is like the HV detector but designed to measure smaller fields with better resolution. The LV probes are 30 cm diameter spheres placed on six booms to give voltage difference measurements up to ±30 V along three independent directions, hence a vector electric field measurement. The vertical low voltage probes are separated by 3.08 m and measure fields up to 10 V/m with a resolution of 0.005 V/m (0.001 V/m for ac vertical channel), and the horizontal probes are separated by 3.6 m and measure fields up to 8 V/m with a resolution of 0.004 V/m (0.001 V/m for ac horizontal channel). See Figure 2.2 for a sketch of the sprite payload configuration.

The HV and LV instruments measure quasi-dc and VLF ac electric fields. This is just one measurement with different sampling rates for the quasi-dc ($\sim$ 300 samples/s) and the VLF ac (20 k samples/s) fields. The quasi-dc channels utilize a low pass filter for a 3 dB attenuation at about 25 Hz, and the VLF ac channels use a band pass filter with 3 dB attenuation at about 25 Hz and 8 kHz (see Figure 2.3 for a block diagram of key components of the HV and LV detector layout). Hence the HV and LV detectors provide both a quasi-dc and a VLF ac waveform for lightning and sprite events. See Appendix A for a schematic of the HV electric field sensor.

2.2.3 The Difficulty of Stratospheric Electric Field Measurements

The High Resistance of the Atmosphere

Measuring electric fields in the atmosphere is difficult since the atmospheric resistance is so large. Mozer and Serlin [1969] compute this resistance between the atmosphere and a charge collecting probe to be

$$R_{atm} = \frac{m_i \nu_i}{4\pi n_i e^2 r_0} \tag{2.1}$$

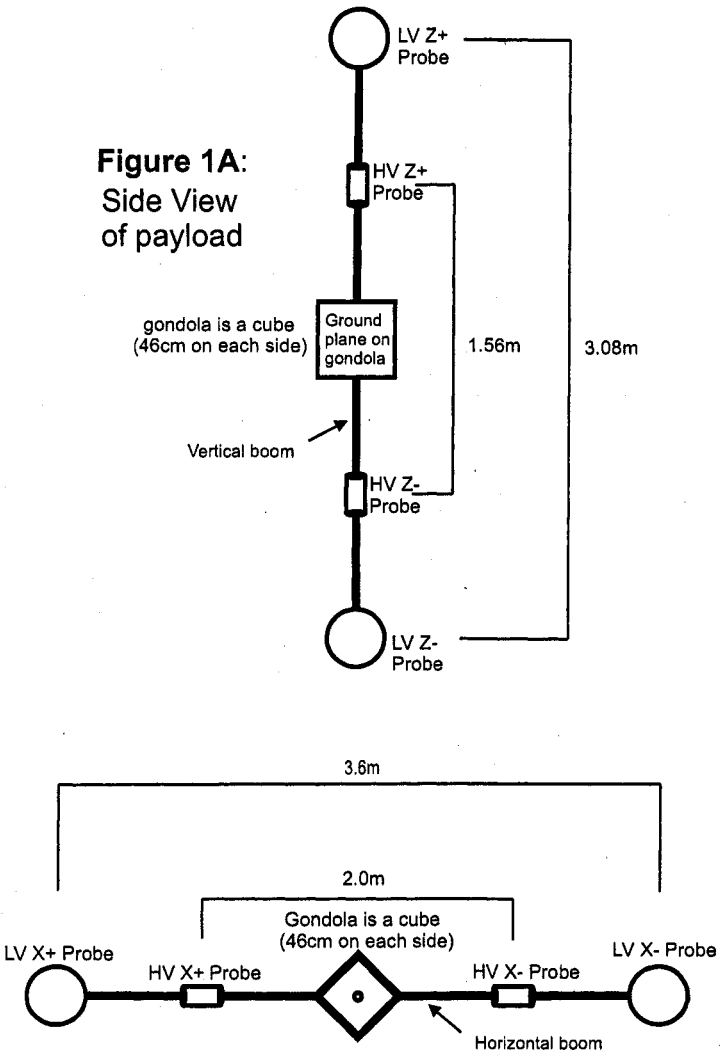

Figure 2.2: Sketch of the sprite payload configuration (not to scale). **(A)** Side view of the payload without the horizontal booms. The HV and LV vertical electric field probes are indicated. **(B)** Top view of the payload with only the one horizontal boom (the other horizontal boom is identical except that it has only LV probes). The HV and LV horizontal electric field probes are indicated.

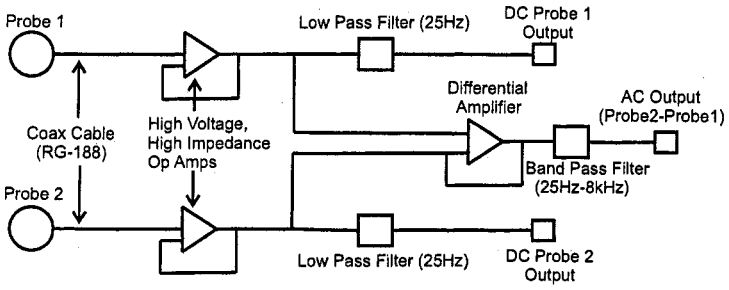

Figure 2.3: Block diagram of the key components of the HV detector layout

where m_i is the ion mass, ν_i is the ion-neutral collision frequency, n_i is the ion density, e is the charge of the electron, and r_0 is the radius of a spherical probe (note that the equation for the atmospheric resistance in Mozer and Serlin [1969] erroneously includes the neutral mass m_n rather than the ion mass m_i). Hence, for a 30 cm diameter sphere (r_0 = 15 cm) at the surface of the earth $R_{atm} \approx 10^{13}\Omega$, and at a 32 km altitude $R_{atm} \approx 10^{11}\Omega$ [Mozer and Serlin, 1969].

The Remedy: High Voltage, High Input Impedance, Operational Amplifiers

So what does this high atmospheric resistance mean for the HV electronics? In order to measure the potential difference between two points in the stratosphere accurately, there must be sufficiently high input impedance R_{in} for the electronics. If this input impedance is low compared to the atmospheric resistance R_{atm}, then the HV detector will effectively short out the field that it is trying to measure. Thus, an accurate stratospheric electric field measurement requires that $R_{in} >> R_{atm}$ [Mozer and Serlin, 1969].

Hence the key to making voltage measurements (or electric field measurements) in the atmosphere is to have a high input impedance yet still draw enough current to

drive the electronics. To accomplish this impedance transform, a high voltage, high input impedance, low output impedance operational amplifier (Apex Corporation, PA141) is connected to the probe in a unity gain voltage follower circuit (see Figure 2.3 for a block diagram of key components of the HV detector layout). By measuring the RC time constant of the op amp in series with a 10 pF capacitor, the effective input impedance of this op amp is determined to be greater than $10^{14}\Omega$, and thus $R_{in} > 10^3 \times R_{atm}$ which is more than sufficient for field measurement accuracy to within a few percent. The availability of these high voltage, high input impedance op amps allows for more than an order of magnitude increase in the dynamic range of the double Langmuir probe technique for measuring electric fields.

2.2.4 The Power Supply for the HV Detector

Two voltage measurements of up to ± 120 V, each using the op amp described in section 2.2.3, are made to calculate the potential difference up to ± 240 V between any pair of separated conductors. Instead of including costly ± 120 V batteries on the payload to power these op amps, a new dual power supply was developed, by Research Engineer John Chin, that converts +15 V to ± 120 V. This new power supply has an efficiency of about 80%, and it varies by less than 1 V in supplying approximately ± 120 V for temperatures between -70^0 and 50^0 C. This power supply can provide 6 mA at 120 V and 6 mA at -120 V, which is ample to follow rail to rail input voltages to the op amps at 10 kHz. Designed for lightweight balloon payloads, this power supply uses only 43 cm^2 of space on the HV detector printed circuit boards with a nominal mass of less than 10 g (see Table 2.1 for power supply specifications and Appendix A for the power supply schematic).

2.2.5 Comparison Between HV and LV Detectors

During Sprite Flight 1 hundreds of transient electric field perturbations were measured by the HV and Low Voltage (LV) instruments, with most of these events correlated

Table 2.1: Power supply specifications

Temperature Range Tested	-70^0 to 50^0 C
Input Voltage	15 V
Quiescent Input Current at 25^0 C	43 mA
Input Current Temperature Coefficient	< 0.2 mA/^{0}C
Output Voltage at 25^0 C	$\pm$119.4 V
Output Voltage Stability at 25^0 C	$> 99.9\%$
Output Voltage Temperature Coefficient	< 0.01 V/^{0}C
Output Voltage AC Noise	< 0.003 V RMS
Maximum Output Current (per side)	6 mA
Maximum Output Power (per side)	0.72 W
Efficiency	$\sim 80\%$
Dimensions	9.5 cm $\times$ 4.5 cm
Mass	< 10 g

with lightning events through the on-board flash detector and/or the Brazilian Integrated Network (BIN) [Pinto et al., 1998], the integration of three ground-based regional lightning detection networks that covers the southeast of Brazil (see section 2.7.2). In this section, the HV and LV detectors are compared during two time intervals when no lightning induced field perturbations occurred (since the LV detector usually saturates during periods of lightning or nearby thunderstorms) to insure that the HV instrument is accurately measuring these field perturbations. Since the HV and LV detectors have completely independent probes and electronics, this is a valid test of the new HV instrument.

Figures 2.4 and 2.5 show examples of one component of the horizontal dc electric field measured by the HV detector (panels 2.4 A and 2.5 A) and LV detector (panels 2.4 B and 2.5 B) for two different time intervals during Sprite Flight 1 on December 7, 2002. The HV horizontal field data have been multiplied by the effective antenna length factor of 0.70 to account for geometrical differences in the field caused by the different locations of the HV and LV probes relative to the ground planes on the

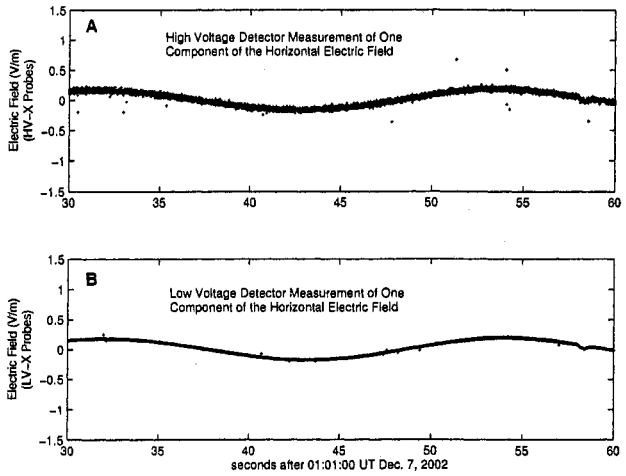

Figure 2.4: Comparison of high voltage and low voltage horizontal electric field detectors during an inactive storm period. **(A)** High voltage detector measurement of one component of the horizontal field. **(B)** Low voltage detector measurement of one component of the horizontal field.

gondola and the cylindrical shape of the HV probes. Since the LV technique has been shown to accurately measure electric fields in past experiments (as discussed in section 1.5), the HV detector was calibrated by matching its measurements to the LV detector.

Figure 2.4 presents dc horizontal field data for a 30 second interval beginning at 01:00:30 UT when there was no nearby (< 100 km) lightning activity, thus the one component of the background horizontal electric field was only about 0.175 V/m. Note that the balloon payload was rotated with a period of about 22 seconds which causes the constant single component of the horizontal field to appear sinusoidal. Since the LV detector was designed to measure smaller fields (0.004 V/m to 8 V/m) than the HV detector, variations of ± 1 telemetry unit are much more evident in the HV field data (panel 2.4 A) than the LV data (panel 2.4 B). But even for this small

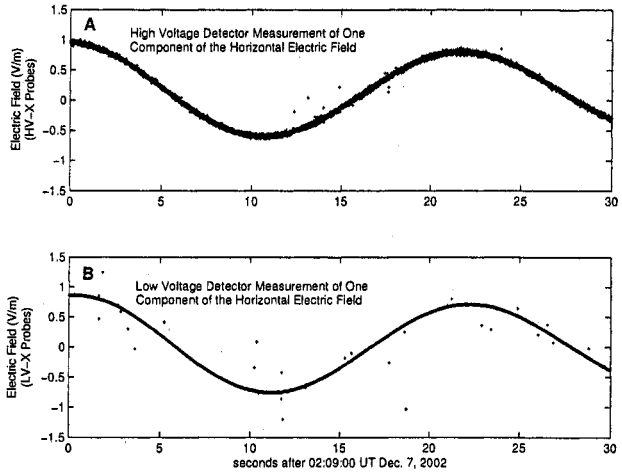

Figure 2.5: Comparison of high voltage and low voltage horizontal electric field detectors during an active storm period. **(A)** High voltage detector measurement of one component of the horizontal field. **(B)** Low voltage detector measurement of one component of the horizontal field.

background field the HV instrument (which was not optimized to measure such small fields) and LV instrument were consistent, with the rotation of the balloon seen in the field data. Figure 2.5 shows one component of the horizontal dc electric field data for a 30 second interval beginning at 02:09:00 UT when there was a strong thunderstorm nearby (< 100 km), thus the dc field was nearly 1 V/m, about six times larger than in Figure 2.4. As in Figure 2.4, the HV detector (panel 2.5 A) and LV detector (panel 2.5 B) were in good agreement, with the rotation of the payload evident. This consistency between the HV and LV detectors, which have completely separate probes and electronics, verifies that the HV instrument measurements of transient lightning electric field perturbations are reliable. Chpt. 3 includes detailed discussions of the dc to VLF electric fields measured during the Brazil Sprite Balloon Campaign.

2.3 *Conductivity Measurements*

In addition to determining the vertical electric field, the LV Z + and Z − probes measured the conductivity of the atmosphere. Since there are very few free electrons below about a 60 km altitude, the conductivity in the stratosphere is determined by ions [Volland, 1984]. These LV probes use the relaxation technique [Holzworth and Bering, 1998], where each probe is biased to a known voltage (Z+ to +2.5 V and Z− to −2.5 V) and then allowed to float back to the ambient voltage, to measure the polar conductivity. The floating voltage returns to the ambient value with an exponential time constant (known as the polar relaxation time τ^+ or τ^-) that is inversely proportional to the local conductivity.

Since the probes do not emit any current, only charge of the opposite polarity to the bias voltage is collected by each probe. Thus each probe only measures one polarity of the polar conductivity. The polar conductivity is defined as

$$\sigma^{\pm} = \Sigma_i \frac{n_i Z_i^2 e^2}{m_i \nu_i} \tag{2.2}$$

where n_i is the ion density, Z_i is the ionic charge, e is the electron charge, m_i is the ion mass, and ν_i is the ion-neutral collision frequency for the ith positive (negative) ion. The total conductivity is thus

$$\sigma = \sigma^+ + \sigma^-. \tag{2.3}$$

In terms of the polar relaxation times, the total conductivity is

$$\sigma = \epsilon_0 \left(\frac{1}{\tau^+} + \frac{1}{\tau^-} \right) \tag{2.4}$$

where ϵ_0 is the permittivity of free space. For the Sprite Balloon Campaign, the LV vertical probes were biased every 10 min to make these conductivity measurements.

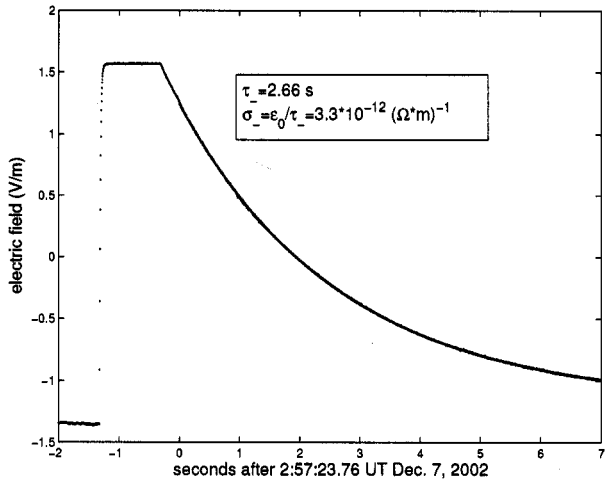

Figure 2.6: Conductivity measurement using the LV Z+ probe with data in blue and exponential fit in green.

In Figure 2.6 one of these conductivity measurements from Flight 1 is shown with the data in blue and exponential fit in green. At just before -1 s the LV Z+ probe is biased to about 2.5 V (equivalent to 1.5 V/m on this plot) and relaxes back towards the ambient electric field with a time constant of $\tau_- = 2.66$ s which gives a conductivity of $3.3 \times 10^{-12}(\Omega\text{m})^{-1}$. During periods of extremely active nearby thunderstorms, the lightning induced electric field transients prevented the probes from smoothly decaying to the ambient field, thus no conductivity data could be obtained. See Chpt. 4 for a detailed discussion of the conductivity measured during the Brazil Sprite Balloon Campaign.

2.4 ELF/VLF Magnetic Field Search Coils

The ELF/VLF magnetic search coils, provided by Professor Michael McCarthy, measured magnetic fields in the band pass between 300 Hz and 8 kHz with a full scale range of ± 15 nT. These magnetic search coils are very similar to coils developed by

Skoug [1995] that were flown on a sounding rocket experiment. Consisting of wire wrapped around a ferrite core with 12000 turns, these coils detect changing magnetic fields which induce an EMF in the wire according to Faraday's Law. These search coils are mounted on the upper boom of the balloon payload, as shown in Figure 2.1, in three perpendicular directions to make a vector ELF/VLF magnetic field measurement. This magnetic field sensor, along with the electric field instrument, allows for a measurement of the total radiated electromagnetic energy for the 300 Hz - 8 kHz band. See Chpt. 3 for examples of lightning-driven ELF/VLF magnetic fields.

2.5 X-Ray Spectrometer

The principal measurement objectives of this instrument were to obtain an x-ray spectrum over the energy range 20 keV – 650 keV at sufficiently high time resolution. The x-ray spectrometer, also provided by Professor McCarthy, consists of 2 detectors, one looking down and one up, each comprised of a scintillator coupled to a photomultiplier tube (PMT). Each NaI scintillator is a 5cm diameter × 5cm right cylinder and looks into a field of view defined by a lead collimator. Each PMT is assembled with integral potted high voltage supply and preamp on its base. The PMT outputs go to 2 separate analog chains consisting of pulse shaper and ADC. The ADC outputs are read by a single board processor which synchronizes measurements and selects and formats data products for transmission.

Only one x-ray event above the normal background, not directly correlated to lightning activity, was detected during the Brazil Balloon Campaign. Figure 2.7 (top panel) shows the downgoing (downward triangles) and upgoing (upward triangles) x-rays measured a the Flight 1 payload from 01:06:45 to 01:07:05 UT Dec, 7, 2002. The event can be seen in the downgoing x-rays from at about 01:06:53 and lasting for about 3 seconds. The middle and lower panels are the optical power and the ELF to VLF electric field measured at the payload which show no signals correlated with

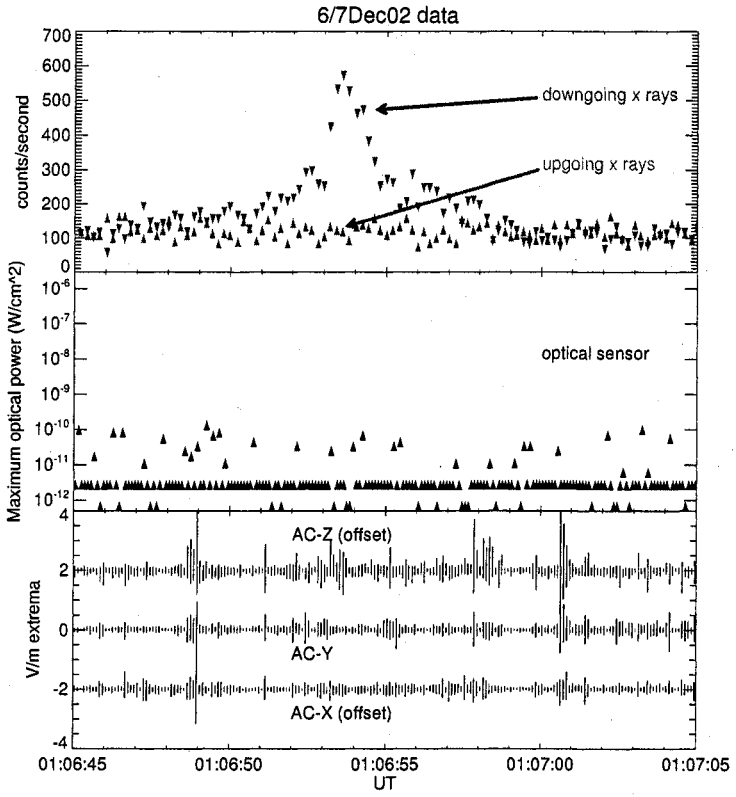

Figure 2.7: The only x-ray event above the normal background detected during the Brazil Balloon Campaign at about 01:06:53 UT Dec. 7, 2002, which was not correlated with optical power nor electric field changes (courtesy of M. McCarthy, U. of Washington).

this x-ray event. Thus, x-ray emissions due to lightning-driven relativistic runaway (see Chpt. 1.2.1) were not observed during the flights.

2.6 Optical Lightning Sensor

Two optical lightning sensors, one down looking and one up looking, were flown during the Brazil Balloon Campaign. The down looking sensor was to detect light from the

lightning flash itself, while the up looking sensor was to detect light from the possible TLEs above the payload. Unfortunately, the uplooking optical sensor did not function during Flight 1, so TLEs could not be detected. During Flight 2 no distinct signals were seen by the up looking sensor, although the data quality for this flight was poor due to ground station noise.

This instrument, developed by Research Engineer John Chin, uses optical photodiodes to observe white light transients from lightning. The proprietary design of the instrument provides for suppression of dc background light and photodiode dark current while greatly amplifying transient optical variations. This is essentially the same sensor design to be flown on the C/NOFS satellite mission [de La Beaujardiere and the C/NOFS Science Definition Team, 2004]. The spectral range is derived from that of silicon namely from about 450 nm to 950 nm. The highest sensitivity is 250 pA (500 pW optical power) and the dynamic range is four to five orders of magnitude in power. The instrument has had a long heritage of balloon, rocket and satellite applications [Li et al., 1991; Barnum, 1999].

Each of the photodiode detectors can detect optical power above 500 pW with a detecting area of about $1cm^2$ which is equivalent to a 2.5×10^6 W lightning event at 400 km distance. Since most lightning is in the range of 10^8 to 10^{11} W [Rakov and Uman, 2003, Chpt. 4], the threshold can be made less sensitive, while keeping the same four orders of magnitude dynamic range. Optical power above the top of the range is also detected for at least another order of magnitude, but the output is no longer proportional to the square root of the input power. The sensitivity available from this sensor allows detection of all types of lightning, big and small from any distance up to thousands of km (see Li et al. [1991]). In Chpt. 3, optical power measurements of lightning events during the Brazil Campaign are presented.

2.7 Sprite Imaging and Ground-Based Lightning Detection

2.7.1 Sprite Imaging

Several cameras, provided by Michael Taylor of Utah State University, were used for this study including two image intensified Isocon systems and one intensified Xybion camera. Sprites were imaged both from the ground and aircraft during the campaign [Pinto et al., 2004] as shown in Figure 1.7, but unfortunately not during the times of the two balloon flights due to cloud coverage (Flight1) and severe local weather (Flight 2).

2.7.2 Brazilian Integrated Lightning Network (BIN)

Cloud-to-ground (CG) lightning location information was provided by Professor Osmar Pinto of INPE using the Brazilian Integrated Lightning Network (BIN), which includes LPATS and IMPACT sensors, and covers the southeast of Brazil [Pinto et al., 1998]. The network is similar to the NLDN network in the U. S. and provides both lightning location and peak current data on CG strokes. Electric field measurements that are correlated with CG strokes detected by BIN are presented in Chpt. 3.

2.7.3 The World Wide Lightning Location Network (WWLLN)

The World Wide Lightning Location Network, operated by the University of Washington and Low Frequency Electromagnetic Research Ltd., overcomes the limitations of satellite-based or regional-based lightning detection systems by using the time of group arrival of VLF lightning spherics to locate both CG and IC strokes. This relatively low cost network continuously detects strong lightning anywhere in the world and should eventually provide real time global coverage of a majority of lightning events with location accuracy to within 10 km [Lay et al., 2004]. During Flight 2 in March 2003, at least one lightning event measured by the LV electric field sensor on

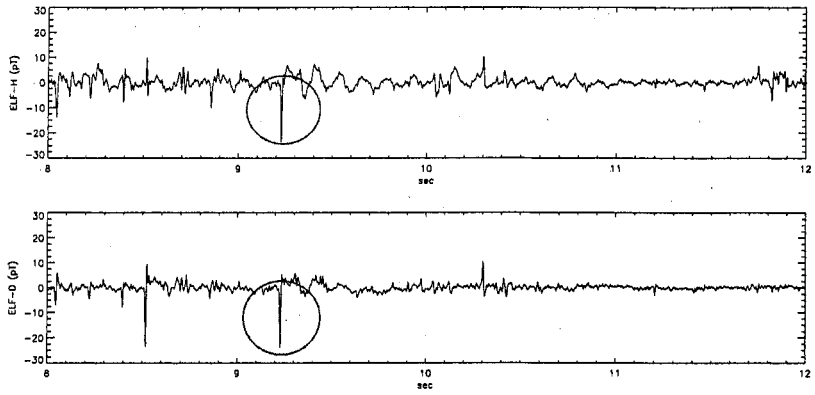

Figure 2.8: ELF magnetic field data from Syowa, Antarctica for 53 kA +CG stroke which occurred 34 km from the Flight 1 payload (courtesy of M. Sato and Tohoku University). See Chpts. 3.2 and 5 for further discussion of this lightning event.

the payload, but not indicated by BIN, was located by WWLLN to be within a few hundred km of the payload (see Lay et al. [2004, Figure 4]).

2.7.4 Remote Extremely Low Frequency (ELF) Magnetic Field Measurements

Remote ELF magnetic field (1-400 Hz) observations from Onagawa, Japan and Syowa, Antarctica, provided by M. Sato and Tohoku University [Sato et al., 2003a]), are available for a few of the lightning events detected by the balloon-borne sensors. Charge moments can be estimated from these ELF measurements, using both the impulse and fitting methods for the two stations, which gives the likelihood of a sprite occurring. Figure 2.8 shows the ELF magnetic field data from Syowa, Antarctica for 53 kA +CG stroke which occurred 34 km from the Flight 1 payload. The balloon-borne data from this +CG stroke are shown in Chpt. 3.2 and the electric field change measured is modeled in Chpt. 5.

2.8 Subsystems of the Brazil Sprite Balloon Campaign

2.8.1 Telemetry system

The telemetry used for the Brazil Balloon Campaign, developed by Professor Timothy Chinowsky, was 3 Mbps BPSK-encoded system at 902 MHz amateur band. The receiving antennas were a yagi antenna and a parabolic dish antenna (for long range receiving), each with a preamp, coupled into a receiver. The video output was bitsynced and pumped into a laptop computer. The data words were transferred continuously over an isolated LAN to a fast laptop where the ground station program was done in Lab Windows (so it was very easy to adjust if changes were made to the logical record structure.) The raw, bit synced data were recorded on hard drives, with a single flight generating over 20 GB of data. As backups, 200 GB external Kanguru disk drives are also used (both internal and external drives were recorded block by block at the same time). The balloon payloads were tracked to a distance of 426 km (the line of site horizon) during the Flight 1 and 267 km during Flight 2.

2.8.2 Power

Power for these relatively short (< 24 hour) flights came from lithium batteries. Multiple D-cell packs were used to drive a set of regulators. This was intrinsically low noise compared to a dc-dc converter, and allowed for a high degree of isolation between power consumption at different voltages. The payload had a star point ground connected to a ground plane surrounding the central payload [Holzworth, 1977]).

2.8.3 Aspect Magnetometer

DC to 100 Hz aspect magnetometers provided the orientation of the electric and magnetic fields measured relative to the geomagnetic field.

2.8.4 Rotation Motor

The entire payload was rotated using a dc motor mounted to the upper boom. This motor was the same as those used during previous thunderstorm balloon experiments (Globe Motors model 5A561-10) with a rotation speed of about 3 RPM. The purpose of the rotation motor was to allow accurate determination of the primary horizontal electric field. Rotating the booms through a quasi-dc electric field produced a sinusoidal voltage oscillation, which allowed for the elimination of any dc offsets caused by probe imbalances.

2.8.5 GPS and Housekeeping Measurements

A standard GPS board was flown with each payload, which allowed payload location information to be incorporated directly into the telemetry. External air temperature was directly measured with a bead thermistor. Other housekeeping voltages were included in the telemetry to allow accurate monitoring of power supply, internal temperatures, and reference voltages.

Chapter 3

ELECTRIC AND MAGNETIC FIELD MEASUREMENTS DURING THE BRAZIL SPRITE BALLOON CAMPAIGN

This chapter presents the lightning-driven electric and magnetic field changes measured in the stratosphere during the Brazil Balloon Campaign. Section 3.1 gives statistics of the all of the field changes correlated with cloud-to-ground (CG) lightning detected by BIN. Case studies of nearby (< 75 km) +CG, -CG, and cloud lightning events are provided in section 3.2 to examine the hypothesis that sprites are the result of large quasi-electrostatic fields (as described in Chpt. 1.3.1). Section 3.3 presents case studies of two distant (75-600 km) lightning events that are compared to the results of the Sprites99 Campaign [Bering et al., 2004b]. Cloud-to-ground stroke delayed pulses that may indicate current flowing in the mesosphere are examined in section 3.4.

3.1 Statistics of Electric and Magnetic Field Measurements

3.1.1 Overview

Thousands of lightning-driven electric and magnetic field changes were measured at altitudes of 30-35 km during Flight 1 (Dec. 6-7, 2002) and Flight 2 (March 6-7, 2003) of the Brazil Sprite Campaign. The CG lightning detected by the Brazilian ground based network (BIN) within 50 km, 100 km, and 150 km of Flight 1 are shown in Figure 3.1. Figure 3.2 is a GOES8 IR satellite image at 23:45:00 UT Dec. 6, 2007 of southeastern Brazil with a magnification of the particular storm cell that Flight 1 flew over from about 23:20:00 Dec. 6 to 00:45:00 UT Dec. 7. All of the nearby

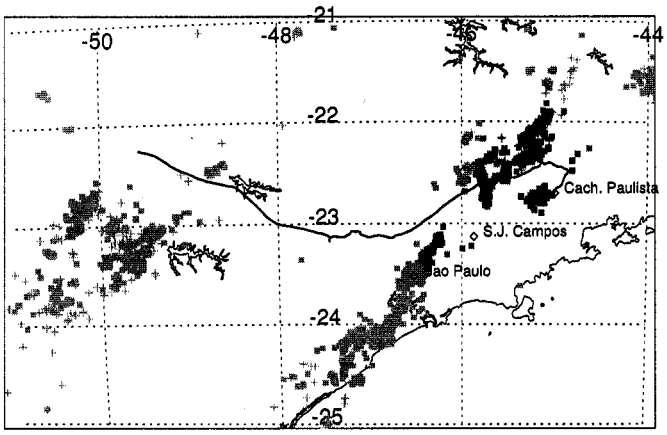

Figure 3.1: Flight 1 balloon trajectory, along with lightning strokes (+ for +CGs, and boxes for -CGs) recorded by the BIN Network within 50 km (darkest), 100 km or 150 km (lightest) of the balloon position.

(< 75 km) lightning events were generated by this cell. Figure 3.3 shows 80 minutes of the vertical dc electric field during the waning side of the first storm encountered during Flight 1. The background dc electric field decreased from about 50 V/m to about zero during this period, with the -CG field changes (upward spikes) and +CG and cloud discharge field changes (downward spikes) evident. The two largest field changes measured occurred at about 00:00:09 and 00:16:03 UT and were correlated with +CG flashes measured by BIN. There were 38 vertical electric field changes greater than 10 V/m with 11 of these detected by BIN and two of these detected by the remote ELF measurements from Antarctica and Japan. For this entire flight, the +CG and cloud discharge field changes are generally larger than the -CG field changes, which is apparent in the 80 minute field record of Figure 3.3 .

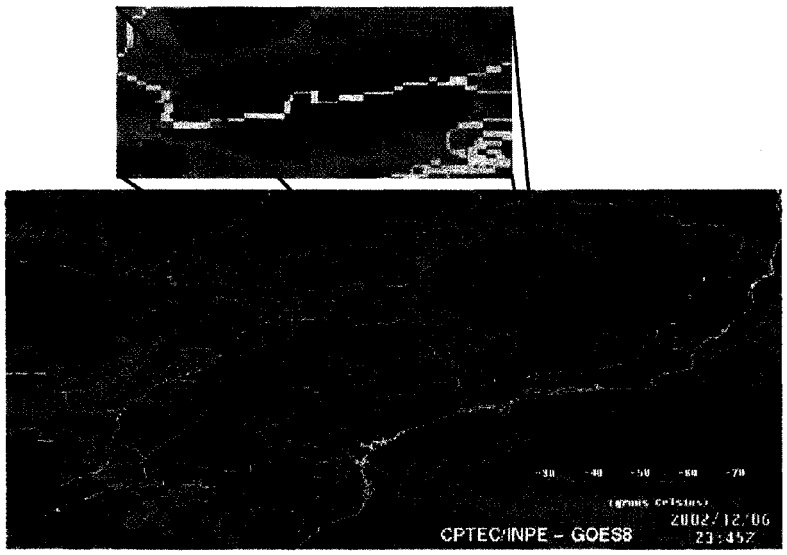

Figure 3.2: GOES8 IR satellite image of southeastern Brazil at 23:45:00 UT Dec. 6, 2002 (courtesy of CPTEC, Brazil). The storm cell that Flight 1 flew over is magnified.

3.1.2 Statistics of Nearby (< 75 km) CG Lightning Events

Electric fields (< 25 Hz) driven by CG lightning strokes and measured by Flight 1 in the stratosphere within 75 km horizontal distance (as detected by BIN) are dominated by the quasi-electrostatic field (QSF) that forms in the atmosphere due to redistribution of charge after the removal of cloud charge (see equation (1.3) term 1). Theories suggest that if these quasi-static electric fields surpass the breakdown threshold of air, which decreases linearly with the neutral density, an electric discharge observed as a sprite can occur. Thus, the foremost objective of the Brazil Balloon Campaign was to measure these nearby lightning-driven electric fields.

During Flight 1, 200 nearby (< 75 km horizontal distance) CG lightning strokes were measured at 30-35 km in altitude including 15 +CGs. See Table 3.1 for a summary of these nearby event statistics. Note that for a few of the +CGs and many

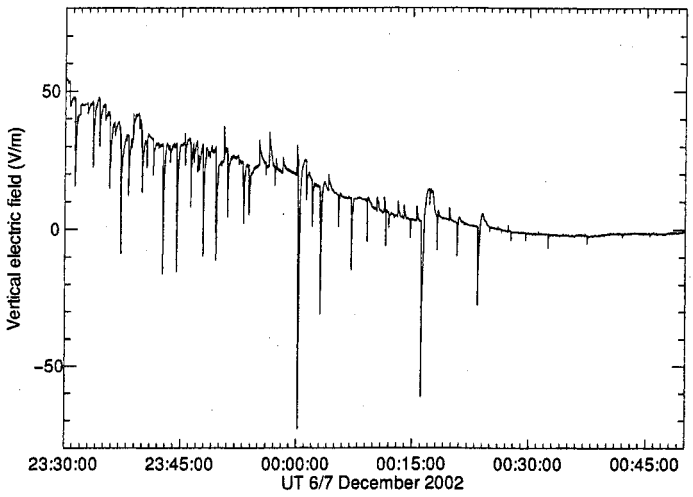

Figure 3.3: Eighty minutes of dc vertical electric field data during Flight 1. The two largest field changes measured occurred at about 00:00:09 and 00:16:03 UT, seen as large negative transients, and were correlated with +CG flashes measured by BIN

Table 3.1: Nearby (< 75 km) lightning statistics

	+CGs	-CGs
total number	15	185
mean (median) peak current	24.1 (18.0) kA	-19.7 (-17.0) kA
mean (median) distance	42.3 (36.8) km	46.0 (47.8) km
mean (median) ΔE_z	22.8 (10.4) V/m	6.1 (3.9) V/m
mean (median) ΔE_{tot}	31.0 (15.6) V/m	8.7 (6.1) V/m

of the -CGs, there were multiple return strokes, so that the quasi-electrostatic field change measured is result of the sum of these return strokes.

An important characteristic of these near-field statistics is that the mean electric field change is almost 4 times greater for the +CGs than the -CGs, even though +CGs and -CGs had similar mean peak currents and horizontal distances. Although this is a small data set and these statistics have not been normalized for the different

horizontal distances and peak currents of the CG strokes, these statistics suggest that +CG lightning flashes on average drive larger quasi-static nearby electric fields than -CG flashes. This is presumably because of the larger charge moments associated with +CGs compared to -CGs. Since sprites are almost exclusively correlated with +CGs, these statistics agree with the theory that sprite production is related to a large quasi-electrostatic field that forms after a +CG stroke.

3.1.3 Statistics of Distant (75 – 600 km) CG Lightning Events

Electric and magnetic fields driven by CG lightning strokes and measured by Flight 1 in the stratosphere at horizontal distances greater than about 75 km (as detected by BIN) are dominated by the induced fields due to the current flowing in the lightning stroke and radiated fields due to the time derivative of this current (see equation (1.3), terms 2 and 3 and equation (1.4) terms 1 and 2). Although these induced and radiated fields, which only exist for a few ms, are presumably not capable of generating sprites that often occur many ms after the parent CG stroke (see Chpt. 1.2), they can be used as remote sensors of the lightning current and sometimes the sprite current [Cummer et al., 1998]. Note that the radiated energy from lightning is likely responsible for TLEs known as elves seen in the lower ionosphere, as discussed in Chpt. 1.2. This data set includes ELF to VLF electric fields (25 Hz-8 kHz) and magnetic fields (300 Hz-8 kHz) measured by the LV electric field sensor and magnetic search coils (see Chpt. 2 for descriptions of these sensors).

The vector electric fields driven by 2467 CGs at horizontal distances of 75-600 km from the payload were measured including 429 +CGs. These 2467 CGs were all of the CGs that occurred at this distance during times when the balloon sensors and telemetry system were working properly, thus every CG produced ELF/VLF electric field signals with peak power at about 300 Hz to 1 kHz. Statistics for these events are summarized in Table 3.2. Note that the average total peak-to-peak electric field magnitude of the -CGs was about 60% larger than the +CGs, which is likely due to

Table 3.2: Distant (75 – 600 km) lightning statistics for all 2467 CGs

	+CGs	-CGs
total number	429	2038
mean (median) peak current	33.1 (26.0) kA	-35.2 (-29.0) kA
mean (median) distance	457.5 (476.9) km	435.5 (485.4) km
mean (median) ΔE_z	0.298 (0.207) V/m	0.443 (0.291) V/m
mean (median) ΔE_{hor}	0.177 (0.116) V/m	0.321 (0.161) V/m
mean (median) ΔE_{tot}	0.350 (0.248) V/m	0.555 (0.334) V/m

the slightly larger average peak current and average horizontal distance for the -CGs compared to the +CGs. This is different from the nearby lightning which drove much larger electric field changes for +CGs compared to -CGs.

For 858 of these 2467 CGs, both the vector electric and magnetic fields were measured. That is, only about 35% of these distant CGs drove a measurable magnetic field change due to the high noise level of the magnetic field search coils. Presumably, all of the CGs drove magnetic field changes but only 858 of them produced signals above this noise level. Statistics for these events are summarized in Table 4.3 with error bars included with the mean values of the magnetic field components and magnitude due the large signal-to-noise ratio.

Note that this subset of events that produced a detectable magnetic field change had an 31% larger average peak current compared to all 2467 CGs, which suggests that the larger peak current CGs produced the larger magnetic field changes that were able to be measured above the noise. Table 3.3 also gives the ratio of the total electric field to the total magnetic field (E_{tot}/B_{tot}) for these ELF/VLF measurements, with the speed of light (2.99×10^8 m/s) falling within the error bars for both the +CGs and -CGs, which suggests that our field measurements were calibrated properly. The large errors in E_{tot}/B_{tot} are due to the high background noise level in the magnetic field data. Also note that these statistics for distant lightning disagree with the Sprites99

Table 3.3: Distant (75 – 600 km) lightning statistics for 858 CGs with measurable magnetic field changes

	+CGs	-CGs
total number	112	746
mean (median) peak current	50.5 (40.5) kA	-45.0 (-36.0) kA
mean (median) distance	436.6 (431.5) km	374.5 (433.9) km
mean (median) ΔE_z	0.536 (0.454) V/m	0.715 (0.607) V/m
mean (median) ΔE_{hor}	0.338 (0.265) V/m	0.572 (0.369) V/m
mean (median) ΔE_{tot}	0.642 (0.537) V/m	0.929 (0.745) V/m
mean ΔB_z	0.281 ± 0.150 nT	0.270 ± 0.150 nT
mean ΔB_{hor}	2.377 ± 0.558 nT	3.623 ± 0.556 nT
mean ΔB_{tot}	2.577 ± 0.550 nT	3.928 ± 0.539 nT
mean E_{tot}/B_{tot}	$4.337 \pm 2.162 \times 10^8$ m/s	$3.752 \pm 1.479 \times 10^8$ m/s

balloon campaign results [Bering et al., 2002, 2004a,b; Bhusal et al., 2004], which rarely measured the ELF electric or magnetic field driven by distant lightning. This is further discussed in sections 3.3 and 3.4 and Chpt. 6

3.2 Case Studies of Nearby (< 75 km) Lightning Events

3.2.1 Nearby Positive Cloud-to-Ground Lightning Events

In this section, the two largest electric field changes measured, correlated with +CG flashes detected by BIN, will be examined in detail, with discussion of both the electric and magnetic field changes correlated with these events.

The largest electric field change measured occurred at an altitude of about 34 km at about 00:00:09 UT December 7, 2002 with a vertical dc field perturbation of $E_z \approx -101$ V/m (the negative vertical field value indicates a field directed downward, towards the earth) and a horizontal dc field perturbation of $E_x \approx 79$ V/m. This field perturbation, the largest reported in the stratosphere above 30 km, correlated with two cloud-to-ground lightning strokes, a +15 kA stroke (peak current) at

00:00:09.05 UT about 33.2 km from the payload (horizontal distance) and a +53 kA stroke at 00:00:09.19 UT about 34.4 km from the payload, detected by BIN.

Figure 3.4 shows the HV detector dc electric field data and the optical lightning data for these lightning events. The large vertical (panel 3.4 A) and single component of the horizontal (panel 3.4 B) dc electric field perturbations occurred simultaneously with the lightning strokes detected by BIN, indicated by dashed vertical lines on the figures, and the optical power data (panel 3.4 C). The +15 kA and +53 kA strokes perturbed the vertical dc field by $E_z \approx -32$ V/m and $E_z \approx -69$ V/m respectively, and these strokes perturbed the single component of the horizontal dc field by $E_x \approx$ 42 V/m and $E_x \approx 37$ V/m respectively. Thus the dc field perturbations add up to fields of $E_z \approx -101$ V/m and $E_x \approx 79$ V/m. These dc fields decayed slowly, taking more than 10 seconds, or a few times the local relaxation time, to return to background values. Since the HV electric field sensor (see Chpt. 2) only measured one horizontal component of the field, there is no advantage in transforming these field measurements into stroke-centered cylindrical coordinates since parts of the radial and azimuthal components would be missing. Note that the horizontal field for this +CG event was measured at an azimuthal angle of about 46^0 from the location of the +CG given by BIN.

Figure 3.5 shows the ac electric field data from the HV detector along with the optical power data for these lightning events. The vertical and single component horizontal ac electric field perturbations (panel 3.5 A) occurred simultaneously to the lightning strokes, just as in Figure 3.4. Note that the BIN lightning strokes are again shown as dashed vertical lines, and that an additional three strokes are included here that occurred after the two strokes of interest. These three strokes had little effect on the electric fields but can be seen in the optical lightning data (panel 3.5 B). The vertical and single component horizontal ac field changes that correspond with the +15 kA and +53 kA strokes were similar in magnitude to the dc field changes shown in Figure 3.4. Hence, low frequency components dominated the electric field signature

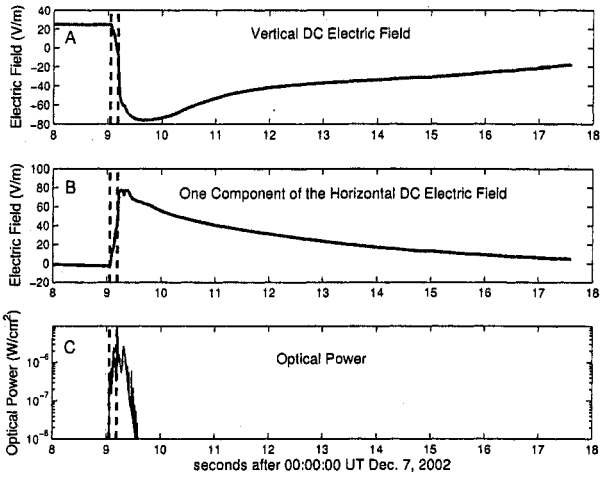

Figure 3.4: Two lightning events, +15 kA and +53 kA, at ~00:00:09 UT Dec. 7, 2002 located ~33.2 km and ~34.4 km horizontal distance from the payload respectively measured at an altitude of 33.9 km. **(A)** Vertical dc electric field. **(B)** One component ($\phi = 46^0$ from +CG) of the horizontal dc electric field. **(C)** Optical power. The two lightning stroke times are indicated by the the dashed vertical lines.

of these strokes. In Chpt. 5, this quasi-electrostatic field change driven by these +CG events is compared directly to a numerical model, and the best fit parameters to this comparison are used to predict the electric fields at altitudes where sprites initiate and grow.

Figure 3.6 is 12 ms of ELF to VLF (300 Hz - 8 kHz) magnetic field data from the magnetic search coil for the +53 kA stroke (second stroke in Figure 3.5) in stroke-centered cylindrical coordinates. The dashed vertical line is the retarded time at the payload of the +CG stroke. The azimuthal component of the magnetic field transient was dominant because a CG return stroke is essentially an impulsive vertical current that flows from the cloud to the ground, which induces and radiates a magnetic field that curls around this vertical channel. The positive polarity of the stroke dictated that the magnetic field curled clockwise around the return stroke, which is

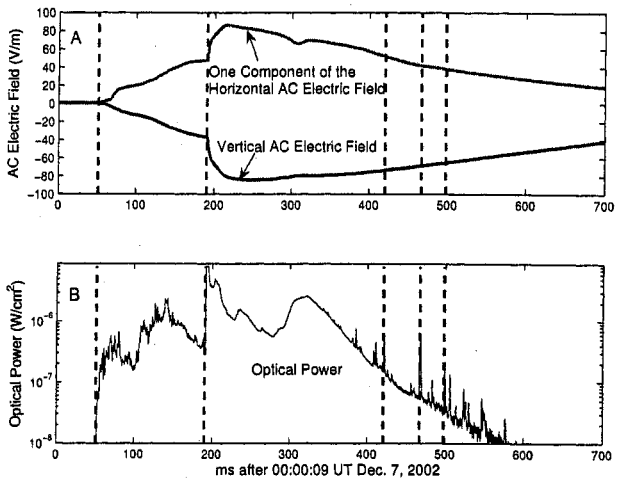

Figure 3.5: Two lightning events, +15 kA and +53 kA, at ~00:00:09 UT Dec. 7, 2002 located ~33.2 km and ~34.4 km horizontal distance from the payload respectively measured at an altitude of 33.9 km. **(A)** Vertical and horizontal (one component, $\phi = 46^0$ from +CG) ac electric field. **(B)** Optical power. Dashed vertical lines indicate lightning stroke times, note that three additional strokes are included here after the two strokes of interest.

seen as the initial negative field change in the azimuthal component. The smaller, but significant, radial and vertical components of the magnetic field transient may suggest that there was a significant horizontal component to the +CG return stroke. This agrees with other studies [Williams, 1998] that have suggested that +CG strokes tap large reservoirs of positive charge via horizontal channels that allows for the large net removal of charge, and hence the large charge moments of some +CG strokes. But this radial component may have partially been due to the uncertainty in the exact location of the lightning channel causing a small error in the transform to stroke centered coordinates, thus allowing the azimuthal magnetic field transient to appear as a radial component. The large vertical magnetic field component may have also been due to the nearby nature of the stroke. The payload was about 25-30 km above the cloud charge center and only 34.4 km away horizontally or an angle of about

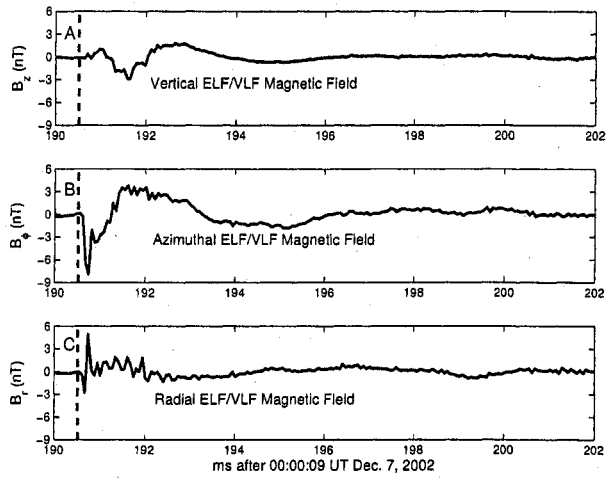

Figure 3.6: The ELF/VLF magnetic field transient from a 53 kA +CG lightning stroke located 34.4 km horizontal distance from the payload measured at an altitude of 33.9 km. The vertical (**A**), azimuthal (**B**), and radial (**C**) components of the magnetic field in stroke-centered cylindrical coordinates. The dashed vertical line is the retarded time at the payload of the +CG stroke.

$36^0 - 41^0$ from the top of the vertical current channel to the payload. When mapping the magnetic field due to the impulsive vertical current to this location a vertical component is expected.

The second largest field change measured occurred about 16 minutes after the events described above, at an altitude of about 34 km at about 00:16:03 UT December 7, 2002 with a vertical dc field perturbation of $E_z \approx -64$ V/m and a horizontal dc field perturbation of $E_x \approx 30$ V/m. This field perturbation was correlated with two CG lightning strokes, a +42 kA stroke at 00:16:03.20 UT about 50.7 km from the payload (horizontal distance) with an azimuth of $\phi = -29^0$ relative to the horizontal axis and a +56 kA stroke at 00:00:16.03.585 UT about 47.4 km from the payload with $\phi = -100.5^0$, detected by BIN. The dc and ac electric field data for this +CG event, along with optical power, are shown in Figures 3.7 and 3.8. The dc and ac vertical

data (panels 3.7 A and 3.8 A) are similar to the prior event +CG at 00:00:09 UT exemplifying how nearby (< 50 km) positive cloud-to-ground lightning strokes form large quasi-static electric fields in the stratosphere above 30 km that remain for long time periods (~ 10 s). The dc and ac horizontal data (panels 3.7 B and 3.8 A) for this event show a positive field change for the first +42 kA CG stroke and a negative field change for the second +56 kA CG stroke due to the difference in azimuthal angles from the horizontal axis to the +CG location. Note that for both of these large +CG events at 00:00:09 UT and 00:16:03 UT that the optical power measured at the payload (panels 3.5 B and 3.8 B) remained at high levels for hundreds of ms, with numerous identifiable pulses, indicating that a significant amount of in-cloud lightning occurred. This in-cloud lightning might have helped to further drive the quasi-electrostatic field changes by allowing for larger total charge moments for the lightning event. The possibility that in-cloud lightning drives large electric fields, maybe large enough to produce breakdown, is further discussed in section 3.2.3 .

Figures 3.9 and 3.10 are 12 ms of ELF to VLF magnetic field data from the magnetic search coil for the +42 kA CG stroke and +56 kA CG stroke (respectively) that occurred at about 00:16:03 UT in stroke-centered cylindrical coordinates. The dashed vertical lines are the retarded times at the payload of the +CG strokes. Just as in Figure 3.6 for the earlier +CG event, the azimuthal components of the magnetic field transients were largest with initial negative changes in agreement with positive polarity CG strokes. The radial and vertical components for the events in Figures 3.9 and 3.10 are smaller than the earlier event in Figure 3.6 which may indicate that the earlier event included larger horizontal components to the lightning current.

3.2.2 A Nearby Negative Cloud-to-Ground Lightning Event

The largest quasi-electrostatic field change due to a -CG event occurred at about 23:26:30.5 UT Dec. 6, 2002 at a distance of about 22.8 km while the payload was at an altitude of 30.8 km. This -CG flash consisted of at least four return strokes

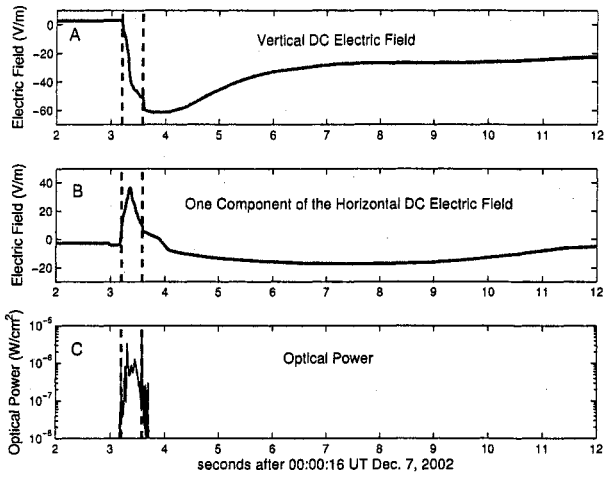

Figure 3.7: Two lightning events, +42 kA and +56 kA, at ~00:16:03 UT Dec. 7, 2002 located ~50.7 km and ~47.4 km horizontal distance from the payload respectively measured at an altitude of 33.4 km. **(A)** Vertical dc electric field. **(B)** One component ($\phi = -29^0$ and -100.5^0 from +CGs) of the horizontal dc electric field. **(C)** Optical power. The two lightning stroke times are indicated by the the dashed vertical lines.

(23, -14, -17, and -9 kA) which occurred in about the same location within a time interval of about 0.7 s. Figures 3.11 and 3.12 are the dc and ac electric field data, along with optical power for this -CG flash. The total vertical (panels 3.11 A and 3.12 A) and horizontal (panels 3.11 B and 3.12 A) electric field changes for this -CG flash were $E_z \approx 32.5$ V/m and $E_x \approx -29.5$ V/m, with the positive polarity of the vertical component in agreement with negative polarity of the CG flash. This largest -CG driven field change was less than 33% of the largest +CG event (Figures 3.4 and 3.5) even though the -CG flash was significantly closer (22.8 km) than the +CG flash (34.4 km). This, along with the statistics that more than 90% of the nearby lightning measured by the payload were -CG strokes (see section 3.1), agrees with previous ground-based observations (see Cummer and Lyons [2005]) that large charge moment -CG strokes are rare (at least over land). Thus, on average, -CG strokes drive

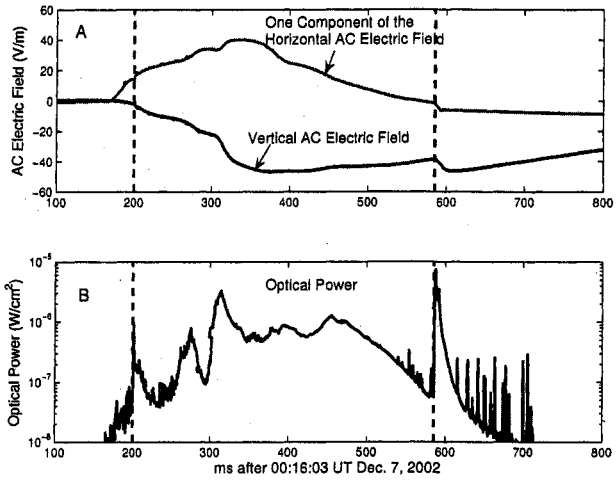

Figure 3.8: Two lightning events, +42 kA and +56 kA, at ~00:16:03 UT Dec. 7, 2002 located ~50.7 km and ~47.4 km horizontal distance from the payload respectively measured at an altitude of 33.4 km. **(A)** Vertical and horizontal (one component, $\phi = -29^0$ and -100.5^0 from +CGs) ac electric field. **(B)** Optical power. Dashed vertical lines indicate lightning stroke times.

smaller quasi-electrostatic field changes compared to +CG strokes, at least for this small sample of data. Note that for this event at 23:26:30.50 UT the optical power (panel 3.12 B) indicates that significant amounts of lightning were occurring at times not indicated by BIN. This could be either in-cloud lightning or CGs missed by the BIN. Hence, in-cloud lightning could have helped to drive the quasi-static field change for this -CG event.

Figure 3.13 is 12 ms of ELF to VLF magnetic field data from the magnetic search coil for the -14 kA stroke (second stroke in Figure 3.13 in stroke-centered cylindrical coordinates). The dashed vertical line is the retarded time at the payload of the -CG stroke. The azimuthal component was again largest, but for this event the initial field change was positive which is an agreement with a upward flowing vertical current or -CG stroke. The small amplitude of radial and vertical components of the magnetic

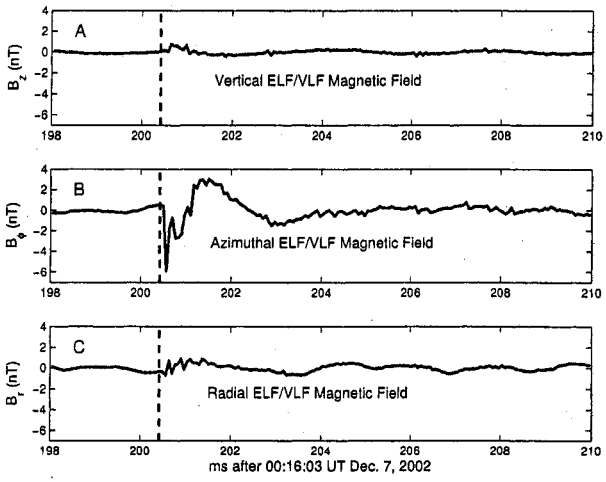

Figure 3.9: The ELF/VLF magnetic field transient from a 42 kA +CG lightning stroke located 50.7 km horizontal distance from the payload measured at an altitude of 33.4 km. The vertical (**A**), azimuthal (**B**), and radial (**C**) components of the magnetic field in stroke-centered cylindrical coordinates. The dashed vertical line is the retarded time at the payload of the +CG stroke.

field suggests that the lightning channel for this -CG stroke was mostly vertical. Hence, this -CG stroke was likely not capable of tapping into a large reservoir of charge like the previous +CG events, and thus had a smaller charge moment and quasi-static field change.

3.2.3 A Nearby Possible Cloud Lightning Event

Of the 38 vertical electric field changes measured by Flight 1 that were larger than 10 V/m, 27 of these were not correlated with a CG stroke detected by BIN. Of these 27 events, 26 of them were negative vertical electric field changes which are consistent with either +CG strokes or cloud discharges, but not -CG strokes. Hence, these 26 events could have been cloud lightning, small +CG strokes that are excluded from the BIN data, or other larger +CG strokes that BIN failed to detect. Since BIN

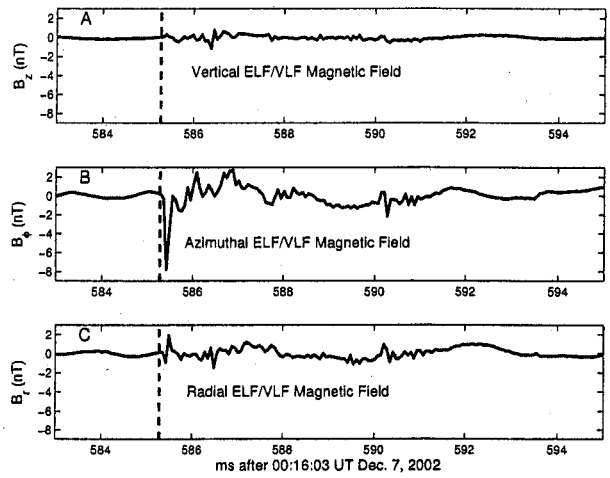

Figure 3.10: The ELF/VLF magnetic field transient from a 56 kA +CG lightning stroke located 47.4 km horizontal distance from the payload measured at an altitude of 33.4 km. The vertical (**A**), azimuthal (**B**), and radial (**C**) components of the magnetic field in stroke-centered cylindrical coordinates. The dashed vertical line is the retarded time at the payload of the +CG stroke.

detects about 80% of CGs (excluding +CG with peak currents below 10 kA) in this region of Brazil [Lay et al., 2004] and only 15 nearby +CG strokes with peak current greater than 10 kA were detected by BIN during Flight 1, it is most likely that these 26 events were either cloud lightning or small +CG strokes. In this section, data from a possible cloud lightning discharge, correlated with the largest electric field change measured by the payload without a corresponding BIN CG stroke, is presented.

Figures 3.14 and 3.15 are the dc and ac data measured by Flight 1 at about 23:37:10.3 UT Dec. 6, 2002 at an altitude of 34.5 km. The exact location of this possible cloud discharge is not known since BIN is designed to locate only CG strokes, but the location can be estimated to be within about 50 km of the payload from the location of other CGs detected by BIN within a few minutes of this event. This particular event is very likely a cloud discharge since the ELF/VLF magnetic search

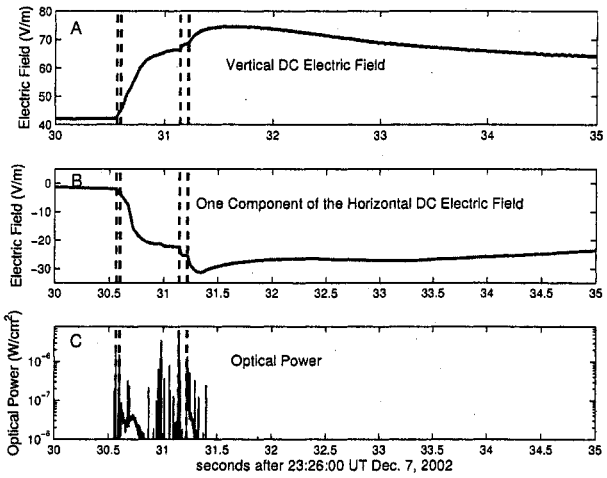

Figure 3.11: A negative lightning flash consisting of at least four return strokes, -23, -14, -17, and -9 kA at ~23:26:30 UT Dec. 6, 2002 located 22.7 km horizontal distance from the payload. **(A)** Vertical dc electric field. **(B)** One component ($\phi = 77^0$ from -CG) of the horizontal dc electric field. **(C)** Optical power. The lightning stroke times are indicated by the the dashed vertical lines.

coils failed to measure any significant field transients above the background noise during the time interval of this event, as shown in Figure 3.16. This lack of magnetic field data for this event suggests that the driving discharge did not include any return strokes, since return strokes would have caused magnetic field transients at ELF to VLF. Cloud discharges, unlike CG strokes, do not include a return stroke stage (see Chpt. 1) but do include a so called active stage with up to 100s A of a current flowing over time periods of up to 100s of ms. This low current (current time derivative) associated with the active stage failed to induce (radiate) magnetic fields large enough to be detected by the payload search coils, hence no magnetic field transients were observed during this event. To further support that this event was indeed a cloud discharge, the magnetic field driven by the lowest peak current nearby +CG detected by BIN was examined. This +12 kA stroke which occurred about 36 km horizontal

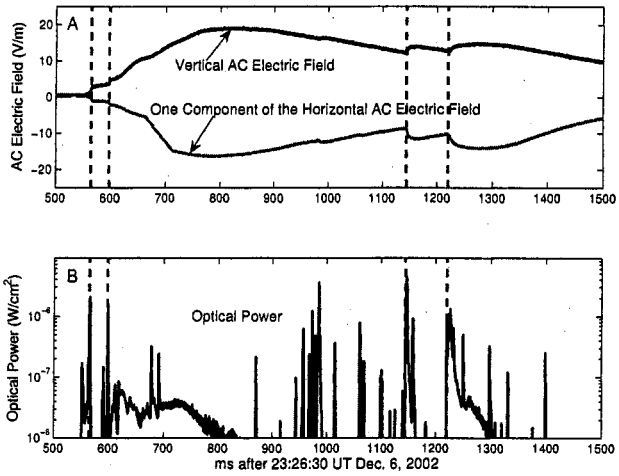

Figure 3.12: A -CG lightning flash consisting of at four least return strokes, -23, -14, -17, and -9 kA at ~23:26:30 UT Dec. 6, 2002 located 22.7 km horizontal distance from the payload measured at an altitude of 30.8 km. **(A)** Vertical and horizontal (one component, $\phi = 77^0$ from -CG) ac electric field. **(B)** Optical power. Dashed vertical lines indicate lightning stroke times.

distance from the payload drove a peak to peak azimuthal magnetic field of more than 4 nT, which is well above the background noise. By examining the electric field data (Figures 3.14 and 3.15) for the possible cloud discharge, it is evident that large amounts of charge are being distributed in the cloud to provide for the considerable electric field changes of $E_z \approx 43$ V/m and $E_x \approx 15$ V/m. Hence, this data suggest that cloud lightning is capable of driving large quasi-electrostatic field changes above thunderstorms. Unfortunately, without knowing the location of the cloud discharge, it is not possible to accurately model the effects of this cloud discharge elsewhere in the middle atmosphere, including sprite altitudes.

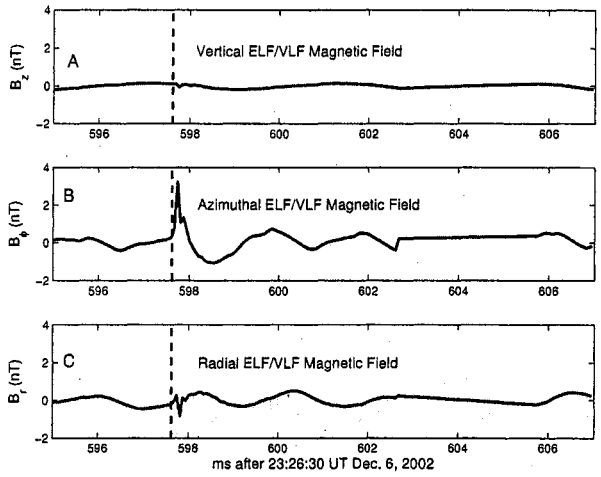

Figure 3.13: The ELF/VLF magnetic field transient from a -14 kA CG lightning stroke (the second return stroke in Figures 3.11 and 3.12 located 22.7 km horizontal distance from the payload measured at an altitude of 30.8 km. The vertical **(A)**, azimuthal **(B)**, and radial **(C)** components of the magnetic field in stroke-centered cylindrical coordinates. The dashed vertical line is the retarded time at the payload of the +CG stroke.

3.3 Case Studies of Distant (75 – 600 km) Lightning Events

In this section, two case studies of distant (75 – 600 km) lightning events, including ELF to VLF electric and magnetic field data, will be presented. At these distances, the fields measured at the balloon payload are induced and radiated fields, rather than the quasi-static electric fields that dominated the electric field data for the nearby events. The statistics for these events have already been discussed in section 3.1.3.

Figures 3.17 and 3.18 are the ELF to VLF electric and magnetic field data for a 111 kA +CG stroke that occurred at 03:01:50 UT Dec. 7, 2002 about 328 km from the payload measured at an altitude of 32.7 km. Figures 3.19 and 3.20 are data for a 101 kA +CG stroke that occurred at 08:22:39 UT (after sunrise) about 409.9 km from the payload measured at an altitude of 35.1 km. The vertical electric field (panels 3.17 A

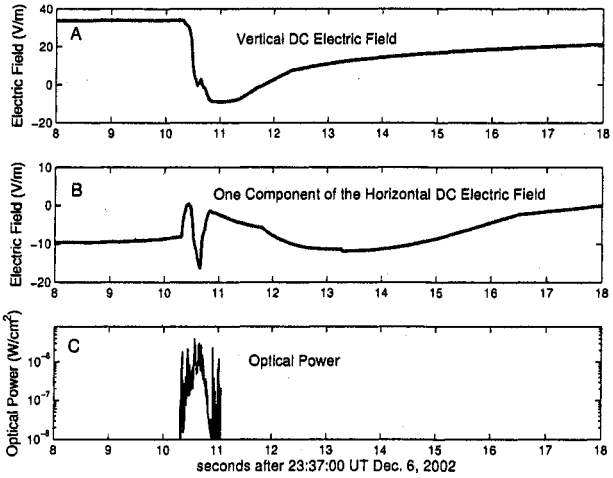

Figure 3.14: A likely in-cloud lightning event at ~23:37:10 UT Dec. 6, 2002 measured at an altitude of 34.5 km. **(A)** Vertical dc electric field. **(B)** One component of the horizontal dc electric field. **(C)** Optical power.

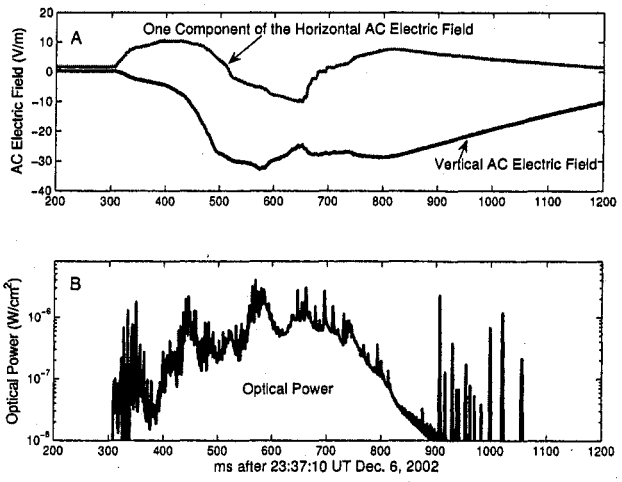

Figure 3.15: A likely in-cloud lightning event at ~23:37:10 UT Dec. 6, 2002 measured at an altitude of 34.5 km. **(A)** Vertical and horizontal (one component) ac electric field. **(B)** Optical power. Dashed vertical lines indicate lightning stroke times.

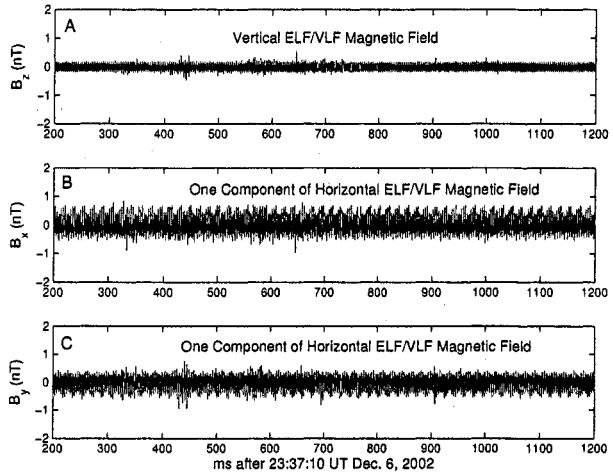

Figure 3.16: The ELF/VLF magnetic field data from an altitude of 34.5 km for the duration of the likely in-cloud lightning event. No significant signal above the background noise was measured, which suggests that no return strokes occurred, and that this is in fact a cloud discharge.

and 3.19 A) and azimuthal magnetic field (panel 3.18 B and 3.20 B) components were dominant with polarity of the transients consistent with a vertical flow of current downward, as in a +CG stroke, with ELF frequencies of a few hundred Hz dominant in both the electric and magnetic field data. The mechanism that drives the relatively large, damped oscillations present in the azimuthal and radial components of the electric field in Figure 3.17, but not observed in Figure 3.19, is not known. These damped oscillations were found in the azimuthal and radial components of some of the electric field measurements driven by distant lightning as well. For both events, the vertical electric field saturates the LV field sensor, so the peak value of this component can not be determined from these data. By examining the HV electric field sensor for these events, the peak values were determined to be 1.6 ± 0.2 V/m (+111 kA +CG) and 0.9 ± 0.2 V/m (+101 kA +CG) with the large uncertainty due to the poor sensitivity of the HV field sensor for small field changes. The electric to magnetic field

ratio for these events are $E/B \approx 2.86 \times 10^8$ and 2.37×10^8 or about 96% and 79% of the speed of light in vacuum c. While 96% of c is a reasonable value for electromagnetic radiation in the earth-ionosphere waveguide at these ELF frequencies, 79% of c is lower than expected and may be due to the HV sensor not measuring this small field change accurately.

These measurements agree well qualitatively with previous ground-based measurements [Cummer et al., 1998] and models [Pasko et al., 1998b] for ELF radiation from lightning at these distances, with vertical electric fields and azimuthal magnetic fields as the dominant components. These waveforms measured by Flight 1 have polarities and shapes very similar to the ground-based measurements and models, but have smaller amplitudes. However, the Flight 1 ELF electric and magnetic field measurements do not agree with the prior results of balloon-borne field measurements from the Sprites99 balloon campaign [Bering et al., 2002, 2004a,b; Bhusal et al., 2004]. During the Sprites99 campaign, the radiated ELF transients driven by distant lightning were very rarely measured in their electric and magnetic field instruments [Bering et al., 2004b; Bhusal et al., 2004]. Although the Sprites99 payloads had a low pass filter of 1 kHz that was below the 8 kHz filter employed on the Brazil payloads, the Brazil payload measurements, along with the ground-based measurements [Cummer et al., 1998] and models [Pasko et al., 1998b], suggest that the Sprites99 payloads should have measured the few 100 Hz ELF transients of the distant lightning. Moreover, the Sprites99 payloads measured ELF vertical electric field pulses delayed by 4-6 ms from the retarded times of the CG strokes in 90% of the NLDN CG strokes [Bering et al., 2004b; Bhusal et al., 2004]. Bering et al. [2004b] and Bhusal et al. [2004] conclude that these delayed pulses are the result of current flowing in the mesosphere after the CG stroke. In the next section, the possible examples of similar delayed pulses measured by the Brazil payloads will be presented. Further discussion of this distant lightning data can be found in Chpt. 6.2.

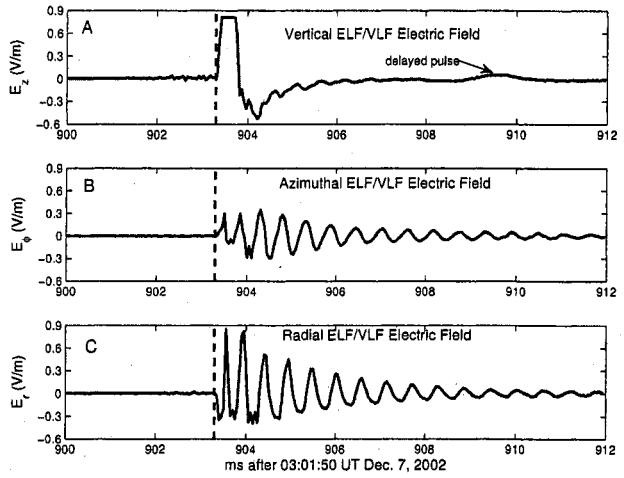

Figure 3.17: The ELF/VLF electric field transient from a 111 kA +CG lightning stroke located 328 km horizontal distance from the payload measured at an altitude of 32.7 km. The vertical (**A**), azimuthal (**B**), and radial (**C**) components of the electric field in stroke-centered cylindrical coordinates. The dashed vertical line is the retarded time at the payload of the +CG stroke.

3.4 Possible CG Delayed ELF Pulses due to Mesospheric Currents

As mentioned in the last section, the Sprites99 balloon campaign measured delayed ELF vertical electric field pulses (delays 4-6 ms longer than the speed of light travel time) in 90% of the NLDN CG strokes within about 200-1700 km of their payloads [Bering et al., 2004b; Bhusal et al., 2004], which they attributed to current flowing in the mesosphere. In this section, possible evidence of mesospheric current in the ELF/VLF electric and magnetic field data measured by the Brazil balloon payloads is presented. Furthermore, the statistics of these cloud-to-ground stroke delayed ELF pulses and the likelihood that these pulses were actually the result of mesospheric current is discussed.

The best examples of CG delayed ELF pulses in the Brazil Balloon Campaign data are the 111 kA and 101 kA +CG strokes examined in the previous section and

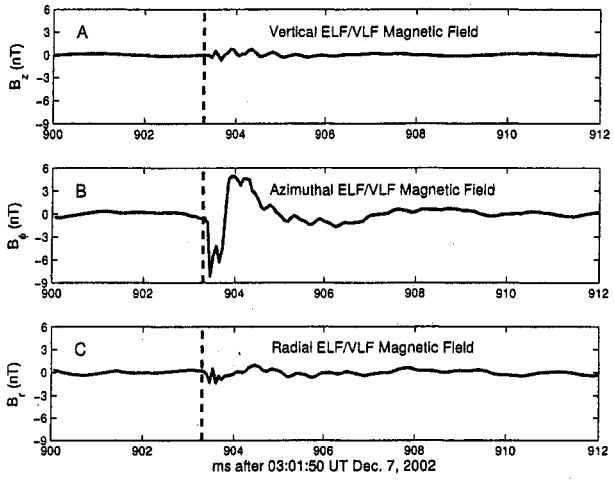

Figure 3.18: The ELF/VLF magnetic field transient from a 111 kA +CG lightning stroke located 328 km horizontal distance from the payload measured at an altitude of 32.7 km. The vertical (**A**), azimuthal (**B**), and radial (**C**) components of the magnetic field in stroke-centered cylindrical coordinates. The dashed vertical line is the retarded time at the payload of the +CG stroke.

with ELF/VLF data shown in Figures 3.17, 3.18, 3.19, and 3.20. Although, in those figures the CG delayed pulses are difficult to resolve due to the axis scaling used to capture the complete CG transient. In Figure 3.21 the vertical electric field data for each of these +CG strokes is shown with the electric field axis adjusted to resolve the delayed pulses. For the 111 kA +CG stroke (panel 3.21 (**A**)), the delayed pulse can be seen with an amplitude of about 80 mV/m at 909-910 ms which is about 5.5 ms after the retarded time of the lightning sferic. A pulse of about 95 mV/m at 837-839 ms or about 5 ms after the lightning sferic can be seen in panel 3.21 (**B**) for the 101 kA +CG. These pulses have similar delay times and magnitudes compared to those measured during the Sprites99 Campaign [Bering et al., 2004b; Bhusal et al., 2004], although the Brazil payloads measured the lightning sferics too, not just the CG delayed pulses. Bering et al. [2004b] and Bhusal et al. [2004] attributed these

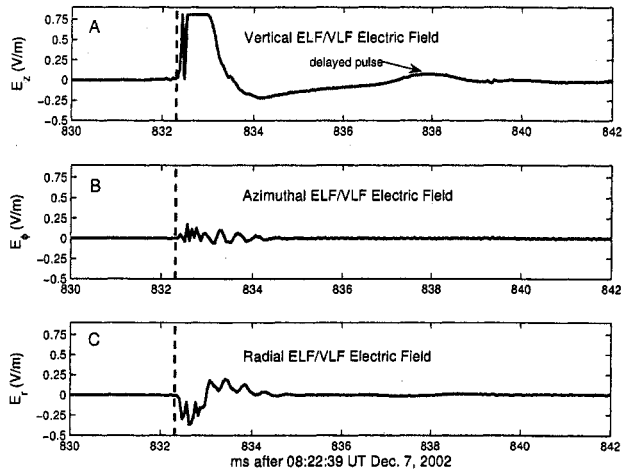

Figure 3.19: The ELF/VLF electric field transient from a 101 kA +CG lightning stroke located 409.9 km horizontal distance from the payload measured at an altitude of 35.1 km. The vertical (**A**), azimuthal (**B**), and radial (**C**) components of the electric field in stroke-centered cylindrical coordinates. The dashed vertical line is the retarded time at the payload of the +CG stroke.

delayed pulses to a mesospheric current moment, which is substantiated with optical data of sprites or halos which occurs simultaneously with a small percentage of these pulses. Cummer et al. [1998] has measured similar CG delayed ELF pulses with ground-based magnetic field sensors that were directly correlated to video images of sprites. Note that the ground-based data of Cummer et al. [1998] always included the lightning sferic first then the CG delayed pulse, like the measurements from the Brazil Campaign.

Electric and magnetic field data from Flight 1 of 934 CG strokes that occurred between 02:47:00 and 10:30:00 Dec. 7, 2002 at distance of 150-600 km were examined for evidence of CG delayed pulses that occurred 4-12 ms after the arrival of the lightning stroke-driven sferic. Data obtained before 02:47:00, during a period nearby storm activity, were excluded to eliminate field perturbations due to nearby

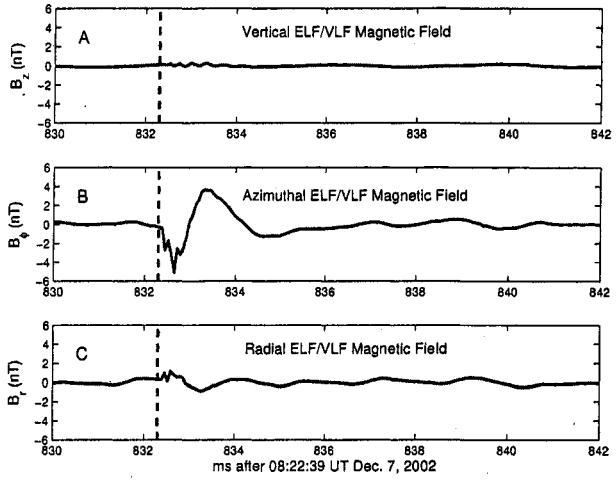

Figure 3.20: The ELF/VLF magnetic field transient from a 101 kA +CG lightning stroke located 409.9 km horizontal distance from the payload measured at an altitude of 35.1 km. The vertical (**A**), azimuthal (**B**), and radial (**C**) components of the magnetic field in stroke-centered cylindrical coordinates. The dashed vertical line is the retarded time at the payload of the +CG stroke.

cloud discharges that might produce false CG delayed pulses. An automated routine identified 240 lightning events (of the 934 studied) for which the vertical electric field was greater than two standard deviations above the background value during the 4-12 ms time window after the retarded time of the lightning sferic. The electric field measurements for these 240 strokes were then examined individually. Only pulses that had frequencies less than 1 kHz and had an unipolarity consistent with mesospheric current flow (positive for +CG strokes, negative for -CG strokes) were considered. It was determined that only 0.5% (4/750) of the -CG strokes and 4.9% (9/184) of the +CG strokes were followed by CG delayed pulses that fit these criteria. These CG delayed pulses were only evident in the vertical electric field data. If these pulses were due to vertical current flowing in the mesosphere an azimuthal magnetic field component should also be measured at the payload. But since these pulses are

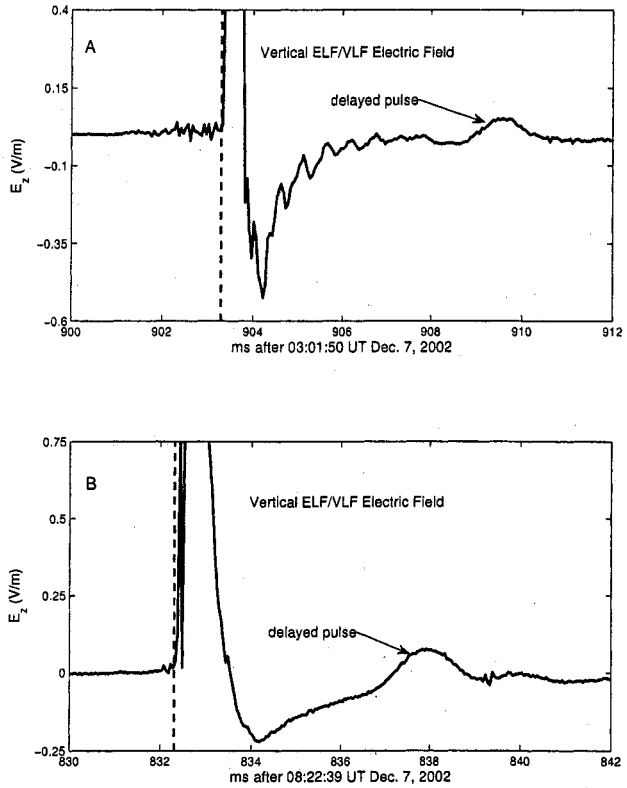

Figure 3.21: The ELF/VLF vertical electric field with the different axis scaling for the 111 kA **(A)** and 101 kA **(B)** +CG strokes shown in Figures 3.17 and 3.19. The delayed pulse can be seen in panel **(A)** at about 909-910 ms and in panel **(B)** at 837-939 ms. The dashed vertical lines are the retarded times at the payload of each +CG stroke.

small in amplitude (less than 100 mV/m) the azimuthal magnetic field component (less than 0.33 nT assuming $B = E/c$) likely was not resolved above the background noise of the search coils. The higher percentage of CG delayed pulses associated with +CG strokes compared to -CG strokes suggests that these pulses could be due to the mesospheric current caused when the quasi-static electric field (QSF) produced by large charge moment CG strokes, which are usually +CGs [Cummer and Lyons,

2004, 2005], surpasses electric breakdown. Thus, the Brazil Campaign results are an agreement with the QSF model (see Chpt. 5 and Pasko et al. [1997a]) that proposes that current flow in the middle atmosphere is the result of large QSF from large charge moment lightning strokes. However, these results are in disagreement with the Sprites99 campaign that measured these CG delayed pulses correlated with 90% of NLDN CG strokes regardless of polarity [Bering et al., 2004b; Bhusal et al., 2004]. Thus, the Sprites99 results suggest that mesospheric current flow is a fundamental response to almost all CG lightning, not just large charge moment events. Moreover, it is not clear from the Brazil data if these CG delayed pulses were indeed the result of mesospheric current. Although each individual waveform was carefully examined, it is possible that some (or all) these pulses were part of the "slow tail" of the lightning generated ELF sferic or driven by cloud discharges that followed the CG strokes. A more detailed discussion of these delayed pulses measured during the Brazil Campaign and comparisons with the pulses measured during the Sprites99 Campaign can be found in Chpt. 6.2.

3.5 Summary of Lightning-Driven Electric and Magnetic Field Measurements

The quasi-electrostatic fields driven by 200 nearby CG flashes were measured during Flight 1, including the largest published electric field change (> 140 V/m) above 30 km in altitude. The two largest electric field changes were driven by +CG flashes, and 26 of the 38 field changes greater than 10 V/m were negative electric field changes not correlated with any BIN detected CG flashes. This suggests that either small positive strokes ($< +10$ kA) or cloud discharges were responsible for these 26 events. The nearby data also suggests that +CG lightning on average produce larger nearby electric field changes compared to -CG lightning (31 V/m compared to 8.7 V/m), which agrees with the correlation between large +CG strokes and sprites. Although, these

statistics have not been normalized for the different horizontal distances and peak currents of the CG strokes. The +CG strokes have larger horizontal current components, suggested by relatively large vertical and radial magnetic field measurements, compared to -CG strokes. The +CG strokes also have more associated cloud lightning activity than -CG strokes, as shown by the optical power measurements. This agrees with previous measurements of large, horizontally extensive current channels that can tap vast amounts of positive charge during a +CG stroke [Williams, 1998]. ELF to VLF field changes for every distant CG lightning stroke (2467 CGs) were measured. CG delayed pulses were measured for only 1.4% of the 934 CG strokes examined, which directly disagrees with the Sprites99 results. Moreover, the Brazil measurements of delayed pulses were dominated by +CG compared to -CG strokes (4.9% of +CGs compared to 0.5% of -CGs).

Chapter 4

CONDUCTIVITY MEASUREMENTS DURING THE BRAZIL SPRITE BALLOON CAMPAIGN

4.1 Atmospheric Conductivity and Sprite Production

The atmospheric conductivity profile and how that ambient profile changes in response to thunderstorm and lightning electric and magnetic fields is critical for the initiation and growth of sprites and other TLEs. For quasi-electrostatic fields, the conductivity governs how space charges in the atmosphere move in response to thunderstorm-driven charge distribution changes in the cloud. This time dependent redistribution of charge determines the magnitude and relaxation time of lightning-driven electric fields at sprite altitudes, for a given lightning charge moment and cloud charge distribution (see Chpt. 5).

The conductivity below about 60 km is dominated by ions (see equation (2.2)) and above 60 km by electrons [Volland, 1984]. Both the ion and electron conductivity are dependent on latitude, longitude, season, solar activity, and solar zenith angle, with the electron conductivity above about 60 km highly dependent on this zenith angle due to the D region ionosphere that forms during the day. The electron conductivity is also dependent on the thunderstorm electric fields that cause electron heating and attachment, which decrease the conductivity, and if the fields are large enough, ionization that increases the conductivity. The effect of electric fields on electron conductivity is further discussed in Chpt. 5.2. Although the affect of electric and magnetic fields on the ion conductivity is assumed to be small due to the large mass of the ions, previous studies [Benbrook et al., 1974; Bering et al., 1980; Holz-

worth et al., 1986; Pinto et al., 1988; Hu et al., 1989; Hu, 1994; Saba et al., 1999] have suggested that the ion conductivity above thunderstorms is perturbed. Possible causes for these variations in ion conductivity are discussed in section 4.3.

4.2 Flight 1 Conductivity Measurements

The conductivity was measured on Flight 1 using the relaxation technique as described in section 2.3. The low voltage vertical probes were momentarily biased with ± 2.5 V, and allowed to refloat as shown in Figure 2.6. The decay time to ambient field levels gives a nearly direct measure of the conductivity [Holzworth et al., 1986]. Note that due to ground station noise, no decay curves from Flight 2 could be adequately fit to provide for a conductivity measurement. Each decay curve was individually inspected to be sure it is not perturbed by a simultaneous lightning stroke. The new high voltage probes were not biased and were not used for making conductivity measurements. Therefore conductivity measurements are only available when the low voltage probes were not saturated, that is, after 00:10:00 UT. Figure 5.1, upper panel, shows a sampling of one conductivity point every 10 minutes (both polarities) altitude normalized to 34 km by the exponential scale heights of $h_+ = 5.8$ km and $h_- = 5.2$ km (the scale heights determined by Saba et al. [1999] over this region of Brazil) for 8 hours during Dec. 7, 2002. Each point is derived from the high time resolution telemetry data, which includes hundreds of data points in each decay profile, resulting in excellent exponential fits to determine the decay time constants. The error in this fitting process results in error bars which are about the size of the point symbols, where we see that the polar components of conductivity (+ for positive and • for negative) have average values of about $3.0 \times 10^{-12}(\Omega\text{m})^{-1}$, while the total conductivity on average is twice this value (squares).

In Figure 4.1, middle and lower panels, the CG lightning stroke rate is shown for the same eight hour period as the conductivity measurements. The middle and

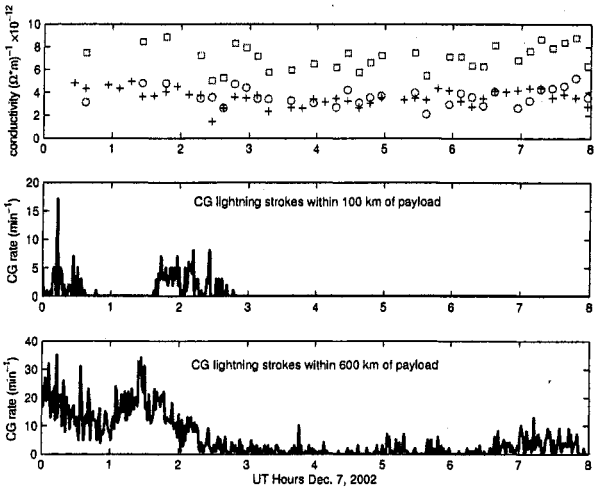

Figure 4.1: *top panel*: Polar components of conductivity (+ for positive and • for negative) and total conductivity (squares) altitude normalized to 34 km for Flight 1. *middle and lower panels*: CG lightning stroke rate within 100 km and 600 km of the balloon payload, respectively

lower panels are for CG strokes within 100 km and 600 km horizontal distance of the payload, respectively, as determined by BIN. A decrease in both polar components of the conductivity occurred around UT 02:30:00, which coincided with a high CG rate within 100 km of the payload. The average total conductivity for the eight hour period was about $6.0 \times 10^{-12}(\Omega\text{m})^{-1}$, which is more than a factor of 2 lower than previous conductivity measurements in this region of Brazil [Saba et al., 1999], after scaling Saba et al. [1999] to our balloon altitude of 32-35 km. During virtually this entire eight hour period, CG strokes were occurring within 600 km, which may suggest that thunderstorm activity lowered the conductivity for this period. But it is important to note that the previous Brazil balloon measurements [Saba et al., 1999] occurred during the daytime in January of 1994. Hence, many factors other than thunderstorm activity (eg. solar activity, biomass burning, etc.) could have contributed to the differences in conductivity measured during the two flights.

4.3 *Possible Mechanisms for Conductivity Variations Over Thunderstorms*

Hu et al. [1989] outlined three possible mechanisms for thunderstorm generated conductivity variations in the stratosphere: thunderstorm-driven gravity waves, lightning-induced electron precipitation (LEP), and vertical discharges to the stratosphere.

Gravity waves can be driven by large thunderstorms that overshoot into the lower stratosphere due to intense updrafts and then are forced back down due to the increase in temperature with altitude in the stratosphere. The thunderstorm oscillates up and down with a period on the order of minutes driving gravity waves that generate neutral density variations in the middle atmosphere [Pasko et al., 1997b]. Since the atmospheric conductivity is inversely proportional to the neutral density (see equation (2.2) in Chpt. 2 and equations (5.14) and (5.15) in Chpt. 5), these gravity wave driven density fluctuations cause variations (increases and decreases) in the both the electron and ion conductivities. Another related mechanism not mentioned by Hu et al. [1989] involves turbulence in the stratosphere generated by thunderstorms to "shake free" some of the water molecules attached to the ions therefore reducing the mass of the charge carrier (see equation (2.2)) and increasing the conductivity. However, during Flight 1, the conductivity decreased due to thunderstorm activity which contradicts this mechanism.

Lightning generated whistler waves that interact with radiation belt electrons causing them to precipitate into the Earth's atmosphere is known as lightning-induced electron precipitation (LEP) (see Voss et al. [1998]). LEP produces secondary x-rays, through bremsstrahlung, in the stratosphere that can cause increased ionization, and therefore increased atmospheric conductivity. During Flight 1, a conductivity decrease was measured and only one x-ray event was measured at the balloon not correlated with lightning activity (see Figure 2.7), thus contradicting this LEP mechanism.

Vertical discharges to the stratosphere, such as the jets described in section 1.2,

would ionize some of the neutrals causing an increase in the ion and electron densities and thus increasing the conductivity. Unfortunately, due to the heavy cloud coverage blocking the sprite imaging cameras, the presence of jets during the balloon flights is not known. But the decrease in conductivity measured again contradicts the effect that jets would have of increasing the conductivity.

4.4 Extrapolating Flight 1 Conductivity Measurements to Sprite Altitudes

The conductivity measured by Flight 1 can be extrapolated to higher altitudes were sprites are typically observed by using the only published conductivity profile from the stratosphere all the way to the ionosphere over a thunderstorm [Holzworth et al., 1985], which has an exponential scale height of 11 km between 40 and 60 km altitudes over a thunderstorm. The conductivity at the balloon from Figure 4.1 is about a factor of two smaller than the conductivity at the same altitude in the profile of the earlier work [Holzworth et al., 1985]. Using the conductivity profile from this rocket and balloon data [Holzworth et al., 1985], but shifted to lower values so the profile matches the lower conductivity over this Brazilian storm (keeping the scale height of 11 km), results in a polar conductivity at 60 km of about $5 \times 10^{-11}(\Omega\mathrm{m})^{-1}$ or a polar time constant of 177 ms as shown in Figure 4.2. If the local relaxation time constant at sprite initiating altitudes is 100 to 200 ms, then the two lightning transients identified in Figures 3.4 and 3.5 will add, making a total field larger than either single event. Since these two lightning-driven electric field changes occurred about 140 ms apart, the effect of the first stroke in the mesosphere will have decayed away substantially when the second stroke occurs. But the electric field changes due to the two strokes will partially add together, allowing for a greater field change than either stroke individually would provide. Note that this adding effect of the electric field driven by these two strokes is shown in Chpt. 5 when a numerical model using

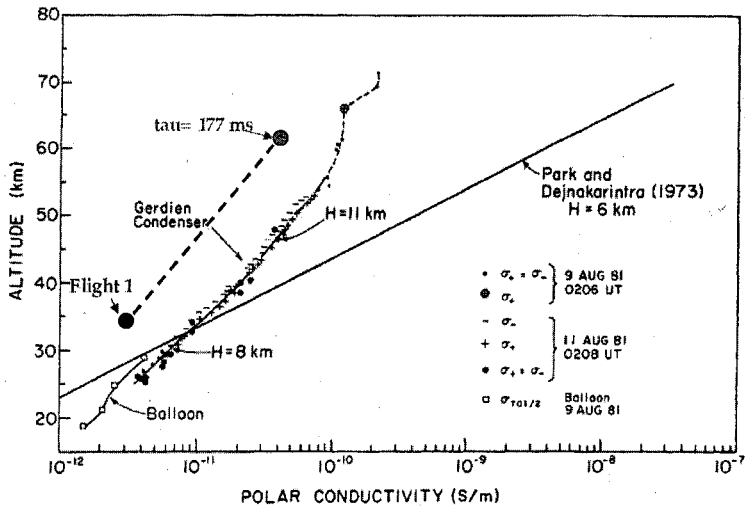

Figure 4.2: Theoretical [Park and Dejnakarintra, 1973] and experimental [Holzworth et al., 1985] single polarity conductivity profiles with altitude (adapted from Holzworth et al. [1985]). The average single polarity conductivity (average of positive and negative conductivity) for Sprite Flight 1 is shown by the • at 34 km in altitude. Using the experimental profile from [Holzworth et al., 1985] to extrapolate in altitude, the ambient time constant at 60 km is estimated to be $\tau = 177$ ms.

the best fit parameters to the stratospheric measurements is used to predict the fields at 50-80 km in altitude. Hence, the relaxation time of electric fields at 60 km could last for more than 100 ms, which is long enough to give sprites plenty of time to develop.

Chapter 5

MEASURED QUASI-ELECTROSTATIC FIELDS AND A NUMERICAL MODEL

5.1 Overview

In the case study presented, the largest electric field change ever measured above 30 km (> 140 V/m, correlated with two positive cloud-to-ground (+CG) strokes shown in Figures 3.4 and 3.5) is compared to an axi-symmetric quasi-electrostatic field (QSF) model. Both the amplitude and the relaxation time of this lightning-driven electric field change is compared to this QSF model at the exact location of the in situ balloon measurements. The lightning stroke locations and peak current values for this +CG event are provided by the BIN (see Chpt. 2), and the conductivity is measured in situ aboard the balloon payload (see Chpt. 4). By varying the QSF model input parameters (e.g. charge moment, discharge time, cloud charge distribution, atmospheric conductivity profile), the model is compared to the in situ measurements. Using the best fit parameters of this comparison, the amplitude and relaxation time of the electric field change everywhere in the stratosphere and mesosphere is predicted and compared to various electrical breakdown thresholds needed for the initiation and/or growth of sprites.

5.2 Model Formulation

The numerical QSF model developed for this study uses an axi-symmetric cylindrical coordinate system centered about the lightning stroke (see Figure 5.1) and is based on the model of Pasko et al. [1997a]. The model uses a one km resolution 2-d grid, with al-

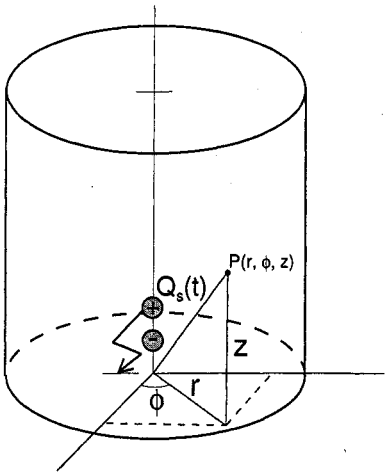

Figure 5.1: The axi-symmetric cylindrical stroke-centered coordinate system used in the QSF model (reproduced from Pasko et al. [1997a]).

titude Z = 0-90 km and radial distance R = 0-60 km, to simulate the lightning-driven electric field pulse in the 3-d space encompassed by this 90 km $\times$ 120 km cylinder. This model assumes that the CG stroke removes charge from the cloud without any orientation (vertical or horizontal) of the lightning current identified, with the coordinate system origin ($R = 0$, $Z = 0$) at the location of the detected ground stroke. The cloud charge ρ_c (specified in equation (5.2)) is not conserved since thunderstorms generate charge, such as through the graupel/ice mechanism discussed in Chpt. 1.1. The charge elsewhere in the atmosphere ρ_b evolves in time due to the insertion (simulated charging process) and removal (simulated lightning stroke) of charge in the thundercloud and the nonzero atmospheric conductivity σ. Moreover, only the electric field change due to lightning events is realistically modeled, not the background electric field before and after the lightning events, which involves complicated cloud charging/discharging mechanisms which is beyond the simple thundercloud specified in this model (see Chpt. 1.1).

The cloud is charged with a characteristic charging time t_c (0.5 s for the case study in section 5.3) for both the positive and negative charge layers with total charge of $\pm Q_0$ through

$$\pm Q(t) = \pm Q_0 \frac{\tanh(t/t_c)}{\tanh(1)}, \text{ for } 0 < t \leq t_c \tag{5.1}$$

to a charge density of

$$\rho_c = \rho_+ + \rho_- \tag{5.2}$$

where

$$\rho_\pm = \pm \rho_0 e^{-[(z-z_\pm)^2/a^2 + r^2/b^2]} \tag{5.3}$$

are Gaussian distributions of positive and negative charge layers (centered at $Z = z_\pm$ and $R = 0$ with Z and R variances of $a/\sqrt{2}$ and $b/\sqrt{2}$) normalized to $\pm Q_0$ by

$$\pm \rho_0 = \frac{\pm Q_0}{\int e^{-[(z-z_\pm)^2/a^2 + r^2/b^2]}\, dV}. \tag{5.4}$$

Charge is removed from the positive layer (for a +CG) or negative layer (for a -CG) with time t_d through

$$\pm Q(t) = \pm Q_0 [1 - \frac{\tanh((t-t_c)/t_d)}{\tanh(1)}], \text{ for } t_c < t \leq (t_c + t_d) \tag{5.5}$$

to simulate the removal of charge due to the lightning stroke. The tanh function employed in (5.1) and (5.5) is used in order for direct comparison with the QSF model of Pasko et al. [1997a] and is not physically significant.

At each time step the background charge density ρ_b (initialized as $\rho_b = 0$) and the cloud charge density ρ_c are used to solve for the electric potential ϕ (initialized as $\phi = 0$) using the Poisson equation

$$-\nabla^2 \phi = \frac{(\rho_b + \rho_c)}{\epsilon_0} \tag{5.6}$$

where ϵ_0 is the permittivity of free space and $Z = 0, 90$ km and $R = 60$ km are assumed to be perfect conductors (ϕ = constant at boundaries). Equation (5.6) is solved using a library of FORTRAN subroutines for the solution of separable elliptic partial differential equations in cylindrical coordinate systems, which employ the method of cyclic reduction, published by Swarztrauber and Sweet [1979] . The potential for some well studied charge distributions (eg. monopole and dipole) were calculated to verify that these subroutines were working properly. From the potential ϕ the electrostatic field $\vec{E}$ is determined using $\vec{E} = -\nabla\phi$ (calculated using the centered finite difference method) and combined with (5.6) gives

$$\nabla \cdot \vec{E} = \frac{(\rho_b + \rho_c)}{\epsilon_0} \tag{5.7}$$

which is Gauss's Law. The continuity equation for charge which governs how the charge redistributes after the lightning stroke is

$$\frac{\partial \rho_b}{\partial t} + \nabla \cdot \vec{J_b} = 0 \tag{5.8}$$

where $\vec{J_b}$ is the background current density. Ohm's Law for the conduction current density is

$$\vec{J_b} = \sigma \vec{E} \tag{5.9}$$

where σ is the altitude dependent atmospheric conductivity (the sum of the ion and electron contributions to the conductivity discussed later in this section). Using (5.7), (5.8), and (5.9) a modified continuity equation can be derived

$$\frac{\partial \rho_b}{\partial t} + \nabla\sigma \cdot \vec{E} + \frac{(\rho_b + \rho_c)\sigma}{\epsilon_0} = 0 \tag{5.10}$$

which determines how the background charge density ρ_b is evolved in time due to atmospheric conductivity σ and the electric field $\vec{E}$. For regions outside the cloud,

the cloud charge is zero ($\rho_c = 0$) so (5.10) becomes

$$\frac{\partial \rho_b}{\partial t} + \nabla\sigma \cdot \vec{E} + \frac{\rho_b \sigma}{\epsilon_0} = 0. \tag{5.11}$$

For regions inside the cloud, the cloud charge is much greater than the background charge ($\rho_c >> \rho_b$). Moreover, the conductivity gradient, which exponentially increases with altitude (scale height of 8 km, as discussed later in this section), is small at the cloud altitudes so that the second term in (5.10) is negligible compared to the third term in (5.10) ($(\nabla\sigma \cdot \vec{E}) << (\rho_c\sigma/\epsilon_0)$) inside the cloud. Thus, (5.10) reduces to

$$\frac{\partial \rho_b}{\partial t} + \frac{\rho_c \sigma}{\epsilon_0} = 0. \tag{5.12}$$

for regions inside the cloud. However, a cloud charge source term must be added to the r.h.s of (5.12) to prevent the cloud charge density from being changed by the conduction current, and thus allow for the cloud charge to evolve independently from the background charge. This source term is chosen to be identical to the second term in (5.12) ($(\rho_c\sigma)/\epsilon_0$) so that (5.12) reduces to $\partial\rho_b/\partial t = 0$ to prevent the background charge density from decreasing the net charge in the cloud. Since this QSF model requires that the net cloud charge be exactly equal to cloud charge ρ_c that is specified by (5.2), this term is included. Hence, by adding this term, (5.11) can be used to determine how the background charge density ρ_b is evolved in time due to atmospheric conductivity σ and the electric field $\vec{E}$ inside and outside the cloud. Note that (5.11) is solved numerically using the 4th order Runge-Kutta method for partial differential equations. Instead of adding $(\rho_c\sigma)/\epsilon_0$ to the r.h.s (5.12), a more physically realistic method would be to lower the conductivity inside the cloud by about an order of magnitude from regions outside the cloud (see MacGorman and Rust [1998, Chpt. 7.6] for a discussion of conductivity measurements inside thunderclouds). Since the conductivity inside the cloud would be very small, (5.12) would again reduce to $\partial\rho_b/\partial t = 0$

and the background charge density would not decrease the net charge in the cloud. This lowered conductivity inside the cloud would also cause a screening layer, which has been measured aloft [MacGorman and Rust, 1998, Chpt. 3.5.4], to form at the cloud boundary due to the large conductivity gradient. Future versions of this QSF model will include this lowered cloud conductivity instead of the added term $(\rho_c\sigma)/\epsilon_0$ in (5.12).

The atmospheric conductivity below 60 km in altitude is dominated by ions [Volland, 1984, Chpt. 2] and increases exponentially

$$\sigma_i = \sigma_{i0}e^{z/h} \tag{5.13}$$

with altitude z and scale heights of $h = 8$ and 11.1 km (below and above 40 km respectively) as measured by balloon- and rocket-borne instruments in the middle atmosphere [Holzworth et al., 1985]. This ion conductivity profile is confined to fit the in situ data measured during Sprite Flight 1 to solve for σ_{i0}. Above 60 km the electron conductivity dominates, and is determined by

$$\sigma_e = eN_e\mu_e \tag{5.14}$$

where e is the electron charge, N_e is the electron density, and μ_e is the electron mobility. The electron density profile increases exponentially with a scale height of 3 km with $N_e(60\text{ km}) = 5 \times 10^3$ m^{-3}, which is similar to the electron density profile model employed by Pasko and Inan [1994, Figure 4, Profile 1]. The ambient atmospheric conductivity profile and the corresponding relaxation time profile used in the case study of section 5.3 are shown in Figure 5.2. The electron mobility is dependent on the neutral atmospheric density N (given by MSIS-E-90 model for the exact location and time of measurements) and the electric field due to the lightning discharge E, and it is solved for self-consistently using an empirical fit [Pasko et al.,

1997a] to experimental data [Davies, 1983; Hegerberg and Reid, 1980] through the form

$$\mu_e = 1.36 N_0/N, \text{ for } EN_0/N < 1.62 \times 10^3 \text{ V/m} \tag{5.15}$$

$$\mu_e = 10^{\sum_{i=0}^{2} a_i x^i}/N, \text{ for } EN_0/N \geq 1.62 \times 10^3 \text{ V/m}$$

where $x = \log(E/N)$, $a_0 = 50.970$, $a_1 = 3.0260$, $a_2 = 8.4733 \times 10^{-2}$, and $N_0 = 2.4901 \times 10^{25}$ m^{-3} is the neutral density at sea level. Figure 5.3 shows the dependence of the electron mobility μ_e on the electric field at three different altitudes (60, 70, 80 km). Hence, (5.15) and Figure 5.2 show that when the effective electric field (EN_0/N) is greater than 1.62×10^3 V/m, the electrons are heated by the electric field thus lowering the electron mobility. When the effective electric field is below this heating threshold, the electron conductivity employed in this study agrees relatively well with rocket measurements of the mesospheric electron conductivity [Hale et al., 1981]. There are also effective electric field thresholds that if surpassed would cause ionization and attachment processes that would change the electron density [Pasko et al., 1997a]. However, for the lightning event in this study, these thresholds are never reached. This model was tested by verifying the output ($\rho_b + \rho_c$ and $\vec{E}$) through direct comparison with a similar QSF model [Pasko et al., 1997a] using identical input parameters. The output of the two models agreed to within a few percent.

5.3 Case Study

This case study compares the QSF model to a +CG event that was measured by the Sprite Flight 1 HV electric field sensor (see Chpt. 2) at an altitude of 34 km. This +CG event is comprised of two +CG strokes that occurred at $\sim$ 00:00:09 UT Dec. 7, 2002 $\sim$ 140 ms apart at a horizontal distance of $\sim$ 34 km from the balloon payload (see Chpt. 3.2 and Figures 3.4 and 3.5). These +CG strokes had estimated peak currents of +15 kA and +53 kA, as determined by BIN, with a total combined charge

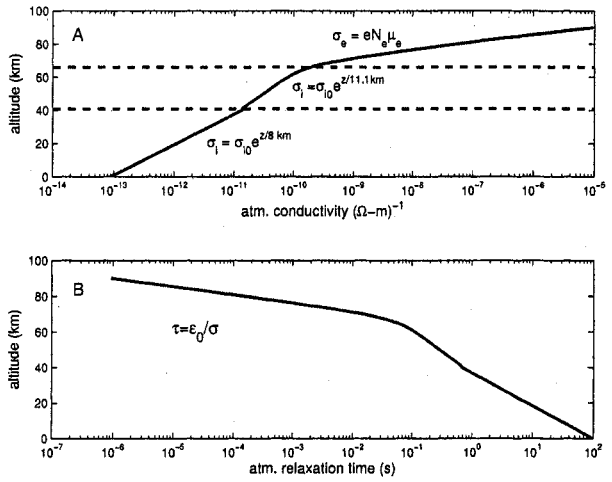

Figure 5.2: The ambient atmospheric conductivity **(A)** and relaxation time **(B)** profiles employed in the QSF model for this case study.

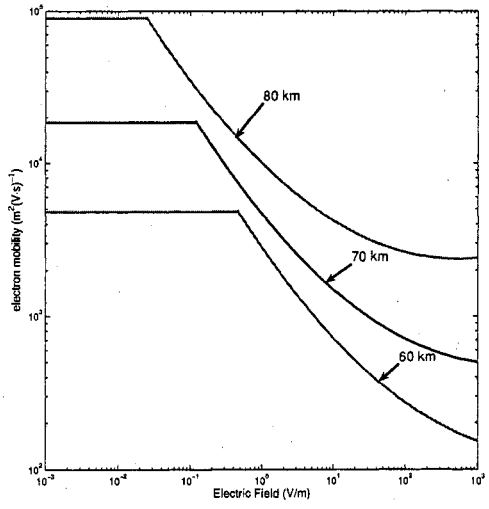

Figure 5.3: The dependence of the electron mobility μ_e on the electric field for at three different altitudes (60, 70, 80 km).

moment of 329-1683 C-km estimated (using both the fitting and impulse methods) from remote ELF measurements (shown in Figure 2.8) in Antarctica and Japan [Sato et al., 2003a].

Figure 5.4 shows contour plots (log scale) for the absolute value of the total charge density $\rho_b + \rho_c$ (left panels) and the magnitude of the vertical electric field E_z (right panels) at three instants in time (1 ms before the first +CG stroke, 1 ms after the second +CG stroke, and 350 ms after the second +CG stroke) given by the QSF model for this case study. At 1 ms before the first +CG stroke, the cloud (below $Z = 10$ km) is charged with positive $+Q_0$ over negative charge $-Q_0$ (shown as white + and − signs) which has induced negative charge (black − signs) to form above the cloud giving an upward directed vertical electric field. At 1 ms after the second +CG stroke, all of the positive charge has been removed from the cloud by the two +CG strokes. This charge removal induces positive charge to form at $Z = 60 - 80$ km with negative pre-stroke charge remaining below $Z = 60$ km due to the longer relaxation times with decreasing altitude (see Figure 5.2). This positive over negative charge structure in the middle atmosphere causes the vertical electric field to point downwards 1 ms after the second +CG stroke with a much greater magnitude than the upwards directed field that existed before the first +CG stroke. At 350 ms after the second +CG stroke, the positive charge has neutralized the negative charge in the middle atmosphere with the negative charge in the cloud remaining. The vertical electric field still points downward at 350 ms after the second +CG stroke, but now has relaxed to a much smaller magnitude compared to just after the second stroke. These contour plots of the charge density and the vertical electric field summarize how CG strokes form electrostatic fields in the middle atmosphere that evolve in time due to the non-zero atmospheric conductivity.

Figure 5.5 shows the comparison between the model output at $R = 34$ km and $Z = 34$ km and in situ data for this +CG event, composed of two +CG strokes at 0.50 s and 0.64 s, for both the vertical (*upper panel*) and radial (*lower panel*) electric

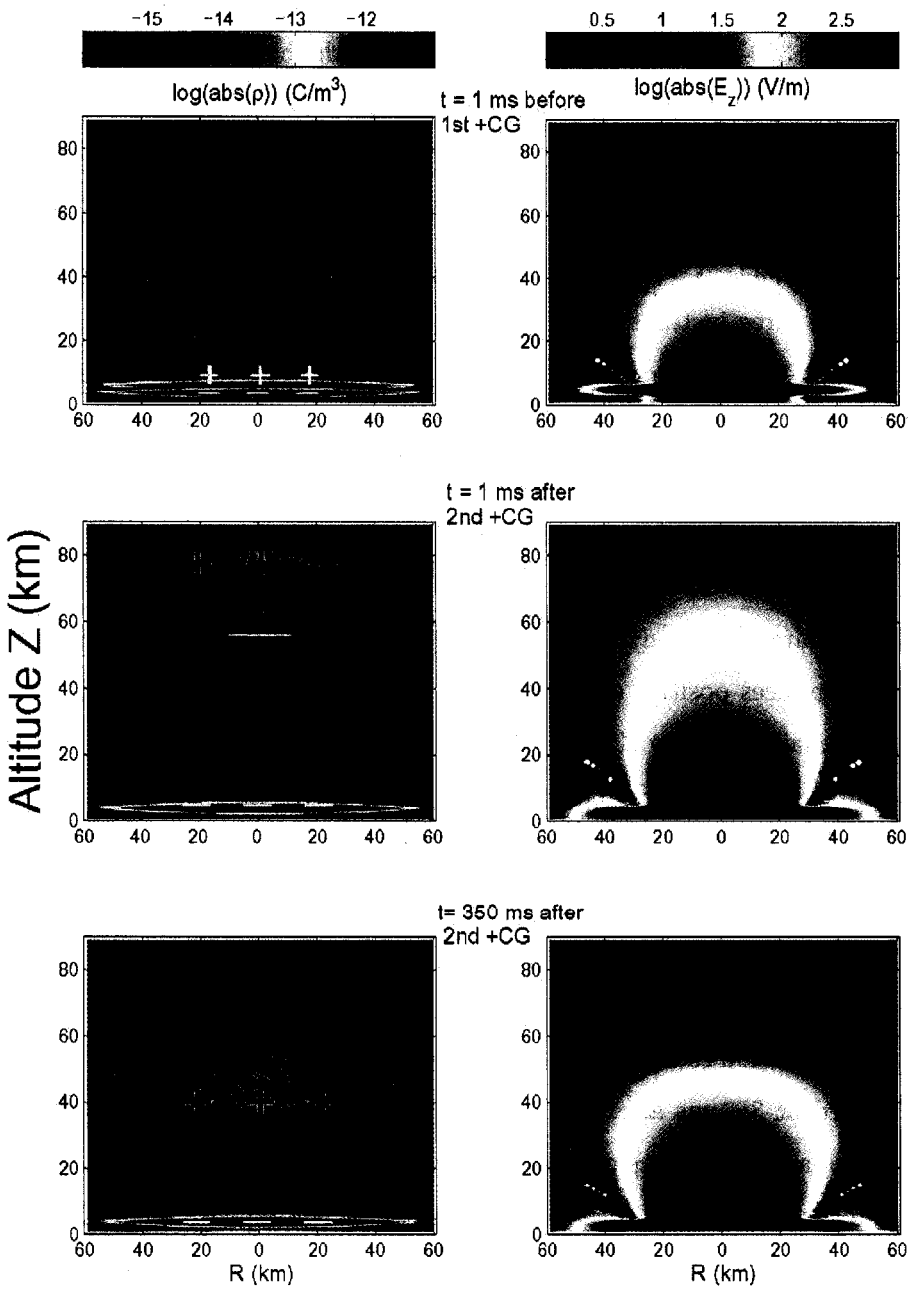

Figure 5.4: Contour plots (log scale) for the absolute value of the total charge density $\rho_b + \rho_c$ (left panels) and the magnitude of the vertical electric field E_z (right panels) at three instants in time (1 ms before the first +CG stroke, 1 ms after the second +CG stroke, and 350 ms after the second +CG stroke) given by the QSF model.

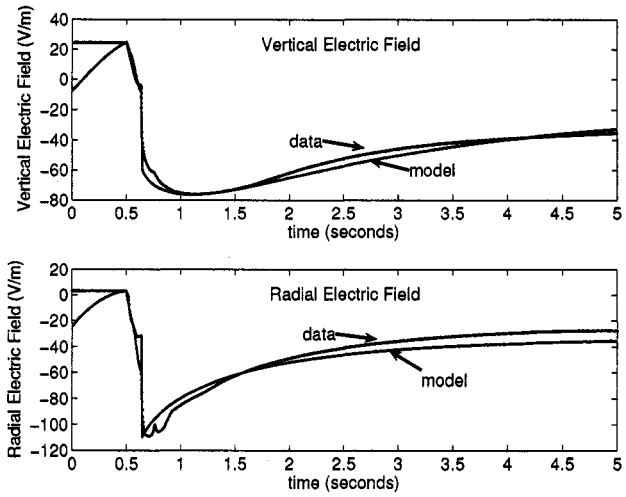

Figure 5.5: Comparison between model (red line) at $R = 34$ km and $Z = 34$ km and data (blue points) for two +CG strokes at 0.50 s and 0.64 s. *top panel*: vertical electric field. *bottom panel*: radial electric field.

fields. Note that the time interval 0.0-0.5 s is the artificial cloud charging time t_c for the QSF model. In this coordinate system, a negative vertical electric field represents a field vector pointing towards the ground. The dc (< 25 Hz) electric field data are shown in Figure 5.5. The dc and ac (shown in Figure 3.5) electric field data for this event had similar rise times, which confirms that the dc instrument properly measured the initial rise of the field.

The model parameters that best fit the model to the data for this event (comprised of two +CG strokes) within ±10% are: total charge moment of $M_q = 479 \pm 50$ C-km (152 C-km for the first +CG stroke and 327 C-km for the second +CG stroke), discharge times of $t_d = 100$ ms for the first +CG stroke and $t_d = 8$ ms for the second +CG stroke, charge layer diameter of 59 ± 17 km (same for positive and negative layer), charge layer thickness of 1.4 ± 0.5 km (for the positive and negative layers separately), positive charge layer altitude of $z_+ = 6$ km, negative charge layer

altitude of $z_- = 4$ km, and atmospheric conductivity as defined in section 5.2 with ion conductivity constants of $\sigma_{i0} = 9 \times 10^{-14}(\Omega\text{m})^{-1}$ and $3.4 \times 10^{-13}(\Omega\text{m})^{-1}$ (below and above 40 km respectively) to match with the ion conductivity measured by Sprite Flight 1 ($6 \times 10^{-12}(\Omega\text{m})^{-1}$ average total conductivity for the 12 hr flight, see Chpt. 4, Figure 4.1). Note that the first +CG stroke had a best fit discharge time of 100 ms, which suggests that this event included a long continuing current interval after the return stroke similar to the previous ground-based ULF measurements of Cummer and Füllekrug [2001], and the second +CG stroke had a more typical continuing current interval for +CG lightning of 8 ms. The model and data agree well for the rise and initial decay of the electric field change (0.5-1.5 s), thus showing that a QSF approach is effective in modeling lightning driven electric fields. However, since the complex cloud charging/discharging processes not related to the +CG event are not included in this model, the electric field before the first +CG stroke (which occurs at 0.5 s) and well after the two discharges ($\gtrsim 1.5$ s) are less well correlated.

These best fit parameters are now used to predict the lightning-driven electric field perturbation at higher altitudes where sprite initiation and/or growth can occur. Figure 5.6 shows the QSF model output for the vertical electric field driven by two +CG strokes at 500 ms and 640 ms at $R = 0$ km, $Z = 50, 60, 70, 80$ km using these parameters. In Table 5.1, the magnitude (ΔE and E_{max}) and relaxations times (τ) of these vertical electric field perturbations, along with the the conventional breakdown threshold $E_k = \pm 3.2 \times 10^6 N/N_0$ V/m [Raiser, 1991], the negative and positive streamer electrical breakdown thresholds $E_{cr}^- = -1.25 \times 10^6 N/N_0$ V/m [Babaeva and Naidis, 1997], $E_{cr}^+ = 4.4 \times 10^5 N/N_0$ V/m [Allen and Ghaffar, 1995], and the relativistic runaway threshold, $E_t = 2.02 \times \pm 10^5 N/N_0$ V/m [Marshall et al., 1995] are summarized for $R = 0$ km, $Z = 50, 60, 70, 80$ km.

In Figure 5.7, the vertical electric field magnitude vs. altitude is shown at three instants in time (1 ms before the first +CG stroke, 1 ms after the second +CG stroke, and 350 ms after the second +CG stroke) and compared to the various electric

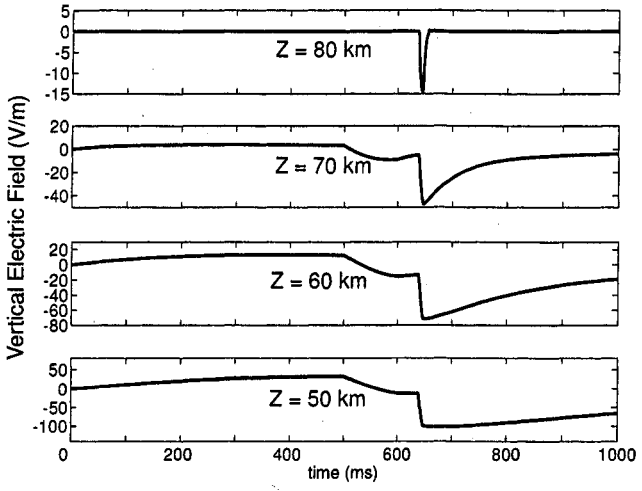

Figure 5.6: Model prediction of the vertical electric field driven by two +CG strokes at 500 ms and 640 ms at four different mesospheric altitudes ($Z = 80, 70, 60$, and 50 km, $R = 0$ km) using the best fit parameters to the measured electric field change at $Z = 34$ km, $R = 34$ km.

breakdown thresholds. The electric field is maximum just after the second +CG stroke (pointing downward) but never surpasses the conventional breakdown threshold E_k. The vertical electric field does surpass the positive streamer breakdown threshold E_{cr}^{+} for $Z = 66 - 82$ km and the relativistic breakdown threshold E_t for $Z = 58 - 83$ km, and the field approaches the negative streamer breakdown threshold E_{cr}^{-} at $Z = 77$ km (to within 94%). Note that due to the 1 km grid spacing employed in the model, the electric field in the cloud (altitude < 8 km) is not well resolved. At 1 ms before the first +CG stroke, the field should be zero at two altitudes in the cloud, at 3-4 km and again at 6-7 km in Figure 5.7. Since this QSF model does not attempt to accurately model in-cloud fields, this lack of resolution has no effect on this analysis.

Table 5.1: The relaxation time (τ), change in vertical electric field (ΔE), and maximum vertical electric field (E_{max}) for the model output shown in Figure 5.6 ($R = 0$ km, $Z = 50, 60, 70, 80$ km), along with the altitude dependent electrical breakdown thresholds (E_k, E_{cr}^-, E_{cr}^+, E_t) .

	50 km	60 km	70 km	80 km
τ (ms)	> 320	239	69	7.6
ΔE (V/m)	-134.5	-84	-51	-14.5
E_{max} (V/m)	-101.5	-71.5	-47.5	-14.5
E_k (V/m)	± 3009	± 907	± 237	± 48
E_{cr}^- (V/m)	-1175	-354	-92	-19
E_{cr}^+ (V/m)	413	125	33	7
E_t (V/m)	± 190	± 57	± 15	± 3

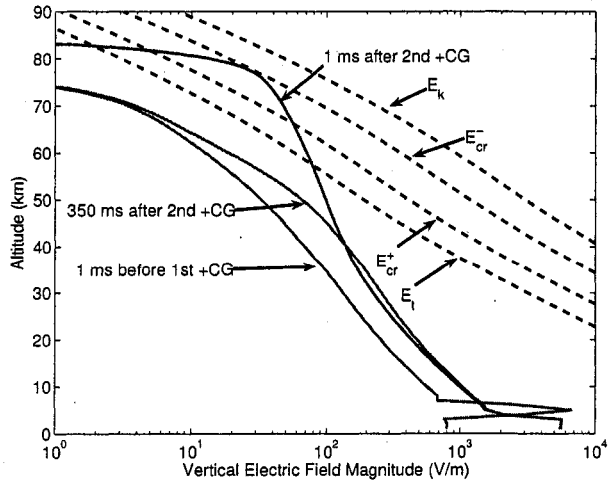

Figure 5.7: Model prediction of the vertical electric field magnitude vs. altitude at $R = 0$ km using the best fit parameters to the measured electric field change at $Z = 34$ km, $R = 34$ km. The vertical electric field magnitude at three instants in time (1 ms before the first +CG stroke, 1 ms after the second +CG stroke, and 350 ms after the second +CG stroke) is compared to the various breakdown thresholds (E_k [*Raizer*, 1991], E_{cr}^- [*Babaeva and Naidis*, 1997], E_{cr}^+ [*Allen and Ghaffar*, 1995], E_t [*Marshall et al.*, 1995]).

5.4 QSF Model and Other Nearby Electric Field Measurements

The QSF model formulated in section 5.2 can be applied to the other nearby electric field changes which are presented in Chpt. 3. All of the electric field changes driven by these nearby lightning exhibit properties consistent with the QSF model, such as initial onsets of a few hundred ms and decay times of a few seconds. The +CG lightning generally drove larger field changes than the -CG lightning (as discussed in Chpt. 3.1.2), which is consistent with larger charge moment M_q events (which are typically +CGs) driving the larger field changes. Due to the lengthy computing time needed to find the best fit parameters to particular events (as in the case study in section 5.3), the results from this case study will be extrapolated to analyze the other large field changes measured at the balloon payload.

The second largest electric field change measured was driven by two +CG strokes at about 00:16:03 UT Dec. 7, 2002 about 50 km from the payload as discussed in Chpt. 3.2 and Figures 3.7 and 3.8. To extrapolate the QSF model from the previous case study (section 5.3), it is assumed that all of the best fit parameters (such as cloud charge distribution, atmospheric conductivity, etc.) except for the total charge removed Q_0 are the same for this event that occurred 16 minutes after the case study event. The further assumption that the amplitude of the field change scales linearly with the charge moment M_q of the driving CG event allows for the total charge removed Q_0 to be estimated using the extrapolation from the case study. Assuming that the field magnitude scales with the charge moment M_q is justified by equation 1.3 term 1, which gives this linear relation for the electrostatic field without including the affects of a non-zero atmospheric conductivity. Including atmospheric conductivity (as in the numerical model of section 5.2) causes the relation between the charge moment and field change to deviate from linear by up to about 10% at the balloon altitude.

Using the extrapolated QSF model results from the case study on this second

largest electric field change, the total charge removed is estimated to be $Q_0 = 189$ C or a charge moment of $M_q = 1135$ C-km (since $z_+ = 6$ km). Thus, assuming that the electric field changes predicted at sprite altitudes in section 5.3 scale linearly with the charge moment, the predicted field changes driven by this event at 00:16:03 UT are a factor of M_q(extrapolated)/M_q(case study) = 1135 C-km/479 C-km = 2.37 larger than for the case study above shown in Figures 5.6 and 5.7 and Table 5.1. Thus the predicted field using this extrapolation at $Z = 70$ km, $R = 0$ km for this +CG event is about -113 V/m and at $Z = 80$ km, $R = 0$ km is about -34 V/m, which are both less than the conventional breakdown threshold (Table 5.1). However, if the effects of the electric field dependent conductivity described in section 5.2 are included, the field changes would be larger due to the decreased electron mobility μ_e decreasing the electron conductivity σ_e. Unfortunately, it is not possible to fully model this +CG at 00:16:03 UT as in the case study since the two +CG strokes for this event occur at different locations, and thus the stroke-centered cylindrical coordinate system cannot be used.

This same extrapolation method, using the same assumptions as above, estimates the total charge removed during the largest electric field change driven by a -CG event (23:26:30 UT Dec. 6, 2002 about 23 km from the payload, see Chpt. 3.2, Figures 3.11 and 3.12) to be $Q_0 = 17.85$ C or a charge moment of $M_q = 71$ C-km. Thus, the field predictions shown in Figures 5.6 and 5.7 and Table 5.1 can be scaled by a factor of M_q(extrapolated)/M_q(case study) = 71 C-km/479 C-km = 0.15 which gives electric fields of 7 V/m at $Z = 70$ km and 2 V/m at $Z = 80$ km for $R = 0$ km. This largest -CG driven field change measured gives much lower field changes at sprite altitudes compared to the two +CG events, which is consistent with large charge moment +CG events driving large quasi-electrostatic fields in the middle atmosphere.

Since BIN does not provide the location of cloud lightning, the QSF model results from the case study above are extrapolated using the upper (50 km) and lower (20 km) bounds of the lightning location (given by CGs located by BIN during the same

storm) relative to the payload for the largest electric field change not correlated with a BIN CG stroke at 23:37:10 UT Dec. 6, 2002 (Chpt. 3.2, Figures 3.14 and 3.15). Using the upper bound of 50 km gives a total charge moment of $M_q = 763$ C-km and using the lower bound of 20 km gives $M_q = 104$ C-km. Since the vertical extent of a cloud discharge is likely to be only a few kilometers, this extrapolation suggests that the total charge destroyed by the cloud discharge could be as large as a few hundred Coulombs, which is much larger than previously reported (see Rakov and Uman [2003, Chpt. 9]). For the upper bound of 50 km, the scale factor for predicted fields of Figures 5.6 and 5.7 and Table 5.1 is M_q(extrapolated)/M_q(case study) = 763 C-km/479 C-km = 1.59, which gives electric fields of -76 V/m at $Z = 70$ km and -23 V/m at $Z = 80$ km for $R = 0$ km. These fields are below the conventional breakdown thresholds (Table 5.1), but could be larger if the electric field dependent electron conductivity is included. For the lower bound of 20 km, the scale factor for predicted fields of Figures 5.6 and 5.7 and Table 5.1 is M_q(extrapolated)/M_q(case study) = 104 C-km/479 C-km = 0.22, which gives electric fields of -10 V/m at $Z = 70$ km and -3 V/m at $Z = 80$ km for $R = 0$ km. This extrapolation suggests that cloud lightning is capable of driving relatively large electric field changes in the middle atmosphere, but without the exact location of this lightning known, the fields at sprites altitudes can only be given upper and lower bounds.

Note that it is assumed for this possible cloud lightning event that there exists significant charge in the cloud that is not destroyed by the cloud discharge in order for the modeled +CG stroke (which leaves negative charge in the cloud) to be extrapolated to this cloud lightning event. This is supported by the observation that the vertical electric field relaxes to about 20 V/m after this cloud discharge (see Figure 3.14), which suggests that a net positive charge remains in the cloud after the discharge. Moreover, this is a reasonable assumption since numerous layers of charge in thunderclouds has been measured with in situ balloon flights [Stolzenburg et al., 1998], and it is unlikely that the cloud discharge would destroy all of the positive and

negative charge in the cloud. However, it is not possible, using the data set available, to know the exact cloud charge structure during this event.

Chapter 6

DISCUSSION AND CONCLUSIONS: IMPLICATIONS FOR SPRITES

6.1 Quasi-Electrostatic Fields Driven by Nearby Lightning

For the first time, lightning-driven electric field changes measured in situ above 30 km have been compared directly to a numerical QSF model. The High Voltage (HV) Electric Field Detector, a new high voltage, high impedance, double Langmuir probe instrument, was designed specifically for measuring these large lightning-driven electric field changes. This is a critical instrument since a large quasi-electrostatic field is included in most sprite generation models. The amplitude and relaxation time of nearby (< 75 km) lightning events measured by the balloon payloads in the stratosphere (see Chpt. 3.2) generally agree with the quasi-electrostatic field model employed in Chpt. 5. Thus, lightning does indeed generate significant electric fields in the middle atmosphere due to the removal and/or redistribution of cloud charge. The in situ data also suggests that +CG lightning on average produce larger nearby electric field changes compared to -CG lightning (31 V/m compared to 8.7 V/m without normalizing for distance and peak current, as discussed in Chpt. 3.1), which agrees with the correlation between large charge moment +CG strokes and sprites. The +CG strokes also have larger horizontal current components, suggested by relatively large vertical and radial magnetic field measurements (see Chpt. 3.2), compared to -CG strokes, Moreover, +CG strokes have more associated cloud lightning activity, as shown by the optical power measurements (see Chpt. 3.2), than -CG strokes. This agrees with previous measurements of large, horizontally extensive current channels

that are capable of tapping vast amounts of positive charge during a +CG stroke [Williams, 1998].

In the case study of Chpt 5.3, the agreement between model and data for the rise and initial decay of the vertical and radial electric field perturbations suggests that the QSF approach is valid for modeling lightning-driven fields. The large diameter (59 km) and thin (1.4 km), low altitude (6 km for the positive layer and 4 km for the negative layer) charge layers agree with previous studies involving large charge moment +CG events that are usually associated with MCC/MCS storms [Marshall et al., 1996; Williams, 1998]. The storm that generated the +CG in this case study had an area of $5000 - 10000$ km^2 (estimated from GOES satellite IR images, see Figure 3.2), which is at the lower limit for MCS storm size. The positive and negative charge layers employed in the QSF model had an area of about 2700 km^2, about $25 - 50\%$ of the total storm area.

Although sprites were not confirmed for the +CG event in this case study, the implications of the predicted electric fields in the mesosphere can be examined. The relaxation time of the mesospheric electric field change is predicted to be at least as long as the duration of a typical sprite event ($\tau = 69$ ms at $Z = 70$ km) allowing sufficient time for sprite initiation and/or growth. Yet, since the electric field after the +CG event never surpasses the conventional breakdown threshold E_k (see Figure 5.7), sprite initiation would not occur for this model prediction. Although the relativistic threshold E_t is surpassed above 58 km in altitude, significant optical emissions would not be initiated by an upward relativistic electron beam since only a few avalanche lengths (e-foldings of the electron population) would be able to develop with this high of a starting altitude [Roussel-Dupre and Gurevich, 1996, Figure 10]. However, if the electric field was to surpass the conventional threshold E_k at a typical sprite initiation altitude of about $Z = 78$ km [Wescott et al., 2001a] due to processes not included in this model, i.e. gravity waves [Pasko et al., 1997b] or micrometeors [Wescott et al., 2001a], then sprites could readily propagate downwards from the initiation altitude,

since the positive streamer threshold E_{cr}^{+} is surpassed for $Z = 66 - 82$ km. Also, since the negative streamer threshold E_{cr}^{-} is nearly surpassed near $Z = 78$ km, propagation upward from the initiation altitude could occur in this region.

The downward direction of the electric field is determined by the positive polarity of the CG event, which allows the positive streamer to propagate downward to about $Z = 66$ km. If instead this was a negative polarity CG event, the field would point upward and the positive streamer would propagate upward to about $Z = 82$ km. Thus, the positive polarity of the CG event would allow for sprites, once initiated, to have a much larger vertical extent ($\sim Z =$ 66-78 km) compared to a sprite caused by a -CG ($\sim Z =$ 78-82 km). This difference in breakdown thresholds for positive and negative streamer production could partially explain why sprites are almost exclusively correlated with positive polarity lightning. Although, for sufficiently large charge moments, both the positive and negative streamer thresholds would be surpassed, and thus the direction of propagation and vertical extent of the sprites would not depend on the polarity of the parent lightning stroke.

The QSF model results for this case study were extrapolated to estimate how another +CG event, a -CG event, and a likely cloud discharge drive electric fields in the middle atmosphere. For the other +CG event at 00:16:03 UT Dec. 7, 2002, the extrapolated model results predicted that the electric field magnitude would be about 70% ($E_z = -34$ V/m) of the field needed for conventional breakdown ($E_k = \pm 48$ V/m) at an altitude of 80 km. Including the effects of electron heating would lower the mobility, and thus the conductivity. This lowered conductivity would increase the relaxation time of the electric field, allowing the field to grow larger, possibly surpassing conventional breakdown. Unfortunately, this +CG event could not be fully modeled, as in the case study of Chpt. 5.3, since the two +CG strokes that make up the event occurred in different locations, which is beyond the capabilities of the stroke-centered model. For the largest -CG stroke-driven electric field change measured, the predicted field change at an altitude of 80 km was only 2 V/m, only about 4% of the conven-

tional breakdown field. Since the location of the likely cloud discharge that produced the largest non-CG correlated electric field change could not be determined by BIN, only upper and lower bounds can be placed on the predicted field change in the middle atmosphere. Assuming that the cloud lightning was 50 km (20 km) from the payload, would give an vertical electric field of -23 V/m (-3 V/m) at an altitude 80 km. Although only a range of -3 to -23 V/m (or $6\% - 46\%$ of E_k) can be predicted, this extrapolation suggests that cloud lightning can drive large quasi-electrostatic fields, in fact larger than any of the measured -CG strokes. If this one cloud discharge studied is representative of at least a few percent of all cloud lightning, then cloud discharges could play a significant role in driving the electric fields responsible for sprites.

Clearly, future in situ electric field measurements of confirmed sprite events, used together with a numerical QSF model, could provide much insight into the physical mechanisms underlying the initiation and growth of sprites.

6.2 ELF to VLF Fields Driven by Distant Lightning

The distant (75-600 km) lightning events drove ELF to VLF electric (25 Hz - 8 kHz) and magnetic (300 Hz - 8 kHz) fields, with large vertical electric field and azimuthal magnetic field components, that are generally consistent with ground-based measurements [Cummer et al., 1998] and models [Pasko et al., 1998b]. However, the results of the Brazil campaign are in disagreement with the results of a previous balloon campaign, Sprites99 [Bering et al., 2002, 2004a,b; Bhusal et al., 2004], conducted over the U. S. High Plains, in which the lightning sferics were rare, while CG delayed pulses (which they attributed to mesospheric current) were frequent. For a few of these CG delayed pulses measured during Sprites99, correlated sprites and halos were imaged as shown in Figure 6.1 (from [Bering et al., 2004b]). Although the Sprites99 payloads had a low pass filter of 1 kHz (below the 8 kHz filter employed on the Brazil payloads), the Brazil payload measurements, along with the ground-based measurements [Cum-

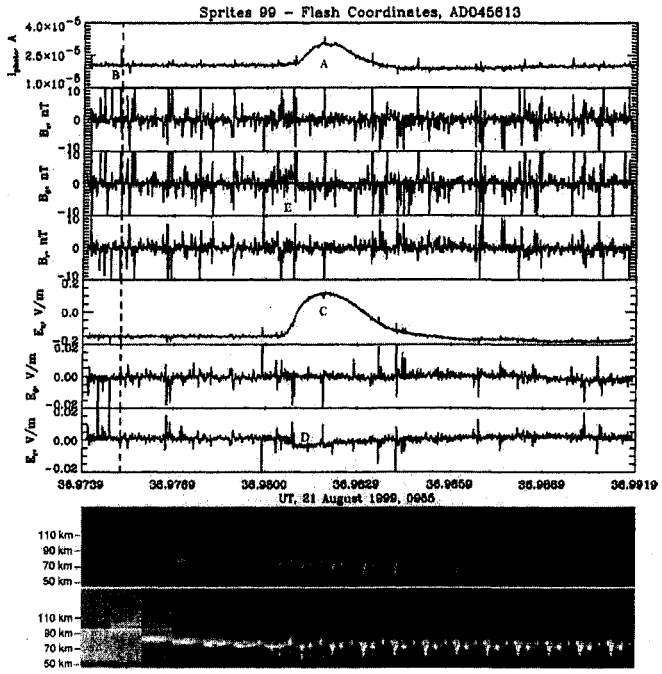

Figure 6.1: Sprites99 balloon measurements of the electric and magnetic fields correlated with with an imaged sprite located about 379 km from the payload (reproduced from Bering et al. [2004b]). There is no lightning sferic at the retarded time of the NLDN recorded +CG, but there is a CG delayed pulse in the vertical electric field correlated with optical sprite emissions.

mer et al., 1998] and models [Pasko et al., 1998b], suggest that the Sprites99 payloads should have measured the few 100 Hz ELF transient of the distant lightning. Bering interpreted these delayed CG pulses correlated with sprites, but without CG sferics, as evidence that sprites might not be the result of lightning driven quasi-electrostatic fields [Williams, Dec. 15, 2001].

The Brazil balloon payloads measured ELF to VLF field changes for every distant lightning stroke (2467 CG strokes) and only measured CG delayed pulses for 1.4% of the 934 CG strokes examined, which directly disagrees with the Sprites99 results.

Moreover, the Brazil measurements of CG delayed pulses were dominated by +CG compared to -CG strokes (4.9% of +CGs compared to 0.5% of -CGs). The Brazil campaign results, in agreement with ground-based measurements [Cummer et al., 1998] and models [Pasko et al., 1998b], support the hypothesis that large quasi-electrostatic fields driven by large charge moment lightning events, which are usually +CG strokes, cause the breakdown and resulting current flow in the mesosphere seen as sprites. Note that the quasi-electrostatic field alone may be causing this breakdown or the QSF along with high energy seed electrons from cosmic rays. The Brazil data cannot differentiate between these mechanisms since no optical emissions in the mesosphere were able to be observed during the flights. Although, the case study of Chpt. 5.3 for a nearby lightning event suggests that the conventional breakdown mechanism might lead to breakdown more readily than the relativistic runaway mechanism, since the relativistic threshold E_t must be surpassed below about 30-35 km in altitude to generate optical emissions [Roussel-Dupre and Gurevich, 1996; Lehtinen et al., 1997].

6.3 Atmospheric Conductivity

Sprite Flight 1 measured a decrease in the atmospheric conductivity that coincided with a high CG rate (determined by BIN) within 100 km of the payload as shown in Figure 4.1. Moreover, the average conductivity for the entire flight (excluding data after sunrise) was about $6.0 \times 10^{-12}(\Omega\mathrm{m})^{-1}$, which is more than a factor of 2 lower than previous conductivity measurements in this region of Brazil [Saba et al., 1999], after scaling Saba et al. [1999] to our balloon altitude of 32-35 km. During virtually this entire eight hour period, CG strokes were occurring within 600 km, which suggests that thunderstorm activity might have lowered the conductivity for this period. Although the mechanism for this conductivity decrease is not understood, these variations of the conductivity above and near thunderstorm may play an important role for sprite generation. The atmospheric conductivity determines the magnitude and

relaxation time of the quasi-electrostatic field for a lightning event with a given charge moment and charge distribution as shown in the QSF model of Chpt. 5. Variations in the conductivity in the middle atmosphere by as little as 10% can cause a sprite to initiate or not initiate.

In Figure 4.2 the average conductivity measured by Flight 1 at 30-35 km is extrapolated to 60 km in altitude using the exponential scale height of $h = 11$ km as measured during a previous balloon and rocket campaign by Holzworth et al. [1985]. The estimated polar relaxation time at 60 km in altitude is 177 ms using this extrapolation, which is about a factor of three longer than the relaxation time measured by Holzworth et al. [1985] at 60 km and about 2 orders of magnitude longer than the conductivity used in the model of Park and Dejnakarintra [1973]. If the local relaxation time constant at sprite initiating altitudes is 100 to 200 ms, then the two lightning transients identified in Figures 3.4 and 3.5 will add, making a total field larger than either single event (just as they add at the balloon altitudes in Figures 3.4 and 3.5). Hence, the relaxation time of electric fields at 60 km could last for more than 100 ms, which is long enough to give sprites plenty of time to develop.

Chapter 7

PROPOSED FUTURE RESEARCH

7.1 Future Experimental Research

The Sprite Brazil Balloon Campaign 2002-2003 showed that a balloon-borne instrument platform was useful for studying how thunderstorms and lightning affect the middle and upper atmosphere. Thus, two future balloon campaigns will try to accomplish the same goal of measuring the electromagnetic environment above a sprite-producing thunderstorm, but with upgrades to increase the probability of success.

Planned for February-March and October-November 2006, the Sprite II Brazil Balloon Campaign will take place in the south of Brazil, with launches occurring from Santa Maria. In this region of Brazil, and neighboring Argentina and Uruguay, large MCS storms, similar to storms in the U. S. High Plains, occur during the late Spring and early Autumn. Thus, this new location in Brazil will significantly increase the probability that the balloon payload will fly above sprite-producing storms. To allow for better telemetry coverage for data sent back from the balloon payload, two ground stations will be used for the data downlink. One ground station will be near the launch site of Santa Maria, and the other will be located west of Santa Maria, likely in Uruguaiana, Brazil. This will allow for telemetry coverage throughout the duration of the overnight balloon flight. Figure 7.1 shows the location of Santa Mara and Uruguaiana along with a global map of sprite occurrences estimated from remote ELF magnetic field data from Sato and Fukunishi [2003b] with a peak located to the west of Santa Maria.

The Sprite II Campaign will also include some upgrades to the suite of instruments.

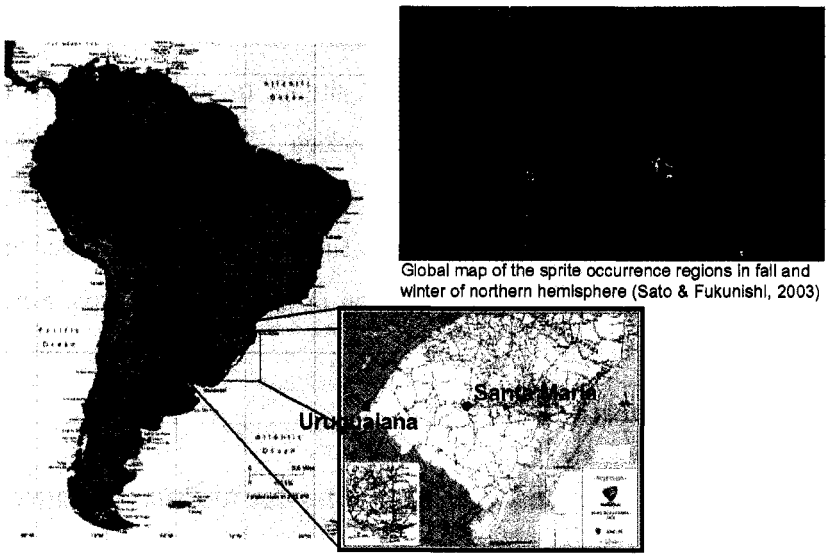

Figure 7.1: Left: Santa Maria and Uruguaiana, Brazil are the launch site and down-range telemetry station (respectively) for the next Sprites Balloon Campaign scheduled for 2005-06. Right: The global map of sprite occurrences estimated from remote ELF magnetic field data from with a peak located to the west of Santa Maria (reproduced from Sato and Fukunishi [2003b]).

A new video camera will be flown on the payload to allow for in situ sprite imaging. The camera to be flown is the WATEC 120 N, which will point upwards with a fish eye lens for 180^0 view. This will allow for sprites to be imaged without having to rely on ground- or aircraft- based imagers that are often blocked by clouds (which happened during both flights of the 2002-03 campaign). An improved electric field sensor, capable of measuring vector fields up to about 500 V/m per axis, will also be flown during the Sprite II Campaign.

In addition to the second Brazil campaign, a balloon campaign to take place over the U. S. High Plains has been proposed for Summer 2006 or 2007. This campaign, named SOCRATES (Stratospheric Overflights of Convective Clouds Responsible for Atmospheric Transient Electric Fields Near Sprites), would use lighter balloon pay-

loads (< 12 lbs) flown on small zero pressure balloons (19000 ft^3). Each payload would include a vector electric field sensor, similar to what is planned for the second Brazil campaign, GPS, and a telemetry package. These balloon payloads would be launched by two mobile teams to optimize the probability of having the balloon float above the most active lightning regions of the storm. Ground-based imaging would be done from the Yucca Ridge Field Station in Colorado and from South Dakota.

7.2 Future Theoretical Research

7.2.1 Mesospheric Preconditioning for Sprites due to Prior Lightning EMPs

Sprites have been observed to occur predominantly during the later stages of thunderstorm activity [Lyons, 1994, 1996], which might suggest that sprites can more easily be generated when the middle atmosphere has been preconditioned due to prior lightning activity. Rodger et al. [2001] has shown that electromagnetic pulses (EMPs) from lightning return strokes cause significant modifications to the electron density (increases of up to 830% and decreases up to 100% from ambient conditions) in the middle atmosphere that can last for hours during times of intense lightning activity. Previous sprite models (such as Pasko et al. [1997a] and the model formulated in Chpt. 5) only include the effects of the quasi-electrostatic field driven by the parent lightning stroke on the electron density and conductivity. To test this preconditioning hypothesis, the effects of the EMPs driven by prior lightning strokes on the electron density and conductivity should be included in sprite models. This could be accomplished by using the model of Rodger et al. [2001], with lightning network location and peak current data for previous strokes, to initialize the electron density of the QSF model presented in Chpt. 5 for confirmed sprite events. This combined EMP/QSF model might also help to explain why sprites often occur horizontally displaced by more than 50 km, and sometimes delayed by up hundreds of ms, from their parent strokes [Wescott et al., 2001a; São Sabbas et al., 2003]. However, the modeling re-

sults of Rodger et al. [2001] have only presented a plausible mechanism to change the electron density, experimental verification of these results also needs to be achieved.

7.2.2 Modeling of Daytime Sprites

Since it is extremely difficult to image sprites during the day, the existence of daytime sprites has only be observed indirectly through ELF radiation [Stanley et al., 2000] and infrasound measurements [Farges et al., 2005]. During the day, the D region ionosphere drops down to altitude of about 60 km due to EUV photo-ionization. Thus, the electron density and conductivity in the middle atmosphere is much larger during the day compared to the night. Hence, it takes a very large charge moment lightning stroke to drive a quasi-electrostatic field large enough to surpass conventional breakdown E_k at altitudes where the relaxation time is long enough for sprite development. Since sprites need at least 1 ms to form, this altitude for daytime sprite initiation must be below about 60-65 km. To initiate runaway with relativistic cosmic ray electrons accelerated by the quasi-electrostatic field (see Chpt. 1.2.1), the relativistic threshold E_t must be surpassed below about 30-35 km in altitude [Roussel-Dupre and Gurevich, 1996; Lehtinen et al., 1997]. Since E_k is about 15 times larger than E_t, the quasi-electrostatic field driven by lightning may more readily surpass the relativistic threshold E_t below 30-35 km compared to surpassing the conventional threshold E_k below 60-65 km, during daytime ionospheric conditions. Hence, these indirect observations of possible daytime sprites might be evidence of a different mechanism for sprite production beyond the QSF model. To test this speculation, a QSF model using realistic daytime ionospheric conditions must be developed.

BIBLIOGRAPHY

N. L. Allen and A. Ghaffar. The conditions required for the propagation of a cathode-directed positive streamer in air. *J. Phys. D Appl. Phys*, 28:331–337, 1995.

N. Y. Babaeva and G. V. Naidis. Dynamics of positive and negative streamers in air in weak uniform electric fields. *IEEE Trans. Plasma Sci.*, 25:375–379, 1997.

B. H. Barnum. *Electromagnetic and Optical Characteristics of Lightning Measured in the Earth's Ionosphere.* PhD thesis, Univ. of Washington, Seattle, Washington, 1999.

C. P. Barrington-Leigh and U. S. Inan. Elves triggered by positive and negative lightning discharges. *Geophys. Res. Lett.*, 26:683–686, 1999.

C. P. Barrington-Leigh, U. S. Inan, and M. Stanley. Identification of sprites and elves with intensified video and broadband array photometry. *J. Geophys. Res.*, 106: 1741–1750, 2001.

C. P. Barrington-Leigh, U. S. Inan, M. Stanley, and S. A. Cummer. Sprites triggered by negative lightning discharges. *Geophys. Res. Lett.*, 26(24):3605–3608, 1999.

E. A. Benbrook, J. W. Kern, and W. R. Sheldon. Measured electric field in the vicinity of a thunderstorm at an altitude of 37 km. *J. Geophys. Res.*, 79:5289–5294, 1974.

E. A. Bering, J. R. Benbrook, L. Bhusal, J. A. Garret, A. M. Paredes, and E. M. Wescott. Observations of transient luminous events (TLEs) associated with negative cloud to ground (-CG) strokes. *Geophys. Res. Lett.*, 31:L05104, doi:10.1029/2003GL018659, 2004a.

E. A. Bering, J. R. Benbrook, J. A. Garret, A. M. Paredes, E. M. Wescott, D. R. Moudry, D. D. Sentman, H. C. Stenbaek-Nielsen, and W. A. Lyons. The electrodynamics of sprites. *Geophys. Res. Lett.*, 29(5):1064, doi:10.1029/2001GL013267, 2002.

E. A. Bering, L. Bhusal, J. R. Benbrook, J. A. Garret, A. P. Jackson, E. M. Wescott, D. R. Moudry, D. D. Sentman, H. C. Stenbaek-Nielsen, and W. A. Lyons. The results from the 1999 sprite balloon campaign. *Adv. Space Res.*, 34:1782–1791, 2004b.

E. A. Bering, T. J. Rosenberg, J. R. Benbrook, D. Detrick, D. L. Matthews, M. J. Rycroft, M. A. Saunders, and W. R. Sheldon. Electric fields, electron precipitation, and VLF radiation during a simultanoeous magnetospheric substorm and atmospheric thunderstorm. *J. Geophys. Res.*, 85:55–72, 1980.

L. Bhusal, E. A. Bering, J. R. Benbrook, J. A. Garret, A. M. Paredes, E. M. Wescott, D. R. Moudry, D. D. Sentman, H. C. Stenbaek-Nielsen, and W. A. Lyons. Statistics and properties of transient luminous event found in the 1999 sprites balloon campaign. *Adv. Space Res.*, 34:1811–1814, 2004.

R. J. Blakeslee, H. J. Christian, and B. Vonnegut. Electrical measurements over thunderstorms. *J. Geophys. Res.*, 94:13135–13140, 1989.

D. Boccippio, E. Williams, S. Heckman, W. Lyons, I. Baker, and R. Boldi. Sprites, ELF transients, and positive ground strokes. *Science*, 269:1088, 1995.

W. L. Boeck, O. H. Vaughan, and R. J. Blakeslee. Low light level TV images of terrestrial lightning as viewed from space. *Trans. Am. Geophys. U. (EOS abstract)*, 72:171, 1991.

H. J. Christian, R. J. Blakeslee, D. J. Boccippio, W. L. Boeck, D. E. Buechler, K. T. Driscoll, S. J. Goodman, J. M. Hall, W. J. Koshak, D. M. Mach, and M. F. Stewart.

Global frequency and distribution of lightning as observed from space by the Optical Transient Detector. *J. Geophys. Res.*, 108(D1):doi:10.1029/2002JD002347, 2003.

M. A. Clilverd, C. J. Rodger, and D. Nunn. Radiation belt electron precipitation fluxes associated with lightning. *J. Geophys. Res.*, 109(A12208): doi:10.1029/2004JA010644, 2004.

S. A. Cummer and M. Füllekrug. Unusually intense continuing current in lightning produces delayed mesospheric breakdown. *Geophys. Res. Lett.*, 28(3):495–498, 2001.

S. A. Cummer, U. S. Inan, T. F. Bell, and C. P. Barrington-Leigh. ELF radiation produced by the electrical currents in sprites. *Geophys. Res. Lett.*, 25(8):1281–1284, 1998.

S. A. Cummer and W. A. Lyons. Lightning charge moment changes in U.S. High Plains thunderstorms. *Geophys. Res. Lett.*, 31(L05114):doi:10.1029/2003GL019043, 2004.

S. A. Cummer and W. A. Lyons. Implications of lightning charge moment changes for sprite initiation. *J. Geophys. Res.*, 110:doi:10.1029/2004JA010812, 2005.

D. K. Davies. Measurements of swarm particles in dry air, Note 346, Westinghouse R&D center. Pittsburg, PA, 1983.

O. de La Beaujardiere and the C/NOFS Science Definition Team. C/NOFS: a mission to forecast scintillations. *J. Atmos. Sol Terr.*, 66:1573–1591, 2004.

T. Farges, E. Blanc, A. Le Pichon, T. Neubert, and T. H. Allin. Identification of infrasound produced by sprites during the Sprite2003 campaign. *Geophys. Res. Lett.*, 32(L01813):doi:10.1029/2004GL021212, 2005.

R. F. Fernsler and H. L. Rowland. Models of lightning-produced sprites and elves. *J. Geophys. Res.*, 101:29653–29662, 1996.

R. C. Franz, R. J. Nemzek, and J. R. Winckler. Television image of a large electrical discharge above a thunderstorm system. *Science*, 249:48–51, 1990.

H. Fuknunishi, Y. Takahashi, M. Kubota, K. Sakanoi, U. S. Inan, and W. A. Lyons. Elves: Lightning-induced transient luminous events in the lower ionosphere. *Geophys. Res. Lett.*, 23:2157–2160, 1996.

O. H. Gish and G. R. Wait. Thunderstorms and the earth's general electrification. *J. Geophys. Res.*, 55:473–484, 1950.

L. C. Hale, C. L. Croskey, and J. D. Mitchell. Measurements of middle atmospheric electric fields and associated electrical conductivities. *Geophys. Res. Lett.*, 8(8): 927–930, 1981.

R. Hegerberg and I. D. Reid. Electron drift velocities in air. *Aust. J. Physics*, 33:227, 1980.

Y. Hiraki, T. Lizhu, H. Fukunishi, K. Nanbu, and H. Fujiwara. Development of a new numerical model for investigating the energetics of sprites. *Eos Trans. AGU*, 83(47):Fall Meet. Suppl., Abstract A11C–0105, 2002.

R. H. Holzworth. *Large scale dc electric fields in the Earth's environment.* PhD thesis, Univ. of California, Berkeley, California, 1977.

R. H. Holzworth and E.A. Bering. Ionospheric electric fields from stratospheric balloon-borne probes. In *Measurement Techniques in Space Plasmas: Fields*, volume Geophysical Monograph, 103, pages 79–84. American Geophysical Union, 1998.

R. H. Holzworth, M. C. Kelley, C. L. Siefring, L. C. Hale, and J. D. Mitchell. Electrical measurements in the atmosphere and the ionosphere over an active thunderstorm. 2. Direct current electric fields and conductivity. *J. Geophys. Res.*, 90(A10):9824–9830, 1985.

R. H. Holzworth, M. P. McCarthy, J. N. Thomas, J. Chin, T. M. Chinowsky, M. J. Taylor, and O. Pinto Jr. Strong electric fields from positive lightning strokes in the stratosphere. *Geophys. Res. Lett.*, 32(L04809):doi:10.1029/2004GL021554, 2005.

R. H. Holzworth and F. S. Mozer. Direct evidence of solar flare modification of stratospheric electric fields. *J. Geophys. Res.*, 84:363–367, 1979.

R. H. Holzworth, K. W. Norville, P. M. Kinter, and S. P. Powell. Stratospheric conductivity variations over thunderstorms. *J. Geophys. Res.*, 91:13257–13263, 1986.

H. Hu. *Global and local electrical phenomena in the stratopshere.* PhD thesis, Univ. of Washington, Geophysics Program, Seattle, Washington, 1994.

H. Hu, R. H. Holzworth, and Y. Q. Li. Thunderstorm related variations in stratospheric conductivity measurements. *J. Geophys. Res.*, 94:16429–16435, 1989.

U. S. Inan, C. P. Barrington-Leigh, S. Hansen, V. S. Glukhov, T. F. Bell, and R. Rairden. Rapid lateral expansion of optical luminosity in lightning-induced ionospheric flashes referred to as 'elves'. *Geophys. Res. Lett.*, 24:583–586, 1997.

E. R. Jayaratne, C. P. R. Saunders, and J. Hallett. Laboratory studies of the charging of soft-hail during ice crystal interactions. *Q. J. R. Meteorol. Soc.*, 109, 1983.

M. C. Kelley, C. L. Siefring, R. F. Pfaff, P. M. Kinter, M. Larsen, R. Green, R. H. Holzworth, L. C. Hale, J. D. Mitchell, and D. Le Vine. Electrical measurements in the atmosphere and the ionosphere over an active thunderstorm. 2. Campaign overview and initial ionospheric results. *J. Geophys. Res.*, 90(A10):9815–9823, 1985.

P. J. Kellogg and M. Weed. Balloon measurements of ionospheric electric fields. In *Proceedings of the Fourth International Conference on the Universal Aspects of Atmospheric Electricity*, Tokyo, 1968.

E. H. Lay, R. H. Holzworth, C. J. Rodger, J. N. Thomas, O. Pinto Jr., and R. L. Dowden. WWLL global lightning detection system: Regional validation study in Brazil. *Geophys. Res. Lett.*, 31:L03102, doi:10.1029/2003GL018882, 2004.

N. G. Lehtinen, T. F. Bell, V. P. Pasko, and U. S. Inan. A two-dimensional model of runaway electron beams driven by quasi-electrostatic thundercloud fields. *Geophys. Res. Lett.*, 24(21):2639–2642, 1997.

Y. Q. Li, R. H. Holzworth, H. Hua, M. P. McCarthy, R. D. Massey, P. M. Kinter, J. V. Rodriguez, U. S. Inan, and W. C. Armstrong. Anomalous optical events detected by rocket-borne sensor in the WIPP campaign. *J. Geophys. Res.*, 96(A2): 1315–1326, 1991.

W. A. Lyons. Characteristics of luminous structures in the stratosphere above thunderstorms as imaged by low-light video. *Geophys. Res. Lett.*, 21:875–888, 1994.

W. A. Lyons. Sprite observations above the U.S. High Plains in relation to their parent thunderstorm systems. *J. Geophys. Res.*, 101:29641–29652, 1996.

W. A. Lyons, T. E. Nelson, R. A. Armstrong, V. P. Pasko, and Stanley. M. A. Upward electrical discharges from thunderstorm tops. *Bull. Am. Meteorol. Soc.*, 84(4):445–454, 2003.

D. R. MacGorman and W. D. Rust. *The Electrical Nature of Storms.* Oxford University Press, New York, 1998.

T. C. Marshall, M. P. McCarthy, and W. D. Rust. Electric-field magnitudes and lightning initiation in thunderstorms. *J. Geophys. Res.*, 100:7097–7103, 1995.

T. C. Marshall, M. Stolzenburg, and W. D. Rust. Electric field measurements above mesoscale convective systems. *J. Geophys. Res.*, 101:6979–6996, 1996.

N. C. Maynard, C. L. Croskey, J. D. Mitchell, and L. C. Hale. Measurement of volt/meter vertical electric fields in the middle atmosphere. *Geophys. Res. Lett.*, 8 (8):923–926, 1981.

F. S. Mozer and R. Serlin. Magnetospheric electric field meaurements with balloons. *J. Geophys. Res.*, 74:4739–4754, 1969.

C. G. Park and M. Dejnakarintra. Penetration of thundercloud electric-fields into ionosphere and magnetosphere. 1. Middle and subauroral latitudes. *J. Geophys. Res.*, 78(28):6623–6633, 1973.

V. P. Pasko. Atmospheric physics: Electric jets. *Nature*, 423(6943):927–929, 2003.

V. P. Pasko. Theoretical modeling of sprites and jets. In *NATO ASI on Intense Lightning Discharges and Sprites*, Corte, Corsica, France, 2004.

V. P. Pasko and U. S. Inan. Recovery signatures of lightning-associated VLF perturbations as a measure of the lower ionosphere. *J. Geophys. Res.*, 99(A9):17523–17538, 1994.

V. P. Pasko, U. S. Inan, and T. F. Bell. Sprites as evidence of vertical gravity wave structures above mesoscale thunderstorms. *Geophys. Res. Lett.*, 24(14):1735–1738, 1997b.

V. P. Pasko, U. S. Inan, and T. F. Bell. Spatial structure of sprites. *Geophys. Res. Lett.*, 25(12):2123–2126, 1998a.

V. P. Pasko, U. S. Inan, T. F. Bell, and S. C. Reising. Mechanism of ELF radiation from sprites. *Geophys. Res. Lett.*, 25(18):3493–3496, 1998b.

V. P. Pasko, U. S. Inan, T. F. Bell, and Y. N. Taranenko. Sprites produced by quasi-electrostratic heating and ionization in the lower ionosphere. *J. Geophys. Res.*, 102: 4529–4562, 1997a.

V. P. Pasko, M. A. Stanley, J. D. Mathews, U. S. Inan, and T. G. Woods. Electrical discharge from a thunderstorm top to the lower ionosphere. *Nature*, 416:152–154, 2002.

I. R. C. A Pinto, O. Pinto Jr., W. D. Gonzalez, S. L. Dutra, J. Wygant, and F. S. Mozer. Stratospheric electric field and conductivity measurements over electrified convective clouds in the South American region. *J. Geophys. Res.*, 93:709–715, 1988.

O. Pinto, Jr., I. R. C. A. Pinto, R. B. B. Gin, and Jr. O. Mendes. Positive thunderstorms in Brazil. *Annales Geophysicae*, 16:353–355, 1998.

O. Pinto, Jr., M. M. F. Saba, I. R. C. A. Pinto, F. S. S. Tavares, K. P. Naccarato, N. N. Solorzano, M. J. Taylor, P. D. Pautet, and R. H. Holzworth. Thunderstorm and lightning characteristics associated with sprites in Brazil. *Geophys. Res. Lett.*, 31(L13103):doi:10.1029/2004GL020264, 2004.

Y. P. Raiser. *Gas Discharge Physics.* Springer-Verlag, New York, 1991.

V. A. Rakov and M. A. Uman. *Lightning: Physics and Affects.* Cambridge University Press, Cambridge, UK, 2003.

R. G. Roble and I. Tzur. The global atmospheric-electrical circuit. In *The Earth's Electrical Environment, Studies in Geophysics*, pages 206–231. National Academy Press, Washington, DC, 1986.

C. J. Rodger, M. Cho, M. A. Clilverd, and M. J. Rycroft. Lower ionospheric modification by lightning-EMP: Simulation of the night ionosphere over the United States. *Geophys. Res. Lett.*, 28(2):199–202, 2001.

R. Roussel-Dupre and A. V. Gurevich. On runaway breakdown and upward propagating discharges. *J. Geophys. Res.*, 101:2297–2311, 1996.

H. L. Rowland. Theories and simulations of elves, sprites and blue jets. *J. Atmos. Sol Terr.*, 60:831–844, 1998.

M. M. F. Saba, O. Pinto Jr., and I. R. C. A. Pinto. Stratospheric conductivity measurements in Brazil. *J. Geophys. Res.*, 104:27203–27208, 1999.

M. M. F. Saba, O. Pinto Jr., I. R. C. A. Pinto, and O. Mendes Jr. Stratospheric balloon measurements of electric fields associated with thunderstorms and lightning in Brazil. *J. Geophys. Res.*, 105:18091–18097, 2000.

F. T. São Sabbas, D. D. Sentman, E. M. Wescott, O. Pinto Jr., O. Mendes Jr., and M. J. Taylor. Statistical analysis of spacetime relationships between sprites and lightning. *J. Atmos. Sol Terr.*, 65:525–535, 2003.

M. Sato and H. Fukunishi. Global sprite occurrence locations and rates derived from triangulation of transient schumann resonance events. *Geophys. Res. Lett.*, 30(16): doi:10.1029/2003GL017291, 2003b.

M. Sato, H. Fukunishi, M. Kikuchi, H. Yamagishi, and W. A. Lyons. Validation of sprite-inducing cloud-to-ground lightning based on ELF observations at Syowa station in Antarctica. *J. Atmos. Sol Terr.*, 65:607–614, 2003a.

C. P. R. Saunders. Thunderstorm electrification. In H. Volland, editor, *Atmospheric Electrodynamics*, volume 1, pages 61–92. CRC Press, 1995.

D. D. Sentman, E. M. Wescott, D. L. Osborne, D. L. Hampton, and M. J. Heavner. Preliminary results from the Sprites94 aircraft campaign, 1. Red sprites. *Geophys. Res. Lett.*, 22:1205–1208, 1995.

R. M. Skoug. *The Origin of Narrow Band Cyclotron Wave Emissions Called Chorus.* PhD thesis, Univ. of Washington, Seattle, Washington, 1995.

M. Stanley, M. Brook, P. Krehbiel, and S. A. Cummer. Detection of daytime sprites via a unique sprite ELF signature. *Geophys. Res. Lett.*, 27(6):871–874, 2000.

M. Stanley, P. Krehbiel, M. Brook, C. B. Moore, W. Rison, and B. Abrahams. High speed video of initial sprite development. *Geophys. Res. Lett.*, 26(20):3201–3204, 1999.

C. G. Stergis, G. C. Rein, and T. Kangas. Electric field measurements above thunderstorms. *J. Atmos. Terr. Phys.*, 11:83–90, 1957.

M. Stolzenburg, W. D. Rust, and T. C. Marshall. Electrical structure in thunderstorm convective regions 3. Synthesis. *J. Geophys. Res.*, 103(D12):14097–14108, 10.1029/97JD03545, 1998.

H. T. Su, R. R. Hsu, A. B. Chen, Y. C. Wang, W. S. Hsiao, W. C. Lai, L. C. Lee, M. Sato, and H. Fukunishi. Gigantic jets between a thundercloud and the ionosphere. *Nature*, 423:974–976, 2003.

P. Swarztrauber and R. Sweet. Efficient Fortran subprograms for the solution of separable elliptic partial differential equations. *ACM Transactions on Mathematical Software*, 5:352–364, 1979.

Y. Takahashi, R. Miyasato, T. Adachi, K. Adachi, M. Sera, A. Uchida, and H. Fukunishi. Activities of sprites and elves in the winter season, Japan. *J. Atmos. Sol Terr.*, 65:551–560, 2003.

J. N. Thomas, R. H. Holzworth, and J. Chin. A new high-voltage electric field instrument for studying sprites. *IEEE Trans. Geo. Remote Sensing*, 42(7):1399–1404, 2004.

J. N. Thomas, R. H. Holzworth, M. P. McCarthy, and O. Pinto Jr. Predicting lightning-driven quasi-electrostatic fields at sprite altitudes using in

situ measurements and a numerical model. *Geophys. Res. Lett.*, 32(L10809): doi:10.1029/2005GL022693, 2005.

M. A. Uman. *Lightning.* Dover, New York, 1984.

H. Volland. *Atmospheric Electrodynamics.* Springer-Verlag, Berlin, Germany, 1984.

H. D. Voss, M. Walt, W. L. Imhof, J. Mobilia, and U. S. Inan. Satellite observations of lightning-induced electron precipitation. *J. Geophys. Res.*, 103:11,725–11,744, 1998.

E. M. Wescott, D. Sentman, D. Osborne, D. Hampton, and M. Heavner. Preliminary results from the Sprites94 aircraft campaign, 2, Blue jets. *Geophys. Res. Lett.*, 22: 1209–1212, 1995.

E. M. Wescott, D. Sentman, H. C. Stenbaek-Nielsen, P. Huet, M. J. Heavner, and D. R. Moudry. New evidence for the brightness and ionization of blue starters and blue jets. *J. Geophys. Res.*, 106:21549–21554, 2001b.

E. M. Wescott, H. C. Stenbaek-Nielsen, D. D. Sentman, M. J. Heavner, D. R. Moudry, and F. T. São Sabbas. Triangulation of sprites, associated halos and their possible relation to causative lightning and micrometeors. *J. Geophys. Res.*, 106(A6):10467–10477, 2001a.

E. R. Williams. Meteorological aspects of thunderstorms. In H. Volland, editor, *Atmospheric Electrodynamics*, volume 1, pages 27–60. CRC Press, 1995.

E. R. Williams. The positive charge reservoir for sprite-producing lightning. *J. Atmos. Sol Terr.*, 60:689–692, 1998.

H. Williams. Rider on the storm. *New Scientist*, page 3636, Dec. 15, 2001.

C. T. R. Wilson. Investigations on lightning discharges and on the electric field of the earth. *Philos. Trans. R. Soc. London, Ser. A.*, A221:73–115, 1920.

C. T. R. Wilson. The electric field of a thundercloud and some if its effects. *Proc. Phys. Soc. London*, 37:32D–37D, 1925.

Appendix A

CIRCUIT DIAGRAM FOR THE HIGH VOLTAGE ELECTRIC FIELD SENSOR

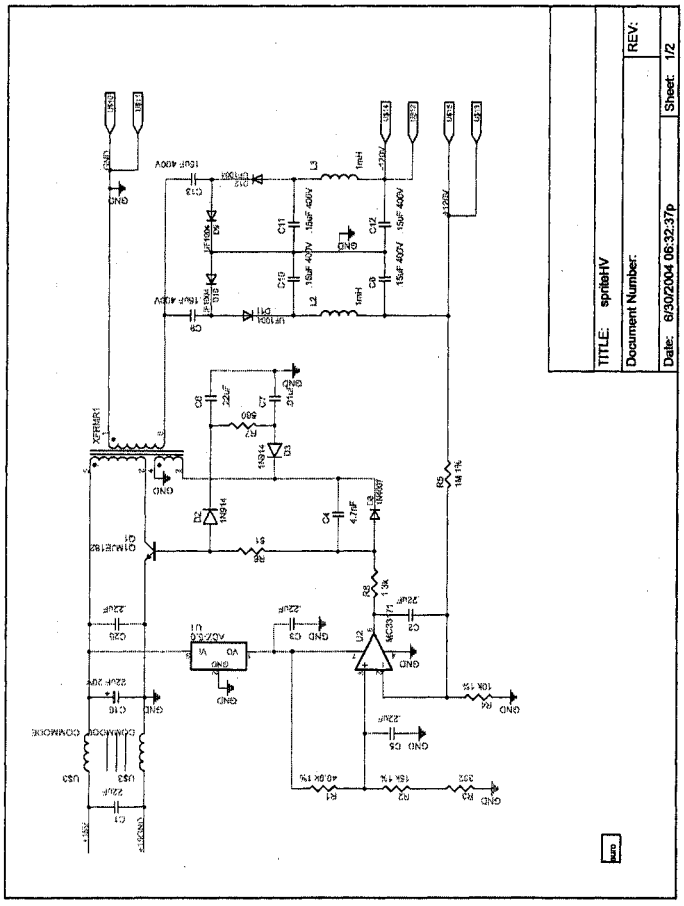

Figure A.1: Schematic for the High Voltage Electric Field Sensor power supply.

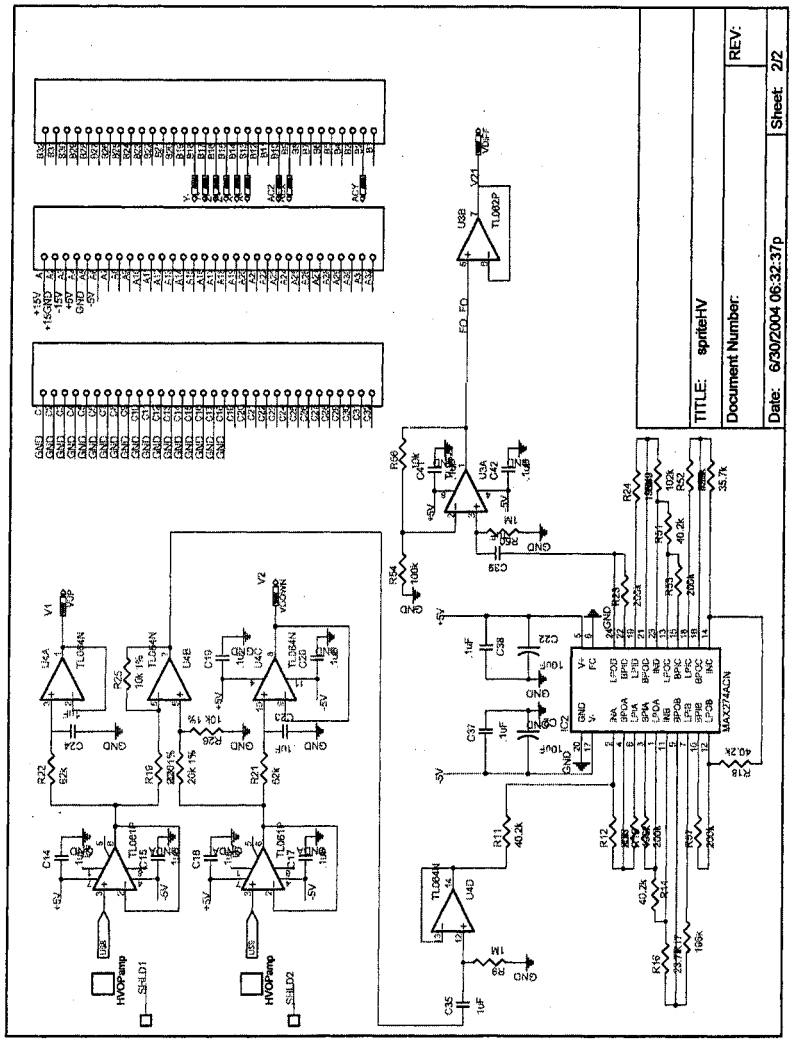

Figure A.2: Schematic for the High Voltage Electric Field Sensor dc and ac voltage measurement circuit.

Appendix B

DATA EXTRACTION AND INSTRUMENT CALIBRATION FOR THE BRAZIL SPRITE BALLOON CAMPAIGN

B.1 Data Extraction

Data for both Flights 1 and 2 of the Brazil Sprite Balloon Campaign can be extracted using the `sp4.exe` program developed by Michael McCarthy. Below is the `README.txt` file for `sp4.exe`.

```
Sprite data extraction software

1. This code is now pretty solid. One known bug is that it will
   trip up over a consecutive sequence of bit-error infected
   frame counters. It does not extract raw x-ray data.

2. The solution to recovering the poor quality data in the
   6/7Mar03 campaign is to run through the all the data and
   build an index file containing sorted pairs of frame number
   and offset into file of that frame's data. The index file
   is a large file that is built once for each flight.

3. The data extract code will fetch up to 10 streams of adc
   data between 2 specified times.
```

4. Installation

unzip sp4.zip on the desktop---into a new folder, SP4, on desktop

enter SP4 directory and execute install program

install to directory SP4, not the default install directory these 4 auxiliary files must be in the directory where the software runs

parms.dat	sets run time parameters
adc_vals.txt	table of adc sampling schedule
FLT_files.dat	list of data filenames and first frame counters
FLT_index.dat	binary list of frame counter, file id's, and file offsets

5. Un-installation

Do this from System Panel, Add/Remove Software.

Remove sprite_extract; then remove install directory SP4

6. Build the index file (run once per flight)

First copy one of the FLT?_files.dat files to file FLT_files.dat

Prepare the parms.dat file to point to the directory containing the data files and set the flight id number; other fields in parms.dat must be present, but the values are ignored.

Run build_index in directory SP4---this builds a large index file by reading through all the data

Rename index.dat (the output file) to FLT?_index.dat

7. Extracting data

Prepare the parms.dat file to describe the desired data

Go to the directory SP4 and start sprite_extract.exe

This can be done through a console window or by mouse-clicking. A console window has the advantage of leaving up error messages.

8. format of parms.dat file

This file has N+5 entries in the following order

A. a flight ID code (1 for 6/7Dec02; 2 for 6/7Mar03; etc)

B. start time: A UTC time in the format 2002-12-06/22:03:00 or 2002-12-06/22:03:00.000000 where the precision of fractional seconds is arbitrary.

C. stop time: same format as start time

D. data path: path to the location of the tm data files, e.g., D:/TM/

E. N: integer indicating the number of data types to process

F. N data codes: integer adc codes specifying data types. For instance, 0 is VLF Bx, 30 is the low voltage y-component DC electric field.

The entries must be space separated and no entry should span lines in parms.dat

9. Input

No input is requested during runtime. parms.dat is the default source of input to the code, but an alternate file of input data can be specified on the command line from a console window.

10. Output

Primary output is a set of binary files consisting of (time, data) pairs. The time is 3 16 bit words which taken together represent the number of 10ns ticks since the start of the week. To convert these into a double precision seconds of week variable, use: secs_of_week = (val3 + 65536D0 * (val2 + 65536D0 * val1))*1.0D-8, where 65536D0 and 1.0D-8 are assumed to be double precision floating point numbers. The data field is a 16bit word value extracted from the adc part of the telemetry frame.Data has not been error-corrected. The filenames are of the form descriptor.dat, where descriptor is a name indicating type of data. Examples: bx.dat, ld_up.dat,e_lv_ac_x.dat.If a same-name file already exists in the current directory, it will be over-written. Binary data byte ordering is little-endian (PC compatible).

A secondary output consists of progress lines every 500000 records written, indications when a new file begins to be processed, and a total for the number of samples for which there was a confusion in timing an adc sample.

B.2 Instrument Calibration

The following MATLAB .m routines convert output of sp4.exe for a given channel (such as e_lv_ac_x.dat) into physical units (such as seconds and V/m):

```
% LV-AC-Z
% open data file
fnlp=fopen('e_lv_ac_z.dat','r');
% read data file
lvzp=fread(fnlp,[4,10e6],'uint16');
% time in seconds of the week
secsz=([lvzp(3,:)]'+65536*([lvzp(2,:)]'+65536*[lvzp(1,:)]'))*1e-8;
% LV-AC-Z in V/m
lvez=(-1/5.988)*.0073*([lvzp(4,:)]'-2047)/3.08;

% LV-AC-X
% open data file
fnlp=fopen('e_lv_ac_x.dat','r');
% read data file
lvzp=fread(fnlp,[4,10e6],'uint16');
% time in seconds of the week
secsx=([lvzp(3,:)]'+65536*([lvzp(2,:)]'+65536*[lvzp(1,:)]'))*1e-8;
% LV-AC-X in V/m
lvex=(-1/5.988)*.0073*([lvzp(4,:)]'-2051)/3.60;

% LV-AC-Y
% open data file
fnlp=fopen('e_lv_ac_y.dat','r');
% read data file
```

```
lvzp=fread(fnlp,[4,10e6],'uint16');
% time in seconds of the week
secsy=([lvzp(3,:)]'+65536*([lvzp(2,:)]'+65536*[lvzp(1,:)]'))*1e-8;
% LV-AC-Y in V/m
lvey=(-1/5.988)*.0073*([lvzp(4,:)]'-2051)/3.60;

%LV-DC-Z
% open data file
fn1=fopen('e_lv_dc_z.dat','r');
% read data file
hvzn=fread(fn1,[4,10e6],'uint16');
% time in seconds of the week
secsz=([hvzn(3,:)]'+65536*([hvzn(2,:)]'+65536*[hvzn(1,:)]'))*1e-8;
% LV-DC-Z in V/m
lvez=(-1)*.0073*([hvzn(4,:)]'-2063)/3.08;

%LV-DC-X
% open data file
fn1=fopen('e_lv_dc_x.dat','r');
% read data file
hvzn=fread(fn1,[4,10e6],'uint16');
% time in seconds of the week
secsx=([hvzn(3,:)]'+65536*([hvzn(2,:)]'+65536*[hvzn(1,:)]'))*1e-8;
% LV-DC-X in V/m
lvex=(-1/5.988)*.0073*([hvzn(4,:)]'-2047)/3.60;

%LV-DC-Y
% open data file
```

```
fn1=fopen('e_lv_dc_y.dat','r');
% read data file
hvzn=fread(fn1,[4,10e6],'uint16');
% time in seconds of the week
secsy=([hvzn(3,:)]'+65536*([hvzn(2,:)]'+65536*[hvzn(1,:)]'))*1e-8;
% LV-DC-Y in V/m
lvey=(-1/5.988)*.0073*([hvzn(4,:)]'-2047)/3.60;

%LV-DC-Z+/-
% open data files
fnlp=fopen('e_lv_dc_zp.dat','r');
fnln=fopen('e_lv_dc_zn.dat','r');
% read data files
lvzp=fread(fnlp,[4,10e6],'uint16');
lvzn=fread(fnln,[4,10e6],'uint16');
% time in seconds of the week
secsp=([lvzp(3,:)]'+65536*([lvzp(2,:)]'+65536*[lvzp(1,:)]'))*1e-8;
secsn=([lvzn(3,:)]'+65536*([lvzn(2,:)]'+65536*[lvzn(1,:)]'))*1e-8;
%LV-DC-Z+/- in V/m
lvezp=.0066*([lvzp(4,:)]'-2063)/1.54;
lvezn=.0066*([lvzn(4,:)]'-2063)/1.54;

%LV-DC-X+/-
% open data files
fn1=fopen('e_lv_dc_xp.dat','r');
fn2=fopen('e_lv_dc_xn.dat','r');
% read data files
lvxp=fread(fn1,[4,10e6],'uint16');
```

```
lvxn=fread(fn2,[4,10e6],'uint16');
% time in seconds of the week
secsp=([lvxp(3,:)]'+65536*([lvxp(2,:)]'+65536*[lvxp(1,:)]'))*1e-8;
secsn=([lvxn(3,:)]'+65536*([lvxn(2,:)]'+65536*[lvxn(1,:)]'))*1e-8;
%LV-DC-X+/- in V/m
lvexp=.0064*([lvxp(4,:)]'-2051)/1.8;
lvexn=.0065*([lvxn(4,:)]'-2051)/1.8;

%LV-DC-Y+/-
% open data files
fn1=fopen('e_lv_dc_yp.dat','r');
fn2=fopen('e_lv_dc_yn.dat','r');
% read data files
lvyp=fread(fn1,[4,10e6],'uint16');
lvyn=fread(fn2,[4,10e6],'uint16');
% time in seconds of the week
secsp=([lvxp(3,:)]'+65536*([lvxp(2,:)]'+65536*[lvxp(1,:)]'))*1e-8;
secsn=([lvxn(3,:)]'+65536*([lvxn(2,:)]'+65536*[lvxn(1,:)]'))*1e-8;
%LV-DC-Y+/- in V/m
lveyp=.0064*([lvxp(4,:)]'-2051)/1.8;
lveyn=.0065*([lvxn(4,:)]'-2051)/1.8;

%HV-AC-Z
% open data file
fnlp=fopen('e_hv_ac_z.dat','r');
% read data file
lvzp=fread(fnlp,[4,10e6],'uint16');
% time in seconds of the week
```

```
secsz=([lvzp(3,:)]'+65536*([lvzp(2,:)]'+65536*[lvzp(1,:)]'))*1e-8;
%HV-AC-Z in V/m
hvez=.0607*([lvzp(4,:)]'-2048)*(2/1.56);

%HV-AC-X
% open data file
fnx=fopen('e_hv_ac_x.dat','r');
% read data file
hvx=fread(fnx,[4,10e6],'uint16');
% time in seconds of the week
secsxac=([hvx(3,:)]'+65536*([hvx(2,:)]'+65536*[hvx(1,:)]'))*1e-8;
%HV-AC-X in V/m
hvex_ac=.0607*([hvx(4,:)]'-2048)*(2/2)*.70;

%HV-DC-Z+/-
% open data files
fn1=fopen('e_hv_dc_zp.dat','r');
fn2=fopen('e_hv_dc_zn.dat','r');
% read data files
hvzp=fread(fn1,[4,10e6],'uint16');
hvzn=fread(fn2,[4,10e6],'uint16');
% time in seconds of the week
secsp=([hvzp(3,:)]'+65536*([hvzp(2,:)]'+65536*[hvzp(1,:)]'))*1e-8;
secsn=([hvzn(3,:)]'+65536*([hvzn(2,:)]'+65536*[hvzn(1,:)]'))*1e-8;
%HV-DC-Z+/- in V/m
hvezp=.0607*([hvzp(4,:)]'-2048)/0.78;
hvezn=.0607*([hvzn(4,:)]'-2048)/0.78;
```

```
%HV-DC-X+/-
% open data files
fnp=fopen('e_hv_dc_xp.dat','r');
fnn=fopen('e_hv_dc_xn.dat','r');
% read data files
hvxp=fread(fnp,[4,10e6],'uint16');
hvxn=fread(fnn,[4,10e6],'uint16');
% time in seconds of the week
secsp=([hvxp(3,:)]'+65536*([hvxp(2,:)]'+65536*[hvxp(1,:)]'))*1e-8;
secsn=([hvxn(3,:)]'+65536*([hvxn(2,:)]'+65536*[hvxn(1,:)]'))*1e-8;
%HV-DC-X+/- in V/m
hvexp=(0.7)*.0607*([hvxp(4,:)]'-2048);
hvexn=(0.7)*.0607*([hvxn(4,:)]'-2048);

%VLF-BZ
% open data file
fnbz=fopen('bz.dat','r');
% read data file
bz=fread(fnbz,[4,10e6],'uint16');
% time in seconds of the week
secsbz=([bz(3,:)]'+65536*([bz(2,:)]'+65536*[bz(1,:)]'))*1e-8;
% VLF-BZ in nT
bzac=([bz(4,:)]'*7.08e-3-14.5)*34/43;

%VLF-BX
% open data file
fnbx=fopen('bx.dat','r');
% read data file
```

```
bx=fread(fnbx,[4,10e6],'uint16');
% time in seconds of the week
secsbx=([bx(3,:)]'+65536*([bx(2,:)]'+65536*[bx(1,:)]'))*1e-8;
% VLF-BX in nT
bxac=([bx(4,:)]'*7.08e-3-14.5)*34/43;

%VLF-BY
% open data file
fnby=fopen('by.dat','r');
% read data file
by=fread(fnby,[4,10e6],'uint16');
% time in seconds of the week
secsby=([by(3,:)]'+65536*([by(2,:)]'+65536*[by(1,:)]'))*1e-8;
% VLF-BY in nT
byac=([by(4,:)]'*8.79e-3-18)*34/43;

%LD-UP/LD-Down
% open data files
fnlu=fopen('ld_up.dat','r');
fnld=fopen('ld_dn.dat','r');
% read data files
ldu=fread(fnlu,[4,10e6],'uint16');
ldd=fread(fnld,[4,10e6],'uint16');
% time in seconds of the week
secslu=([ldu(3,:)]'+65536*([ldu(2,:)]'+65536*[ldu(1,:)]'))*1e-8;
secsld=([ldd(3,:)]'+65536*([ldd(2,:)]'+65536*[ldd(1,:)]'))*1e-8;
%LD-UP/LD-Down in W/cm^2
ldup=7.5e-13*([ldu(4,:)]').^2;
```

```
lddn=7.5e-13*([ldd(4,:)]').^2;
```

Appendix C

FLIGHT NOTES FOR THE BRAZIL SPRITE BALLOON CAMPAIGN

C.1 Flight 1

Brazil Sprite Flight 1 was launched from Cachoeira Paulista, Brazil ($22^0 44'$ S, $44^0 56'$ W) at approximately 22:00:00 UT (20:00:00 local time) Dec. 6, 2002. The payload reached an altitude of about 30 km at 23:23:00 UT and stayed between 30-35 km for the duration of the flight until telemetry was lost at 10:49:00 UT Dec. 7, when the payload was downrange 426 km from the groundstation. All sensors worked properly except the uplooking optical power sensor that was unable to gather any data. The rotation motor worked properly throughout the flight rotating the payload clockwise when viewed from above. The electric and magnetic field sensors on the payload measured thousands of lightning-driven field changes with the nearby events occurring before 00:47:00 UT. The sprite imaging aircraft was airborne for a few hours during this flight, but could not observe sprites due to significant high altitude cloud coverage.

C.2 Flight 2

Brazil Sprite Flight 2 was launched from Cachoeira Paulista, Brazil ($22^0 44'$ S, $44^0 56'$ W) at approximately 23:40:00 UT (20:40:00 local time) March 6, 2003. The payload reached an altitude of about 30 km at 01:35:00 UT March 7 and stayed between 30-35 km for the duration of the flight until telemetry was lost at 04:00:00 UT March 7, when the payload was downrange 267 km from the groundstation. Due to a groundstation noise problem, the data set from Flight 2 is very limited, although some electric

and magnetic field changes driven by lightning were measured. The sprite imaging aircraft was grounded due to severe local weather for the duration of this flight.

C.3 Published Articles Pertaining to the Brazil Sprite Balloon Campaign

Thomas et al. [2004] includes a detailed description of the HV Electric Field Sensor. Holzworth et al. [2005] is an overview of the electric field and conductivity measurements from the Brazil Balloon Campaign. Thomas et al. [2005] compares in situ electric field data to a QSF model and predicts the electric fields at sprite altitudes.

VITA

Jeremy Norman Thomas was born in Westfield, New York on May 26, 1978 to Carter and Constance Thomas. He graduated from Bishop Verot High School in Fort Myers, Florida in 1996. He received the B.A. degree from Bard College, Annandale-on-Hudson, NY, in 2000, and the M.S. degree from the University of Washington, Seattle, in 2002, both in physics. He was previously involved in neutrino physics research at the University of Oklahoma (1998), Los Alamos National Laboratory (1999), Bard College (1999-2000), and the University of the Witwatersrand, Johannesburg, South Africa (1999). Since 2001, he has been a member of the Space Physics Group, Department of Earth and Space Sciences, University of Washington, where has been involved in atmospheric electrodynamics research. His current interests include the electrodynamics of sprites and intense lightning, the World Wide Lightning Location Network (WWLLN), and x-ray measurements from triggered lightning.